5-12-2023

Eddy current defect response analysis using sum of Gaussian methods

James William Earnest
Mississippi State University, jearnest1@cox.net

Eddy current defect response analysis using sum of Gaussian methods

By

James William Earnest

Approved by:

Robert J. Moorhead (Major Professor)
John E. Ball
Mehmet Kurum
Ali Gurbuz
Qian (Jenny) Du (Graduate Coordinator)
Jason M. Keith (Dean, Bagley College of Engineering)

A Dissertation
Submitted to the Faculty of
Mississippi State University
in Partial Fulfillment of the Requirements
for the Degree of Doctor of Philosophy
in Electrical and Computer Engineering
in the Department of Electrical and Computer Engineering

Mississippi State, Mississippi

May 2023

Name: James William Earnest

Date of Degree: May 12, 2023

Institution: Mississippi State University

Major Field: Electrical and Computer Engineering

Major Professor: Robert J. Moorhead

Title of Study: Eddy current defect response analysis using sum of Gaussian methods

Pages in Study: 148

Candidate for Degree of Doctor of Philosophy

This dissertation is a study of methods to automatedly detect and produce approximations of eddy current differential coil defect signatures in terms of a summed collection of Gaussian functions (SoG). Datasets consisting of varying material, defect size, inspection frequency, and coil diameter were investigated. Dimensionally reduced representations of the defect responses were obtained utilizing common existing reduction methods and novel enhancements to them utilizing SoG Representations. Efficacy of the SoG enhanced representations were studied utilizing common Machine Learning (ML) interpretable classifier designs with the SoG representations indicating significant improvement of common analysis metrics.

DEDICATION

When I started this educational journey many years ago, one very significant aspect of the purpose was to provide a testament through my efforts of the hard work of my parents who unfortunately are no longer with me. Through God's grace, they gave me life and instruction which mollified many of life's obstacles. Their love and kindness flood my thoughts often.

Mother, Father, I do my best to carry your lessons of virtue.

Athair ar neamh,

Bí thusa 'mo threorú i mbriathar 's i mbeart

Fan thusa go deo liom is coinnigh mé ceart

ACKNOWLEDGEMENTS

This work would not have been possible without the hard work and help of numerous people. Firstly, my wife Whitney for her steadfast encouragement during this endeavor. Secondly, the faculty and staff with the Electrical and Computer Engineering Department at Mississippi State University. The online classes are first rate and greatly enabled a deeper understanding of the material.

Dr. John Ball, Dr. Qian (Jenny) Du, and Dr. James Fowler's courses provided deep insight into the topics and the assignments greatly re-enforced the research aspect of the field. I am so very thankful for the opportunity to have learned from such great researchers.

Dr. John Ball, Dr. Ali Gurbuz, and Dr. Mehmet Kurum for being on my committee and their review of this work. Any mistakes are entirely my own.

Lastly, I would like to thank Dr. Robert Moorhead for taking a chance on me and his subsequent patience and encouragement while I was completing this work. Your timely words and guidance greatly helped me along the path of discovery.

To all, your kindness and the generosity of your time will not be forgotten.

TABLE OF CONTENTS

LIST OF TABLES

LIST OF FIGURES

ACRONYMS AND ABBREVIATIONS

1NN	1-Nearest Neighbor
AI	Artificial Intelligence
AR	Autoregressive
CNN	Convolutional Neural Network
DBN	Deep Belief Network
D-Coil	Differential Coil
DL	Deep Learning
DS	Dataset
DTW	Dynamic Time Warping
EC	Eddy Current
ECI	Eddy Current Inspection
ECIS	Eddy Current Inspection System
EDM	Electrical Discharge Machining
EM	Electromagnetic
EMD	Empirical Mode Decomposition
EMF	Electromotive Force
ESAX	Extended Symbolic Aggregate Approximation
FCM	Fuzzy C Means

FDI	Fraction of Defects Correctly Identified
FEM	Finite Element Method
FoV	Field of View
GLRT	Generalized Likelihood Ratio Test
GMM	Gaussian Mixture Model
GMR	Giant Magnetoresistance
HPT	High Pressure Turbine
IA	Information Augmentation
ICA	Independent Component Analysis
IQ	In-phase and Quadrature
JSD	Jensen-Shannon Divergence
KCD	Kernel Change Detection
KDE	Kernel Density Estimation
KLD	Kullback-Leibler Divergence
KNN	K-Nearest Neighbor
KPCA	Kernel Principal Component Analysis
LCSS	Longest Common Subsequence
LSSVM	Least Squares Support Vector Machine
MBR	Minimum Bounding Rectangle
ML	Machine Learning
MLP	Multilayer Perceptron
MLR	Multiple Linear Regression

MM	Mathematical Morphology
MRA	Multiresolution Analysis
NDE	Nondestructive Evaluation
PAA	Piecewise Aggregate Approximation
PCA	Principal Component Analysis
PCB	Printed Circuit Board
PDF	Probability Density Function
PEC	Pulsed Eddy Current
P_{FA}	Probability of False Alarm
PIP	Perceptually Important Points
PNN	Probabilistic Neural Network
PoD	Probability of Detection
PTA	Piecewise Trend Approximation
RBF	Radial Basis Function
RBFNN	Radial Basis Function Neural Network
RBM	Restricted Boltzmann Machine
ResNet	Residual Convolutional Neural Network
RFC	Retirement For Cause
RFEC	Remote Field Eddy Current
RKPNN	Rotated Kernel Probabilistic Neural Network
RMSE	Root Mean Square Error
RMSE	Root Mean Square

ROC	Receiver Operating Characteristic
ROI	Region of Interest
SAE	Stacked Autoencoder
SAX	Symbolic Aggregate Approximation
SE	Structuring Element
SG Tube	Steam Generator Tube
SNR	Signal to Noise Ratio
SoG	Sum of Gaussian
SoGFDE	Sum of Gaussian Feature Detection and Extraction
SoG-PAA	Sum of Gaussian Piecewise Aggregate Approximation
SoG-SAX	Sum of Gaussian Symbolic Aggregate Approximation
SOM	Self Organizing Map
SVM	Support Vector Machine
UCR	University of California, Riverside
USAF	United States Air Force
UUT	Unit Under Test
XAI	Explainable Artificial Intelligence

CHAPTER I

INTRODUCTION

Quantitative electromagnetic (EM)-based inspection methods have been used to determine the operational state of metallic components in numerous industrial applications. Some examples include: railway [1], steam generator tubes in nuclear plants [2], gas pipelines [3], and aircraft engine components [4]. In these industries, correct assessment of the state of the component is paramount to continued safe operation.

1.1 USAF Retirement For Cause (RFC) Program

The United States Air Force (USAF) has employed a Retirement for Cause (RFC) program for aircraft engine components since the 1980's [5-11]. The motivation for the program is to obtain cost savings by returning viable parts to service rather than replacement at predetermined component life intervals. Two key elements of the program are Nondestructive Evaluation (NDE) coupled with Fracture Mechanics analysis which are used to determine the viability of a given engine component as a candidate for reuse based on statistical models.

A core enabling capability to the NDE of engine components is the use of Eddy Current Inspection (ECI) techniques [12-14] to detect, localize, and describe near surface defects.

1.1.1 RFC ECI Components

Central to this study is the analysis of Eddy Current (EC) data that was collected as part of the RFC program. One common ECI technique used in the RFC program is based on the

Uniwest US-500 [15] ECI instrument which is a sub component of the Eddy Current Inspection System (ECIS). Pictorial representations of these components are provided in Figure. 1.1.

(a)

(b)

Figure 1.1 RFC ECI Components:

(a) Uniwest US-500 Eddy Current Instrument, (b) RFC ECIS [16,17].

Referencing Figure 1.1, the ECIS is a Gantry style robotic system that enables automated inspection of aircraft engine components. The US-500 eddy current instrument subsystem outputs horizontal and vertical channel (In-phase and Quadrature - IQ) data that represent the resistive and reactive impedance components detected by the EC probe. Additionally, the

instrument has the capability of programmatically setting the gain and frequency of the probe drive channel as well as bandpass filtering and phase adjustment of the return signal. These adjustments allow the inspector better control of inspection Signal-to-Noise ratio (SNR) and the ability to minimize liftoff effects (separation of the probe from the test specimen).

1.1.2 D-Coil Probe Design

EC Probes typically used in the RFC program are differential coil probes termed D-coil probes. Typical D-coil (a.k.a Split-D) EC probe design is comprised of two split receive coils wound 180° out of phase with respect to each other and encircled by a drive coil. A picture of the arrangement is shown in Figure. 1.2

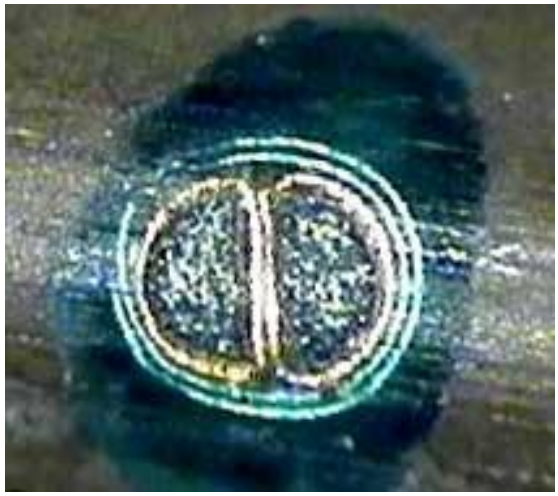

Figure 1.2 D-coil Eddy Current Probe

The green coil is the probe drive coil and inside this are the two receive coils wrapped around half-cylinder soft ferrite material. The coil is set in the probe shoe with an epoxy resin [18].

As a result of the D-coil probe design, the sensor is highly resistant to noise, however, when in the presence of a defect, due to the separation of the receive coils, the probe will present a typical signature response as indicated in Figure 1.3.

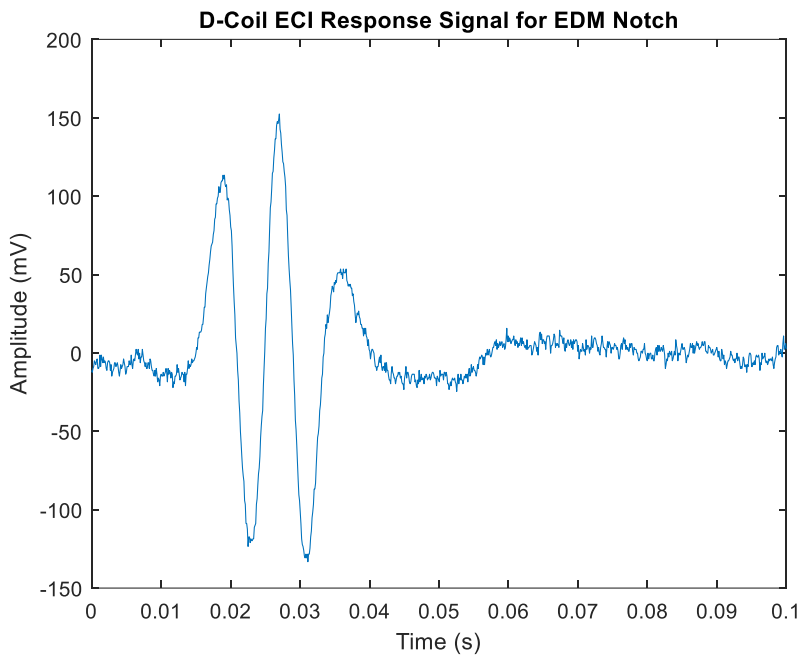

Figure 1.3 Typical D-Coil ECI Response Signal Scanning over Defect Vertical channel response line scan plot.

The defect response shown in Figure 1.3 was obtained by scanning the probe over an Electrical Discharge Machined (EDM) notch. The relevance of utilizing material defects created in this manner will be discussed later in this dissertation.

One immediate observation of the defect signature in Figure 1.3 is the appearance of Gaussian-like peaks that comprise the signal. Defect detection would be a fairly simple process if all ECI receive signals presented defect responses like the example in Figure 1.3. However, the ECI technique has numerous factors that can affect the defect signal appearance like

separation of the probe from the Unit Under Test (UUT) lift-off, coil orientation relative to the surface [19], receive coils geometrical relationship relative to the drive coil, defect orientation related to the receive coils, scan speed, and the volume of the UUT defect that is present in the reception field of the ECI probe.

To illustrate this last point, a series of plots are presented in Figure 1.4 which indicate responses typically seen for the vertical component of a D-coil type probe receive signal when the probe is indexed across a small (relative to the coil diameter) EDM notch while keeping the drive signal amplitude and frequency fixed.

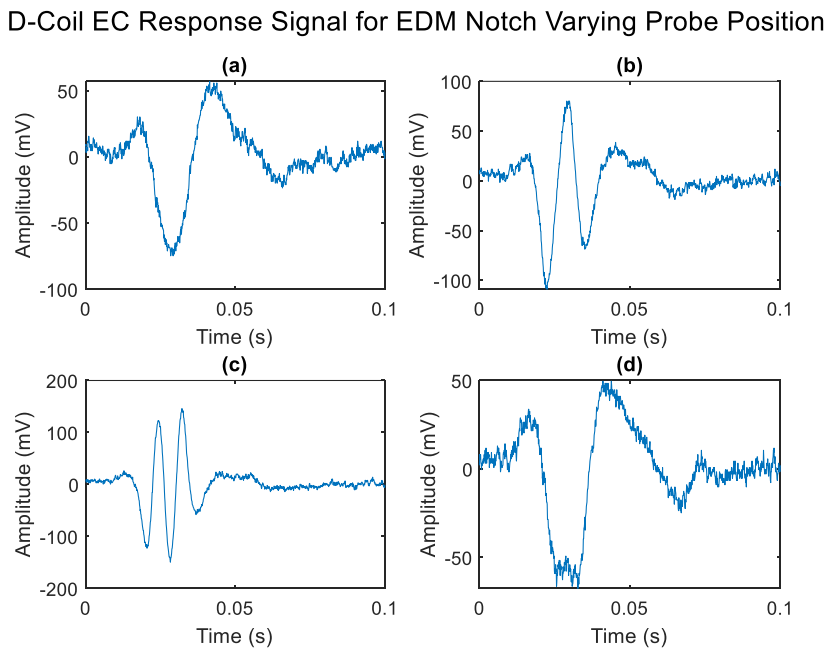

Figure 1.4 D-Coil ECI Response Varying Probe Position

(a) probe is approaching defect region, (b), (c) both receive coils sensing defect, (d) probe is leaving the defect region. (a)-(d) Note the changes in defect response shape and amplitude which are primarily due to the volume of the defect in the reception fields of the coils.

1.2 RFC ECI Process

In a much broader sense, the ECI process typically involves three steps: detection, localization, and description [20,21]. Detection and localization algorithms typically attempt to discover anomalies and determine the location of the suspect defective region using some set of features in the defect response signal. Lastly, the description process then attempts to describe the defect in term of dimension depth, length, shape or classify (characterize) the type of defect (e.g., corrosion, magnetite build-up) using the feature data.

Defect detection and localization in the RFC ECI system is primarily based on an amplitude feature in the defect response. This value is termed the "system response" and is used to calculate the defect depth or length using predetermined sizing models. Considerable detail regarding this approach to defect description is provided in [22].

1.3 Artificial Defects

As indicated in [22], ECI approaches that quantify material defects (cracks) usually employee materials that contain known defect regions for the purposes of demonstrating inspection coverage and to create models that relate the system response to known crack sizes. In many instances, EDM notches are created in the material to provide a known sized defect or as a seeding process to create fatigue cracks using additional procedures. There have been numerous studies (e.g. [23-25]) that indicate EDM features do not directly correspond to actual crack features. Nonetheless, EDM notches are often used to demonstrate the efficacy of defect detection and localization algorithms due to their similarity to crack responses, ease of manufacture, and lower cost when compared to actual crack samples.

1.4 Work Contribution Summary

In many EC analysis scenarios common filtering techniques can alter defect signature information in ways that can complicate further investigation. In these cases, many researchers rely upon time domain-based methods such as function approximation. To this end, the present work novelly contributes to the body of EC analysis knowledge in the following aspects:

- Describes the design and validation of a generalized method that can be used to decompose D-coil defect signatures as a summation of basic Gaussian functions whose parameters relate to the EC probe geometry and inspection properties.
- Demonstrates the efficacy of such Gaussian based representations in regards to improving the performance of relatively simple Machine Learning (ML) models that have easy to understand internals.
- Demonstrates the ability of such Gaussian based representations to improve relative peak amplitude and temporal fidelity of dimensionally reduced representations of D-Coil defect signatures when compared to other current similar methods.

1.5 Dissertation Outline

The remainder of this document is arranged in the following manner. Chapter 2 presents a literature review focused on quantitative EC analysis methods and the much broader field of time series analysis. Chapter 3 provides an analysis of the literature review to determine gaps and trends in research and it is in this chapter the dissertation hypothesis is presented. Chapter 4 provides a description of the datasets used in experimental investigations of the proposed methods. Chapters 5 and 6 present the proposed method and experimental results that are a main focus of this study, namely representation of EC defect responses as an add mixture of Gaussian functions. Chapters 7 and 8 provide case studies that demonstrate how the proposed method for defect response representation can increase the performance of existing ML methods. Lastly, Chapter 9 provides conclusions from the work and discusses possible future topics for research.

CHAPTER II

LITERATURE REVIEW

A literature review was conducted in the field of Quantitative ECI analysis and methods in an effort to identify the trends in research and to find possible gaps in existing knowledge.

From the review, a taxonomy was observed that the various approaches could be categorized in terms of two model types that were used to investigate the ECI method termed: Physics-based and Data-centric approaches.

2.1 Physics-Based Approaches

Physics-based EC analysis approaches primarily aim to analyze an ECI method using models that are constructed from electric circuit components and/or Maxwell's EM field equations in an effort to predict the outcome of a given EC problem using simulation via numerical methods or analytical expressions.

In the literature, there are excellent chronologies of progress of physics-based EC analysis approaches. Notable references are provided in [26-28]. Central to the progress of development of physics based ECI analysis is understanding the change of probe impedance (ΔZ) in the region of a material defect. This is termed the forward EC problem in the literature.

2.1.1 Forward EC Problems

The work of Libby [28] provided qualitative analysis of ΔZ using a transformer model of the probe impedance and the material defect. Burrows [29] provided a more quantitative

analysis by considering air-filled coils that were placed near small material defects. Using quasi-static representations of the Maxwell EM field equations [30], the Lorentz reciprocity relation, and simplifying assumptions from EM scattering theory, an expression for the flaw voltage was obtained which enabled predictive analysis of ΔZ in terms of flaw dimension and angular position of the flaw from the EC probe.

Later approaches studied EC analysis methods at microwave frequencies which necessitated a different theoretical framework. These approaches generalized Burrows work by utilizing concepts from microwave circuit theory [31,32]. The result of these studies provided exact values for ΔZ in terms of the field distributions of the probe in regions free of and in the vicinity of an arbitrary defect.

Modelling of the probe EM field distribution is not a straightforward process as there are many confounding factors that can influence the model. A considerable amount of research has been conducted to provide estimates of the probe field distribution for various ECI analysis scenarios. Probe field modelling for circular air-filled coils was initially undertaken by Dodd and Deeds [33]. Later work expanding the capability of probe field analysis using a Dyadic Green's function boundary integral approach [34] was undertaken by Bowler [35]. In [36], the method was expanded to allow 3D modelling of ferrite core probes and utilized optimization techniques to reduce computational cost when compared to Finite Element Method (FEM) based approaches.

As computational capability increased, numerous researchers utilized FEM approaches to analyze ECI scenarios. For example, Badics et al. [37], demonstrated the ability to model EC crack problems using FEM by introducing an algorithm to deal with zero conductivity flaws.

Bihan et al. [38], utilized both FEM and boundary integral methods in their calculation of probe response signals.

To this point, the discussion of methods of ECI analysis via physics-based methods have focused on the forward EC problem. The forward EC problem provides predicative capability of probe response based on a supplied probe geometry and defect type. However, in many ECI applications the inverse EC problem is of greater interest. The inverse EC problem seeks to provide quantitative information (e.g., dimensional size and shape) of the defect based upon a supplied probe response.

2.1.2 Inverse EC Problems

One early approach to the inverse EC problem was addressed in [39] for EC defects in circular tubes. The approach considered numerous inspection coils placed along the axis of the tube allowing a conductivity mesh of the suspected flawed region to be created. The geometry of the ECI arrangement greatly simplified the analysis and the calculation of the necessary Green's functions used in modelling the EM field in the flaw region. The resulting model produced the perturbed EMF of the coils which was then compared to the measured EMFs. Given an estimated conductivity distribution, an iterative least squares approach was used to optimize the model to the measured values.

A more generalized approach to EC inversion based on the boundary integral approach was provided in [40], that built upon the work in [35] and provided the capability to solve the inverse problem via the gradient of ΔZ in terms of a parametrized flaw model.

Numerical simulations used for the EC inversion problem are notoriously computationally expensive due to the need to iteratively solve the forward problem that has been parameterized in terms of a defect model. The inversion process iterates until the forward model

output signal is close enough to the actual measured values based on some predetermined minimization criterion. There has been considerable research into methods of reducing the number of iterations required to attain the inversion result. Li et al. [41], utilized a genetic search algorithm to determine the flaw parameters to use at each forward model iteration. Bilicz et al. [42] implemented a surrogate forward model using a Kriging interpolator to reduce the number of forward problem iterations. Douvenot et al. [43] utilized a surrogate metamodel of the forward process that was developed using Sequential Design, Radial Basis Functions (RBF), and Particle Swarm optimization. Bilicz [44], utilized the sparse grids concept to create a surrogate forward model to improve inversion performance. Other approaches such as that in [45] sought to decrease forward model computation time by using a Kernel Change Detection (KCD) technique [46], to localize the suspected defect regions.

In addition to study of EC inversion methods, research has also been conducted in regards to validating forward models with real world studies. Mooers et al. [47] conducted a study comparing the forward model described in [48] for EDM notches inspected by a split-D probe. The results of the study revealed some discrepancies between the forward model simulation results and the actual measurements attained.

Lastly, research has been conducted seeking to minimize another issue that presents a problem for EC inversion, namely noise. ECI approaches that inspect titanium are prone to grain noise which is a result of the crystalline structure of the material. This translates to noise in the probe response signal that can cause stability and accuracy issues for inversion methods. In [49] and [50] researchers attempt to address the issue by treating the outputs of the forward model as random variables and utilize a Bayesian Framework to describe uncertainty in the model.

2.2 Data-centric Approaches

Data-centric approaches to ECI analysis largely seek to analyze EC problems using learning and decision-based algorithms that perform operations on features derived from the probe response data. There is a trait in the approaches that detection, localization and/or description of the defect is provided at near real time and with little to no reliance on physics-based methods.

Literature review in the area of data-centric approaches revealed a low number of studies that solely focused on ECI equipment and UUT configurations similar to that employed in the USAF RFC program. However, there were a wide range of approaches that focused on other ECI UUT specimens (e.g., Nuclear Plant Steam Generator Tubes (SG)) and probe designs (e.g., bobbin coil, Giant Magnetoresistive (GMR), Printed Circuit Board (PCB)) that generated probe responses similar to those seen in the USAF RFC program.

It is noted that in the field of Machine Learning (ML), data features play a prime role. With this in mind, one logical taxonomy for the data-centric approaches previously studied would be to group them according to data representation. Largely, the studies in this area can be classified as Impedance Plane and Impedance Component approaches.

2.2.1 Impedance Plane Approaches

A number of studies extracted ML feature vectors from the Argand diagram (Impedance plane) representation of the complex impedance probe response data. Due to the physical separation between the receive coils in differential type probes, response signals typically trace Lissajous curves in the Impedance plane when scanned across a defect [51]. The shape or geometry of these geometric curves can be affected by the properties of the material defect and inspection frequency. It should also be noted that all things being constant for a given ECI setup

and defect, the curves are periodic. An example of such a signal for a D-Coil EC probe is provided in Figure 2.1.

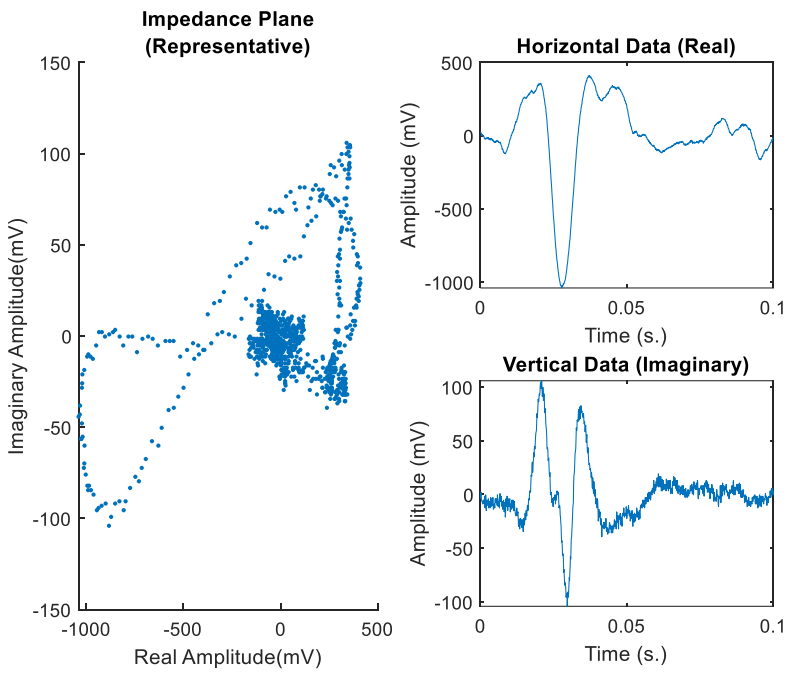

Figure 2.1 Lissajous Plot of D-Coil Probe Scanning over EDM Notch

D-Coil probe impedance component signals trace a Lissajous pattern in the impedance plane when encountering a flaw as seen on the left of the figure.

Lord and Satish [52] describe a detection and description scheme using features derived from the Fourier coefficients of the probe response Impedance plane curve. Detection and description were accomplished by comparing new feature vectors against samples stored in a database via the K-means method [53]. The efficacy of the technique was demonstrated by determining magnetite levels in SG tubes in a later study [54]. Jarmulak [55] described a detection method for SG tubes that employed a feature vector comprised of the wavelet transform [56],[57] of the angular directional change of the original Lissajous defect signature.

Due to the frequency partitioning (decomposition) nature of the Wavelet transform, the author claimed better fidelity in comparison between the stored examples.

Song and Shin [58] utilized physics-based models as a means to generate simulated probe responses for four categories of SG tube defects. Probabilistic Neural Networks (PNNs) [59,60] were used to detect and describe the class of the defect using the maximum impedance values and phase angle as well as the phase angle at the end of the impedance curve with features extracted at two ECI frequencies. Multilayer Perceptrons (MLPs) utilizing the backpropagating training algorithm [61,62] for each defect class were then used to determine the defect depth and width (EC inversion). The study reported a 91% classification accuracy. Jo and Lee [63] utilized the same dataset studied in [58] but improved the classification performance by reducing the number of features to three (3), using the maximum impedance value and phase angle as well as the width of the curve at half maximum. In addition, the study used MLP's for classification and inversion activities and investigated the performance when the responses were corrupted with additive white Gaussian noise. In the worst case, classification accuracy was > 90% and without noise corruption classification accuracy was perfect (100%).

In a more recent study by D' Angelo et al. [64,65] the defect Lissajous signature was partitioned into two regions (referenced to the null point) and the feature vector created from the phase angle, width, and length of the two subsignals collected with a GMR type EC probe. An experiment was conducted using Naïve Bayes [66], C4.5/J48 Decision Trees [67], and MLP networks classifiers that perform the EC inversion function. The dataset feature vectors representing probe distance from and scan angle relative to the defect were placed into classes based on the defect length, depth, and width. The area under the Receiver Operating Characteristic (ROC) curve was > 0.95 for all three classifier types.

Yin et al. [68] developed analytical models for variations of EC Lissajous curves which aided feature extraction via K-means clustering. The extracted features: petal width, maximal and minimal curve extents, phase angle, and petal symmetry were obtained from a steel test specimen that contained slots of varying depth. The features were then used as input to a set of six supervised classifiers. Overall, an average classification accuracy of 86.8% was observed across the classifiers. The K-Nearest Neighbor (KNN) classifier [69] had the highest accuracy at 87%.

Grman et al. [70] investigated the Lissajous curves obtained from EC inspection of nonmagnetic heat exchanger tubes that had numerous defect conditions (e.g., interior and exterior cracks, interior protrusions, exterior support plates, and through hole cracks). The study obtained representative feature vectors based on Fourier coefficients, maximal and minimal curve extents and phase angle. The feature vectors were then classified using MLP and PNN based classifiers. According to the study authors the PNN outperformed the MLP classifier, however, classification accuracies were not clearly stated.

In [71] an Adaptive Neuro-Fuzzy Inference Model was employed to estimate the percentage signal feature given the width and depth of defects sensed with a differential probe in a manual inspection scenario. The study investigated 60 data records with a 75/25% training/test data split and obtained an average error of 0.0023%

2.2.2 Impedance Component Approaches

Impedance component approaches process the EC signal by treating the resistive and reactive components independently or in terms of magnitude and phase. Some approaches operate on line scan/track data wherein the probe is moved once over the UUT and the measured impedance values are referenced by distance or time. As computational capability has

progressed many of the data-centric quantitative ECI approaches have gravitated toward digital image processing based techniques that operate on ECI image scan data. ECI scan images are created by assembling multiple line scans performed at predetermined spacing intervals to create an image of the UUT surface. ECI scan images are often termed C-Scans in the literature.

2.2.2.1 Line Scan Based Approaches

M. Das et al. [72] employed an approach from the field of Statistical Signal Processing [73,74] by first shaping the defect scan signals using a bobbin coil probe to remove low frequency content and then using a Generalized Likelihood Ratio Test (GLRT) scheme to detect defect regions in windowed portions of the signal. Lastly, classification errors were reduced by using a rule-based classifier which employed known features of the defect response.

Guepie et al. [75] modeled EC impedance components defect signatures using Autoregressive (AR) models and utilized the learned model parameters as feature vectors to classify twelve crack types in aluminum that varied in penetration angle and depth. The Support Vector Machine (SVM) [76] was utilized to classify the feature vectors based on the crack type and the results compared with feature vectors derived from Fourier coefficients. The AR model-based features outperformed the SVM classifier using Fourier coefficients by approximately 6%, achieving 98.75% in terms of classification accuracy.

Barcherini et al. [77] employed a binary Hopfield network [78] on signals from a Remote field ECI (RFEC) scenario. The method constructed down-sampled and quantized representations of exemplar probe response signals representative of material conditions to create a network that could classify material defect types (notch, corrosion, paint, cracks).

Angeli et al. [79] utilized a variant of the PNN, the Rotated Kernel PNN (RKPNN) [80], to classify two types of RFEC impedance response signals using a pancake coil [81] inspecting a

circular conducting plate. The study investigated the effectiveness of Gaussian, Laplacian, and Sigmodal kernels in the RKPNN. The RKPNNs utilizing Gaussian and Sigmoidal kernels achieved 100% classification accuracy on the test dataset.

In [82] the authors utilized 1-D Mathematical Morphology (MM) [83-85] operators to isolate and detect defects in EC line scans of probe response data from Jet engine rotary fan disks. The defect response signals were greatly affected by the background edge geometry effects of the UUT. Experiments were conducted with the algorithm using 16 separate differential coil probes each inspecting 30 fan disk slots of which 10 were seeded with EDM notches. The experiments resulted in only 5 missed detections.

Gao and Udpa [86] presented an adaptive 1-D MM algorithm to detect and localize defects in Aircraft wheels. The effectiveness of the algorithm was demonstrated visually by processing noisy ECI line scan data.

Other researchers investigated using features derived from algorithms that determined an orthogonal basis for the data and then utilized coefficients from the basis. An example of this is provided in [87] where the authors analyzed the performance of features extracted using Principal Component Analysis (PCA) [88,89], Coiflet Wavelet System ([90,91]), and Fourier descriptors against the block mean method in determining the location of fatigue defects in rivet holes in Aircraft lap-joints. The features were used as inputs to MLPs with the output signifying the location of the defect left/right. The researchers reported that all methods performed similarly (approximately 93% classification accuracy), but further analysis could not be made due to insufficient data.

Some studies utilized the wavelet transform and multiresolution analysis (MRA) to decompose the EC signal and then the hard thresholding technique [92] to remove coefficients as

part of denoising the EC signal. In [93] the authors utilized the Daubechies wavelet system [94] to denoise ECI line scan data collected from SG tube inspections. After denoising, an amplitude threshold technique was used for defect detection. Demonstration of the effectiveness of the method was shown through visual analysis of the effects of the algorithm on ECI scan data.

A data fusion technique was presented in [95] that utilized PCA, Independent Component Analysis (ICA) [96], Wavelet transforms, and Self Organizing Maps (SOM) [97] as methods to produce reduced representations (features) of ECI data. The features were then used as inputs to a MLP network to localize defects and provide EC inversion (width) information of circular defects in a metallic plate. The method sought to provide an alternative approach to address shortfalls of conventional PCA.

Ye et al. [98] used the Morlet (Gabor) Wavelet System [99,100] MRA coefficients obtained from EC line scans and Kernel Principal Component Analysis (KPCA) [101] to improve conventional PCA performance. The study investigated the improvement provided by KPCA for four classifier types (K-Medoids [102], KNN, MLP, SVM). The first experiment involved characterizing defects of varying depth with KCPA reducing classification error by an average of 3.6% over PCA. The second experiment involved classification of three corrosion type defects from a representative aircraft wing splice. The KPCA approach reduced classification error by 4.6% over PCA.

In [103], the authors employed KPCA to extract features and SVM and MLP networks to classify defects in aluminum Alloy plates of varying length and depth. The investigation studied the effects of varying probe excitation frequency (50 kHz. – 850 kHz.) on classification accuracy. KPCA based characterization schemes outperformed PCA schemes by an average of 2% for the drive frequencies investigated. However, both PCA-SVM and KPCA-SVM

classification schemes achieved 100% classification accuracy over a range of drive frequencies which may suggest that the SVM portion of the classifier was the more important element of the model.

One of the confounding aspects of the literature review regarding data-centric approaches to quantitative EC is that numerous studies present the EC analysis approach in tandem with an innovative probe design. One example of this is can be found in the work of Rosado et al. who developed a PCB based differential probe [104] and in a later study [105] investigated fitting Sum of Gaussian (SoG) pair models to FEM simulated ECI line scan data (using the PCB probe). The Gaussian pairs were used as inputs to a MLP network trained to characterize the depth and width of defects.

More recent studies have focused on Deep Learning (DL) methods [106,107]. In [108] the authors investigated Residual Convolutional Neural Networks (ResNet version 1, ResNet version 2, ResNeXTs) [109-112] that varied in dimensional depth and the number of modules employed in each stage of the four-stage model. The experimental setup consisted of a stainless-steel plate that contained rectangular notches of varied depth. The data set was collected by different inspectors, manually generating ECI line scans at differing angles and directions over flawed and unflawed regions of the steel plate. Training of the networks in the study took five days to complete, however, the ResNeXt based network of dimension depth 38 was able to attain a 93.58% classification accuracy determining the depth of the defects.

2.2.2.2 Scan Image Based Approaches

As stated previously, data-centric quantitative ECI scan image approaches process 2-D EC representations of the UUT surface. Often this image representation better reveals lift-off and surface conditions than individual line scan signals.

One example of ECI scan image analysis can be found in the work of Chady et al. [113-115]. The latest work [115] employed an EC probe that consisted of dual exciter coils in quadrature and a single pickup coil as part of a multi-frequency ECI system that generated Spectrograms of defects. EC inversion was performed to recover the 1D profile (length and depth) of the EDM defects created in Inconel 600 plates. The study investigated the performance of various feature sets consisting of Spectrogram peak values and coefficients obtained from analytically fitting the signals using the SoG approach and the frequency characteristic as a damped exponential. The SoG approach was used to combat in-band noise present in the probe response signals. Various levels of SNR (0 – 40 dB) were studied. Inclusion of the analytical coefficients as features greatly reduced inversion error (~ 40%).

The authors in [116] investigated the effectiveness of using Kullback-Leibler Divergence (KLD) [117] as a means to detect and characterize ECI defects in terms of length and depth. The study analyzed a multi-frequency (0.8 – 6 MHz.) ECI scenario wherein a pancake style probe was indexed across a nickel super alloy plate that contained EDM notches of varying length and depth and identical width. Even though the data collection generated ECI scan images, the spatial information between line scans was not directly used due to aggregation of the probe response amplitudes to construct estimated probability density functions (pdfs) of the flawed and unflawed regions of the plate using only the Imaginary component of the probe response and Gaussian Kernel Density Estimation (KDE) [118]. KLD was compared to the first four statistical moment measures and visually shown to be superior in performance in detecting defects with lower probability of false alarms (P_{FA}) occurrence. In addition, the study authors used the PCA eigenvalues obtained from the multi-frequency probe response KLD, mean, variance, and maximum amplitude to discriminate flaw length and depth.

In a later study [119], the Jensen-Shannon Divergence (JSD) [120] was investigated using the same inspection setup as in [116] (but with a much larger dataset size) as a method to detect and localize defects. However, the method utilized both impedance components and preprocessed the signals with FastICA [121] and then further decomposed using the Daubechies Wavelet System MRA Level 5 approximation signal coefficients as the source for estimated pdfs of the flawed and unflawed probe response signals. The work compared the JSD discriminative efficacy against the KLD method in [116] and CUSUM [122,123] at varying levels of SNR (0 – 20 dB) with JSD clearly outperforming the other two methods as primarily demonstrated through ROC curves.

Other data-centric quantitative ECI studies have focused on quantifying uncertainty in the model and/or data, thereby providing greater information regarding the interpretability of the results. Rather than only supplying a defect detection call, a bootstrapping method [124] was employed in [125] which modelled subsets of the training data with replacement (features used were the peak-to-peak value of Real and Imaginary components in the regions of interest (ROI)) using Gaussian Mixture Models (GMM) [126] over numerous iterations to determine class conditional pdfs and then Bayes theorem was used to calculate the posterior probability pdfs for each class. The estimated class conditional pdfs were combined with the test data estimated noise pdf to obtain a weighted posterior pdf to which the bootstrap method was again applied. The result was a pdf from which a classification confidence value was obtained. The study analyzed 10 SG tubes containing 21 defects and verification of the technique was through visual analysis of ECI scan images.

The method in [125] was later incorporated with an ensemble-based defect classification scheme [127],[128] based on Adaboost [129] wherein the hypothesis was modified at each

iteration by the class posterior probability confidence value. The test results indicated a 4.47% decrease in detection error rate when compared to the unmodified Adaboost algorithm.

In addition to DL approaches processing ECI line scan data, DL approaches have also been used to analyze ECI scan image data. In [130] the authors constructed a two-stage model consisting of a Deep Belief Network (DBN) [131] which consists of multiple stacked Restricted Boltzmann Machines (RBMs) [132] for feature extraction. Next, the Least Squares Support Vector Machine (LSSVM) [133] was used to develop a regression model relating the extracted features to defect descriptions. The study investigated ECI real component scan images of Titanium sheets that contained rectangular and circular EDM defects of varying length/diameter and depth. Comparisons were made of the DBN-LSSVM model against similarly sized models using PCA, RBM, and MLPs in the initial feature extraction stage and Multiple Linear Regression (MLR) [134] and LSSVM in the second stage. The DBN-LSSVM outperformed the other models in terms of repeatability and relative error in characterizing the scan image data in terms of diameter/length and depth. An interesting result of the study was that the DBN performed better regardless of the second stage used. This indicated the features extracted by the DBN were more discriminative. In addition, the LSSVM outperformed the MLR by roughly one order of magnitude which is of indicative of its superiority in representing the nonlinear relationship between the features and defect dimensions.

In [135], a Convolutional Neural Network (CNN) [136] was used to classify the depth and length of rectangular defects in a titanium sheet similar to that studied in [130] using the real component ECI scan images. The CNN model performance was analyzed by comparison to DBN, Stacked Autoencoders (SAE) [137], and SVM classifiers. The CNN consistently outperformed the other classification models with classification accuracy > 99%. When the

trained models were subject to Gaussian noise (SNR 30 – 95 dB), the classification accuracy of the CNN decreased to < 96% in the worst case (SNR 30 dB). However, when the CNN was trained with a subset of noised ECI scan images added to the dataset the classification accuracy modestly improved to > 98% when SNR=50 dB. Although the model training time was not directly mentioned in the paper it was inferred to be an issue as it was listed as a focus on future research.

Zhu et al. [138] constructed a CNN to detect defects in ECI scan images of SG tubes. The algorithm used Robust PCA (RPCA) [139] as a preprocessing step to suppress background features and enhance ROIs. The CNN used for the detector utilized binary cross entropy [140] functions for each class (defect/non-defect) to form a linear relation for the total cost model. This allowed the addition of a parameter (λ) to provide a greater penalty cost to errors related to defect classifications. In contrast to the CNN used in [135], the study introduced an adaptive strategy [141] for the CNN learning rate. In addition, the method estimated uncertainty in the detection result by calculating the sample mean and variance from the CNN dropout [142] during the testing phase. Performance of the network was analyzed by calculating the fraction of defects correctly identified (FDI) and the classification (detection) accuracy for a range of λ ($1 \leq \lambda \leq 11$) and decision thresholds θ, ($0.1 \leq \theta \leq 0.9$). The optimal FDI=0.991 and accuracy=0.981 was achieved when λ=1.1, and θ=0.4. This was an interesting result in that it is very close to the unweighted cost function and the optimal decision threshold was very close to the mid-range of the decision threshold.

2.3 Symbolic Representation of Time Series

Much of the literature review to this point has focused on EC defect response features selected by the researcher or in the case of DL approaches learned by the algorithm. In a more

general sense, EC defect responses can be considered as time series and there is another area of research that investigates the development of symbolic representations of time series which greatly aid data mining operations.

According to the creators and the custodians of the University of California, Riverside (UCR) Time Series Archive [143], data mining of time series at least started in the 1990s with the work of Agrawal et al. [144]. The research is relevant in that time series are typically high dimensional, requiring dimensionality reduction techniques that permit effective analysis with ML methods. These dimensionality reduction techniques create a symbolic representation of the time series under study.

A more recent survey of the symbolic representation of time series methods categorizes such approaches as "Feature-based Time Series" analysis [145]. In the work of [145], two type distinctions are made in feature-based time series analysis in terms of how the spatial/temporal ROI is partitioned to obtain the features. The feature types are referred to as global and subsequence.

2.3.1 Global Feature-Based Time Series Analysis

Global features typically utilize features extracted for analysis by considering the entire temporal interval of study. Examples of such previous methods used for mapping the time series to a feature space (and subsequent extraction) from the quantitative EC analysis literature review include Discrete Fourier Transform, PDF similarity, PCA, and Lissajous signature analysis.

2.3.2 Subsequence Feature-Based Time Series Analysis

In contrast to global features, subsequence features are obtained by partitioning the ROI in terms of spatial/temporal boundaries and extracting features from the partitioned intervals resulting in a symbolic representation of the time series subsequences.

As an example, Piecewise Aggregate Approximation (PAA) [146-148] approaches first partition the ROI using Haar basis functions of identical time scale width that span the interval and then obtain the arithmetic mean for the samples in each subinterval. It is noted that the PAA approach differs from the Haar wavelet transform in that the Haar wavelet transform utilizes differing time scales of orthogonal basis functions to decompose the signal into frequency bands. Thus, the Haar wavelet system and wavelet systems in general can be problematic for applications such as spatial/temporal comparisons (data mining) of time series.

Piecewise Trend Approximation (PTA) [149,150] decomposes a time series based on a ratio measure of the difference between successive sampled values (i.e., trend ratio). Further dimensionality reduction is achieved by determining subsequence trends in the time series by using the sign change locations in the trend ratio sequence and a predetermined trend ratio threshold. The resulting segmented time series is again dimensionally reduced by calculating the segment trend ratio using the values from the detected segment end points.

Other researchers provided algorithms that are based on a form of down sampling. Perceptually Important Points (PIP) [151] is an example of such an approach in that it utilizes a bisection-like segmentation algorithm to locate a predefined number of extrema within a ROI, starting with the sampled values at the beginning and ending of the interval.

Along with algorithms that directly perform dimensionality reduction on time series, other methods attempt to reduce dimensionality by locating interesting patterns in subsequences

of time series. One such example, shapelets [152] achieve dimensionality reduction by locating subsequences in a time series that are highly representative of the class of the time series. Stated differently, provided a dataset consisting of two classes of time series examples discovered shapelets can be used to perform binary classification. In the original development, the shapelet subsequences are obtained by sliding a window across the time series in the dataset and locating subsequences that minimize intraclass distance while maximining interclass distance as measured by information gain of the partitioned dataset.

Discovery of shapelets due to the sliding window technique can be excessively time consuming. Further developments in the field have sought to decrease the discovery process. Abdullah et al. [153] utilize intelligent caching and pruning of the discovery space. The authors in [154] reduce shapelet discovery time by learning subsequences which optimize a classification objective function. In [155] the authors reduce discovery time by utilizing the generalized eigenvector method [156].

Motif [157-160] discovery is another time series analysis technique that locates common subsequences in time series with a goal of summarizing the time series in terms of the common patterns. The algorithm requires a range parameter to ensure that trivial matches which are close to the first detection of a Motif subsequence do not adversely affect the results.

By contrast to motifs, discords [161-163] locate the most unusual or anomalous subsequences in time series. Locating discord subsequences in a time series is accomplished by using a sliding window of predetermined length and calculating from all possible time series subsequences the subsequence that has the largest not trivial match distance. As with shapelets, discovery of motifs and discords can be time consuming tasks. Some researchers have investigated methods to reduce the time necessary for the discovery process. An example of

such a method is provided in [164] that utilizes prior subsequence frequency information and Markov models in the detection of unusual subsequences.

The literature review of EC analysis methods revealed few examples of data-centric methods that utilized subsequence-based features as previously mentioned. Wavelet-based approaches used in EC analysis methods provide the ability for time-frequency series analysis, but have been used for defect response denoising in some applications. In other analysis methods, a subset of features extracted from the wavelet decomposition procedure have been used for classification (e.g., defect type) and inversion applications. Few EC analysis studies which have used PNNs for classification of defect types appear to have used the time series defect response without dimensionality reduction of the defect signatures.

2.3.3 Feature-Based Time Series Similarity Search

A central enabling concept for feature-based time series analysis are measures of distance or similarity between sequences. One feature-based time series analysis technique not discussed to this point, but directly related to similarity measures is similarity search (also termed indexing or template matching [165]). Indexing applications are employed when the analyst needs to determine the prevalence of a template sequence in a time series dataset. Indexing queries return sequences in the dataset that match the template in accordance with a predefined query criterion.

There exists a considerable amount of research literature regarding indexing techniques for symbolic representations of time series. Examples of such works can be categorized in terms of the similarity measure employed.

Dynamic Time Warping (DTW) [166-169] approaches attempt to account for the fact that frequently, time series sequences may exhibit high similarity but are delayed in time relative to

one another and thus not aligned. DTW attempts to warp the time axis which permits sequence alignment according to a desired minimum distance criterion.

Tree Data Structure [170-177] approaches to sequence similarity construct hierarchical models of regions in the feature space which serve to localize similar features. The models can then be represented using tree data structures to efficiently find sequences that match a specified template.

Other approaches to similarity search of symbolic representations of time series are based on approaches commonly used in text-based similarity searches.

Longest Common Subsequence (LCSS) [178-183] is a method based upon dynamic programming that identifies the longest subsequence between an unknown time series representation and the template. Such methods typically allow omissions between sequence elements being compared and similarity is measured by the number of elements in the LCSS.

Edit Distance [184-187] is another similarity search method that considers the symbolic represented time series as strings from a predefined alphabet and calculates the number of edit operations necessary to make the sequences consistent. In such methods a cost function must be defined for insertion, deletion, and substitution operations and similarity is judged by a minimal threshold criterion.

Lastly, some approaches to similarity search in symbolically represented time series employ methods based on l_p norms [188,189]. These approaches determine similarity by calculating the l_p norm between the two time series representations. One very common measure used is the Euclidean distance (l_2 norm).

CHAPTER III

ANALYSIS OF PREVIOUS QUANTITIATIVE EC RESEARCH

The literature review revealed a number of gaps in existing knowledge some of which provide motivating factors for the dissertation hypothesis. The factors are discussed in the following sections of this chapter.

3.1 Issues with Physics-Based Model Approaches

3.1.1 Simulation Issues

As indicated in the literature review, EC inversion physics-based model approaches although rigorously grounded in scientific models suffer from numerous issues. One of the issues mentioned frequently in the literature is that the problems are not well-posed in the Hadamard sense (e.g. [43,190]). In addition, some forward model validation studies (e.g. [47]) indicated discrepancy between the validation and forward model simulation. Other studies (e.g. [49,50]), addressed methods to handle various noise sources that can have a detrimental effect on the inversion accuracy. Studies such as [191] indicate the need to consider the influence of multiple cracks in close proximity to one another during inversion analysis as these can influence the shape of the defect response.

3.1.2 EC Probe Variability

Another issue is the need to account for all relevant sources of the EC probe geometry in the simulation. An example of this can be readily demonstrated in the case of EC simulation

analysis that utilize D-coil type probes. There are a number of factors in the probe construction (e.g., coil set back, orientation of the coil within the shoe) that can significantly influence the estimated probe response [192] and must be accounted for to attain more accurate inversion results.

3.2 Issues with Data-Centric Approaches

3.2.1 Dimensionality Considerations

Data-centric approaches to EC problems typically involve hand selection of features or in the case of DL features learned by the algorithm. Largely, these approaches exhibit one common characteristic, dimensionality reduction in the pre-processing stage. As pointed out in [193], data pre-processing can have an immense effect on the performance of a ML based system. Properly reducing the number of inputs to a ML algorithm can have the effect of providing a better representation of the pdf for the input features. This is readily demonstrated in EC scan image-based approaches of [116] and [119] where the ECI data was aggregated and used to develop estimated pdfs for the defect/non defect regions at the expense of losing spatial/temporal representations of the data. Dimensionality reduction allows the ML algorithm to avoid the commonly known pitfall of the “curse of dimensionality” [194].

In addition to dimensionality reduction, in the case of ML classifier algorithms (which are many times used in data-centric EC inversion approaches), input features that are highly discriminative can greatly increase the accuracy of the classifier. An example of this can be seen in [195], where the authors mention that data-centric analysis approaches that rely solely on ECI Lissajous responses for features in the analysis of defects from voids or non-metallic particles could be problematic due to the close similarities among the responses for different defect classes.

3.2.2 Noise Effects

EC line scan signals are representative of a nonstationary process [196] that is affected by nonlinear dynamics (e.g., temperature, material surface condition, defects, etc.). The significance of this fact is that the time-frequency aspect of the phenomena usually must be considered in the analysis to gain greater understanding. Previous Spectrogram and wavelet decomposition ECI analysis methods can facilitate time-frequency analysis; however, in-band noise in the defect response signature which cannot be effectively removed can present problems. Empirical Mode Decomposition (EMD) [197,198] which decomposes a signal using envelope information into intrinsic mode functions representative of frequency bands inherent in the signal, have been employed in EC analysis of SG tube defects [199] and defect detection using Pulsed Eddy Current (PEC) [200]. However, EMD does suffer from issues such signal spikes (noise) and other issues as described in [201]. In these aforementioned cases, ML models should be verified at regular intervals to ensure that nonstationary effects of the phenomena are not adversely affecting the ML model.

Noise removal is another process that can have detrimental effect on the accuracy of data-centric EC analysis approaches. As indicated in the literature review, varied wavelet systems have been used in the analysis of ECI data. In [93], a hard thresholding technique was used to remove noise from the EC response. Such approaches can be quite effective provided that the noise is not in the frequency band of the EC signal, however, as pointed out in [115] in some cases complete noise removal is not possible. Care must be taken using the reconstructed EC signal to extract features for a ML algorithm as artifacts from the wavelet basis functions can be present that can negatively affect amplitude-based features in the defect response (e.g. [202]).

Other noise abatement algorithms such as median filtering [203], can also negatively impact EC line scan ML approaches that extract amplitude-based features if the window is not properly sized. Some researchers (e.g. [204]), have attempted to fit the noise using analytical based models (e.g., polynomial surfaces) in ECI scan image approaches to improve the detectability of defect signatures by removing low frequency trends in the image. Care must be taken when using these approaches to quantify any distortion to the remaining defect signature.

3.2.3 Training Time

Lastly, as indicated in [108] and alluded in [135], DL networks can exhibit fairly long training times in a tradeoff for robustness of the model as indicated in [108]. It is possible that future research in feature representations could provide information to reduce training times in DL methods by providing more focused feature learning algorithms for these methods.

3.3 Lack of Research in Robust Automated Defect Detection and Feature Extraction

Much of the existing EC research focuses on techniques that improve physics-based model performance in both forward and inverse problems. Data-centric EC analysis approaches largely focus on algorithm development and defect description with little discussion on defect detection and or feature extraction. For instance, in [115],[116],[119] which are EC scan image-based approaches, suspect defect regions appear to be inspector selected or based upon amplitude thresholding with little discussion of the method used. Despite the vast literature concerning data-centric EC analysis techniques, opportunities do exist for automated EC line scan defect detection and feature extraction techniques that are resilient to decreased SNR situations which are not typically investigated in laboratory scenarios. In addition, such detection techniques should provide ample response information from which metrics can be obtained to both assess

the confidence in the detection result and to build response quality models. Lastly, such detection techniques should provide the ability to compare defect responses and analysis methods which is another lesser studied area discovered from the literature review.

3.4 Lack of Explainability/Interpretability in Many Quantitative EC Models

One common observation made in data-centric and physics-based EC analysis approaches was the lack of uncertainty information provided with the output of the analysis model. More recent research (e.g. [49],[50],[125]) has begun to focus on the issue. On a larger scale, ML based approaches are often seen as black box models and research efforts have focused on Explainability and Interpretability (Explainable Artificial Intelligence – XAI) of the black box models typically to aid human understanding [205-210]. At a basic level, Explainable ML approaches create explanation models that attempt to explain the validity of the black box model result to the human user. These approaches can have issues such as how the automation model is validated in [211] or from the lack of constraints in the solution space that correspond to domain knowledge as discussed in [212]. In [213], the authors mention that one approach to the problem is to construct "simple models with clear internals" (e.g. [214]) as a means to increase interpretability of the ML model.

Many ECI scenarios are used to determine the operational state of the UUT as a precursor to a decision of its suitability for continued service. Therefore, it is critical that data-centric models used for this purpose possess highly interpretable and explainable characteristics. In [215], the authors stress the need to view AI or ML solutions within the context of Information Augmentation (IA) [216-225] for the analyst or inspector.

In either approach, possessing numerous ML models that tackle the problem in differing ways may be one way to increase the analyst's understanding of the phenomenon under study

3.5 Dissertation Hypothesis

Considering the motivating factors discussed, this dissertation will attempt to answer the following hypothesis:

Is it possible to improve highly interpretable data-centric EC model(s) that can detect and quantify in a novel and meaningful way various defect response signatures obtained by a D-coil based ECI system for the purposes of better enabling data mining functions?

Central to the hypothesis statement is the concept of interpretability. In the context of this dissertation, interpretability will be defined as possessing the following narrowly defined attributes:

- The data-centric models must possess IA attributes in that they facilitate efficient querying of past defect signatures which is a common data mining function.
- Defect response alternative representations possess simple to understand features and concepts.
- Defect response alternative representations facilitate the ability to identify relevant anomalous features in the defect signature.

3.5.1 Method Outline

The method proposed to answer the hypothesis will be composed in two parts and will focus on dimensionally reduced SoG representations of D-Coil defect responses. It will be demonstrated that such representations can significantly boost the performance of interpretable ML classification and function approximator designs. Description of the constituent methods and their rationale are provided in the following sections.

3.5.1.1 Automated SoG Surrogate Modeling of D-Coil EC Line Scan Data

In many quantitative EC research approaches, the published probe response signals have a Gaussian-like appearance (e.g. [226-236]). The Gaussian property of defect responses has been exploited in previous research using a SoG approach as indicated in the literature review. Specifically, the SoG approach has been used to characterize EC defects in terms of position, width, and depth using collections of Gaussian pairs and an artificial neural network [105]. In another EC analysis study, the SoG approach was utilized to combat in-band noise in the defect response [115]. However, these approaches assumed prior knowledge of the number of Gaussian elements present in the defect signature.

As indicated in Figure 1.4, typical D-coil EC line scan probe response signals to have a Gaussian-like appearance, but they vary in the number of Gaussian-like elements and are often asymmetric in appearance. Therefore, an automated approach to approximation of D-Coil defect response signatures via SoG elements must be able to reliably determine an indeterminate number of SoG elements.

Numerous Gaussian curve fitting approaches utilize the fact that the exponential term of the Gaussian function is quadratic. Using this feature, the curve fitting problem is reduced to a quadratic line fit by taking the logarithm of both sides of the Gaussian equation [237-240]. Implicit in the efficacy of these approaches is that the ROI is sufficiently isolated and not strongly influenced by other Gaussian signals in the vicinity and that sufficient data points exist in the ROI to reliably determine a candidate fit.

However, the number of data points that represent an EC defect signature can be rather small, corrupted by colored noise, and in the immediate vicinity of other Gaussian-like signals of interest. This can present problems for algorithms that utilize quadratic line fitting.

Other approaches to curve approximation utilize a SoG approach with one notable example being a technique that transforms the original signal into a scale-space representation [241] and then processes the transformed signal to obtain the initial Gaussian parameters which are then optimized via the Marquardt algorithm [242].

Typical D-Coil defect response signatures, due to probe geometry and scan speed for small defects typically only require a small range of σ (width) values of interest for analysis. Scale-space filtering approaches could possibly yield SoG fitted parameters that are outside the realm of interest for the analyst.

The presented algorithm makes no assumption as to the number of Gaussian-like components in the D-Coil defect signature, addresses the asymmetric nature of the defect response signatures, and provides the analyst tunable parameters along with a method to capture SoG features in the defect response signals based on probe geometry and scan speed.

Central to the presented method is the application of MM-based filtering. MM based operations are not just limited to single frequency EC analysis, but are often used in other EC analysis methods such as PEC (e.g. [243]). Of the MM filtering-based EC filtering techniques surveyed, an interesting trend was observed: non-binary MM approaches were used when investigating an individual ECI scan whereas binary MM approaches were used when filtering C-scan EC images. However, in both cases the filtering kernel used was based on a model of the entire EC defect signature. The presented algorithm attempts to decompose the defect response by utilizing only a MM filtering kernel modelled on a hypothesized portion of the EC defect signature as a means to build a complete defect response signature model.

As indicated in the literature review, in many applications an EC defect signature feature like peak amplitude is used to characterize the defect. The proposed algorithm provides greater

information about the defect signature that can greatly improve the reliability and precision of the characterization processes that rely on this feature.

The proposed method employed in this study draws upon the Parzen-Rosenblatt method [244,245] often utilized in KDE but in the present case it is used to create two 2-D Gaussian image matrices of the positive and negative partitioned 1-D D-coil EC line scan signal. The resulting image matrices are then binarized and subject to binary MM operations which were used to further isolate and detect the SoG features in the signal. This was accomplished by selecting a structuring element (SE) and expected width parameter that places a lower and upper bound on the width of a detected SoG feature. Once the initial candidate SoG parameters (amplitude, mean, and standard deviation) are obtained, they are subject to a two-phase constrained optimization procedure using the interior point method.

Significant time reduction can be realized in the optimization fitting procedure methods and similarly the training procedure in Neural Network methods by restricting the solution universe to the area of interest. In the case of the presented algorithm, the parameters optimized are constrained using range information obtained from the detection portion of the algorithm. The adaptive constraints employed ensure that the fitted SoG features are within the solution universe expected by the analyst. The constrained optimization procedure employed utilizes a two-pass approach. The first pass fits the SoG parameters to each detected Gaussian-like signature individually, then another pass is executed using all the parameters from the first pass and fitting the entire response holistically. The second pass was performed to seek a better fit to the defect response signature by considering mixtures of adjacent SoG features in the approximation. The output of the optimization procedure is a set of SoG parameters (amplitude,

mean, variance) that represent the defect response signature and achieve significant dimensionality reduction.

3.5.1.2 Symbolic Representation of Defect Responses via SoG Features

As indicated in the literature review, previous research regarding analysis of symbolic representations of time series are largely general-purpose algorithms in that they do not directly exploit known properties of the signal characteristics. In many circumstances this is due to consideration of the speed of the algorithm due to the time cost of the search procedures. In many instances attempts are made to learn the signal properties. To study the benefit of utilizing the Gaussian properties in defect responses two case studies were investigated.

In the first case study, a collection of Gaussian features was created by amalgamating normalized SoG features extracted from numerous D-coil defect response signatures. Clustering methods were utilized to determine classes of the SoG elements based on feature amplitude and width. The resulting cluster information was then used as part of a novel enhancement to methods that utilize PAA which boosts its classification accuracy

In the second case study, the SoG representation of the D-Coil defect responses were used as inputs to processes that created symbolic representations in an effort to boost the classification accuracy for an interpretable ML classifier often utilized in the EC analysis literature, the PNN.

CHAPTER IV

DATA SOURCE DESCRIPTIONS

The datasets used for this study were collected using the USAF ECIS during various probe calibration operations on differing materials and equipment configurations.

4.1 Data Collection Procedure

Immediately prior to an ECIS inspection, the probe undergoes a calibration procedure to determine the optimal response of the probe as measured by the extrema amplitude extents in the vertical channel. The procedure entails an automated raster scan over an EDM notch in predefined index increments for a specified number of individual line scans.

At the end of the calibration response search procedure, the probe is robotically moved back to the index where the maximal response was detected and the probe drive gain is automatedly adjusted until the extrema response amplitude attains a predetermined acceptable range.

Table 4.1 provides a summary of the ECI parameters used for collection and the UUT material of the datasets and Figure 4.1 provides a simplified diagram of the inspection setup.

Table 4.1 Study Dataset Summary

Dataset ID	Nominal Coil Diameter (In.)	Material	Coil/Notch Orientation	Index Distance (In.)	No. Line Scans/Sequence	No. Samples
DS1	0.040	Inconel	Transverse	0.005	25	50
DS2	0.020	Titanium	Transverse	0.010	10	50
DS3	0.040	Inconel	Transverse	0.005	25	2375

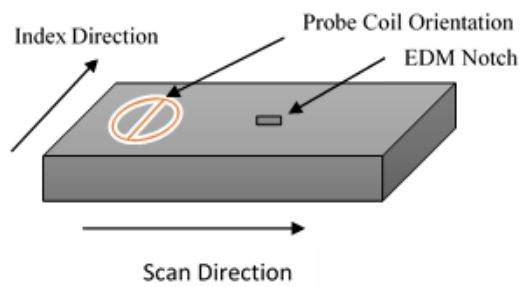

Figure 4.1 Simplified Diagram of ECI Setup

The centerline of the D-coil is transverse to the EDM notch on the UUT.

As indicated in Figure 4.1 at each line scan, the volume of the EDM defect region in the probe reception field varies. It is also noted that the diagram does not reflect possible differences in coil orientation due to probe manufacture or system alignment.

4.1 DS1 Dataset

DS1 consists of data from two separate calibration sequences and was collected using a test frequency of 2 MHz (which is common to the ECIS) at a scan rate of 5 in./s. An example of the line scans in DS1 is provided in Figure 4.2.

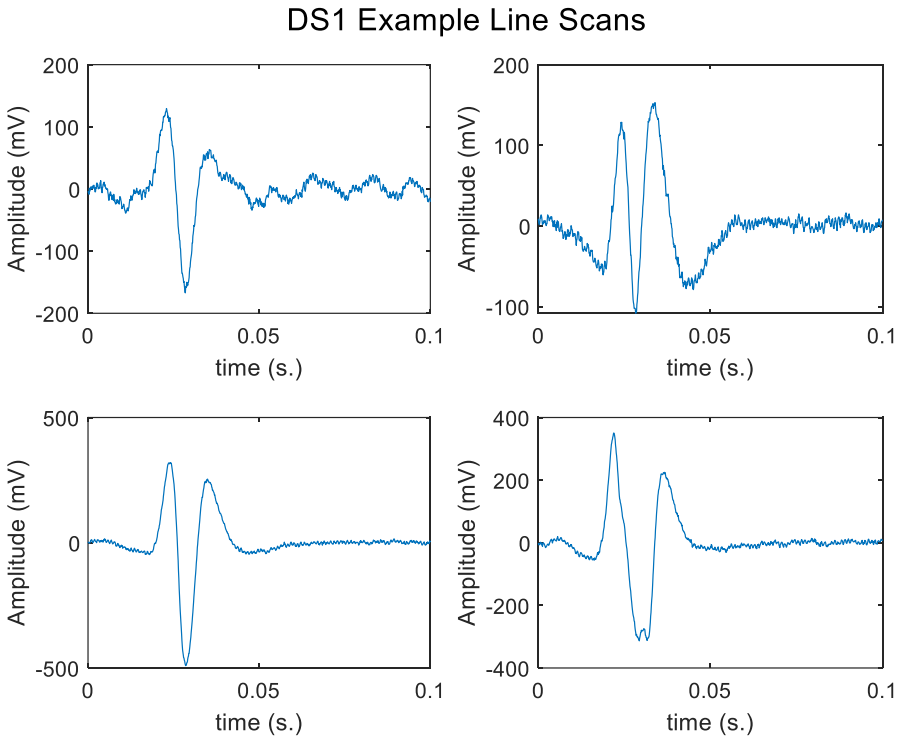

Figure 4.2 DS1 Example Line Scans

Referencing Figure 4.2, the ROI contained one EDM notch (dim.: 0.010 (l) x 0.004 (w) x 0.006(d) in.) in all instances. The defect response is located in the region ($0.01 \leq t \leq 0.06\ s.$) in all cases. Noise was estimated in an area known to not have a defect which was the time interval ($0.07 \leq t \leq 0.1\ s.$).

4.2 DS2 Dataset

DS2 consists of data from seven separate calibration sequences in a manner similar to that described for DS1. However, DS2 was collected with a test frequency of 6 MHz (due to the effect of increased surface noise of titanium at lower frequencies via the skin depth phenomenon) at a scan rate of 0.83 in./s. An example of the line scans in DS2 is provided in Figure 4.3.

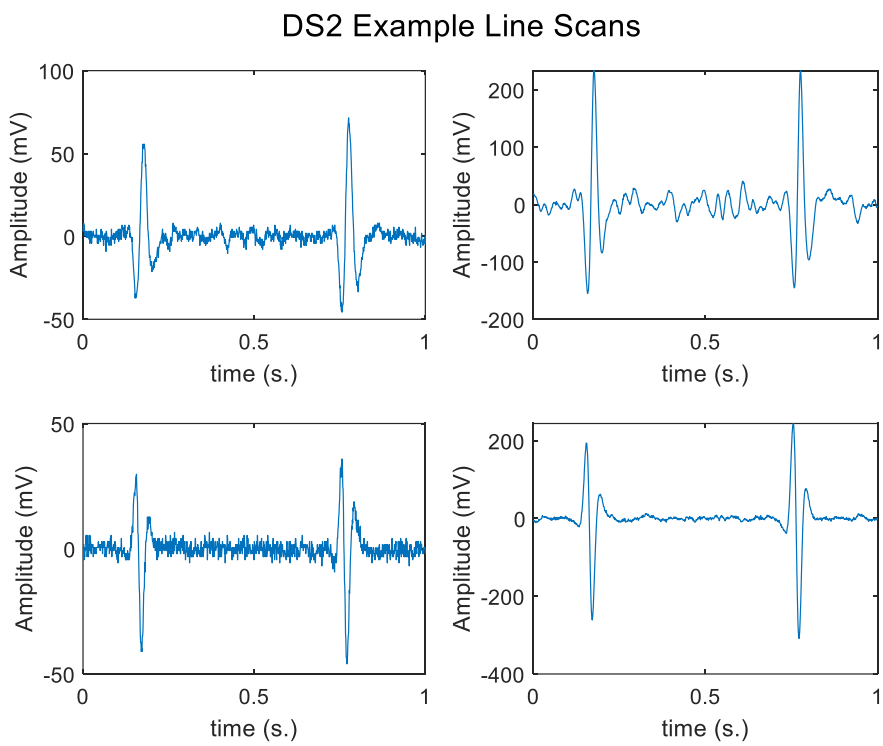

Figure 4.3 DS2 Example Line Scans

Referencing Figure 4.3, the ROI contained two EDM notches (dim.:0.010 (l) x 0.004 (w) x 0.006(d), dim.: 0.010 (l) x 0.004 (w) x 0.009(d) in.) in all instances. The defect response was located in the intervals (0.1s ≤ t ≤ 0.3s, 0.7s ≤ t ≤ 0.9s) in all cases. Noise was estimated utilizing the time interval between the two defects ($0.3 < t \leq 0.6\ s.$).

4.3 DS3 Dataset

After the initial analysis of the SoG features obtained from DS1 and DS2, the calibration record sources for DS1were expanded in number in an effort to capture greater possible morphologies that may be present in the defect responses and to further verify the robustness of the proposed methods. In addition, for each line scan, the estimated noise record was expanded

to 1000 datapoints and located immediately prior to the ROI to better investigate the Signal-to-Noise (SNR) of the estimated noise, the actual signal, and the SoG representations.

DS1 and DS2 were utilized to study the initial effectiveness of the SoG features in approximating the defect response. The DS3 dataset was utilized primarily in the study of symbolic representation of defect responses via SoG features.

CHAPTER V

FEATURE DETECTION AND EXTRACTION ALGORITHM

5.1 SoG Feature Detection and Extraction (SoGFDE) Outline

A diagram of the SoGFDE algorithm [246] is provided in Figure. 5.1 with a detailed description of the algorithm stages following.

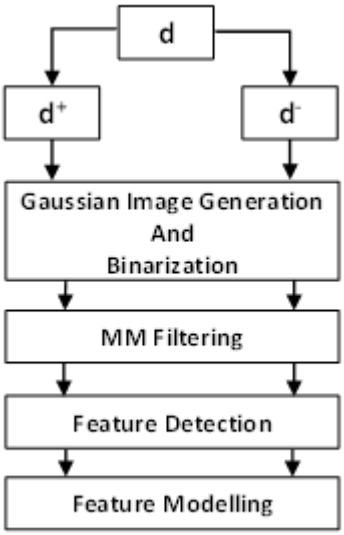

Figure 5.1 SoGFDE Process Diagram.

Referencing the block diagram, the input defect response vector d, is separated into positive and negative portions. The resulting vectors are then subject to further feature detection and extraction operations independently until the Feature Modeling step.

5.2 Gaussian Image Generation and Binarization

Table 5.1 provides pseudocode for the Gaussian image generation and binarization process.

Table 5.1 Gaussian Image Generation and Binarization Algorithm

Algorithm: *BinarizeDefectResponse*	
Input: $Sampled\ defect\ response\ vector$: $\mathbf{d} = [d_1, d_1, \dots, d_n]^{\boldsymbol{T}}$ $Sampling\ instant\ vector$: $\mathbf{t}_{\boldsymbol{s}} = [t_1 = 0, t_2, \dots, t_n]^{\boldsymbol{T}}$ $Expected\ Peak\ Width$: σ_e $Binary\ Image\ Threshold$: α	
Output: $Binary\ Image\ Matrices$: $\mathbf{B}^+, \mathbf{B}^-$	
Step	**Description**
1.	Partition s such that $$\mathbf{d} = \mathbf{d}^+ - \mathbf{d}^-$$ Where $$d_i^+ = \begin{cases} d_i, & d_i > 0 \\ 0, & otherwise \end{cases}$$ $$d_i^- = \begin{cases} \lvert d_i \rvert, & d_i < 0 \\ 0, & otherwise \end{cases}$$ $$1 \le i \le n, \qquad n \in \mathbb{Z}$$
2.	Find the maximum values in each partitioned signal: $$d_{max}^+ = \max(\mathbf{d}^+), \qquad d_{max}^- = \max(\mathbf{d}^-)$$
3.	Normalize the partitioned signals $$\mathbf{d}_n^+ = \frac{\mathbf{d}^+}{d_{max}^+}, \qquad \mathbf{d}_n^- = \frac{\mathbf{d}^-}{d_{max}^-}$$
4.	For each partitioned signal vector, form a Gaussian Image Matrix (e.g., for positive part) $$\mathbf{g}_i^+ = d_i^+ \exp\left(-\frac{(\mathbf{t_s} - t_\mathrm{i})^2}{\sigma_e^2}\right), \ 1 \le i \le n$$ $$\mathbf{G}^+ = [\mathbf{g}_1^+ \quad \dots \quad \mathbf{g}_n^+]$$
5.	Create the partitioned vector Binary Image Matrices such that $$\mathbf{B}^+(i,j) = \begin{cases} 1, & \mathbf{G}^+(i,j) \ \ge \alpha \\ 0 & otherwise \end{cases}$$ $$\mathbf{B}^-(i,j) = \begin{cases} 1, & \mathbf{G}^-(i,j) \ \ge \alpha \\ 0 & otherwise \end{cases}$$

As indicated in Table 5.1, the original sampled defect response signal is partitioned into positive and negatives values (step 1) with each partitioned signal normalized onto the interval [0,1] (steps 2,3).

Next, for each partitioned signal, a 2-D signal image (dimension n x n) is created by using the spatial/temporal location in the ROI and normalized amplitude of each signal data point as the mean and amplitude of a Gaussian function of prespecified standard deviation (σ). The fitted functions are arranged in columnar format (step 4). With this arrangement, the original signal values are located along the main diagonal of the constructed signal image but stretched in time. Selection of the known standard deviation is not critical, however, if the value is too large it will increase the number of calculations necessary for the MM filtering portion of the algorithm and increase the number of sample points considered for analysis in the neighborhood of each d_i value.

Lastly, a thresholding operation is performed on the normalized Gaussian signal image such that values above a pre-specified binary image threshold (α**)** referenced to the maximum amplitude value in the window, are set to unity, and values below the threshold value set to zero. The process creates a simplified binary image of the 1-D signal in 2-D which can be viewed as indicative of a top-down view of the original signal. Selection of the binary image threshold in 1-D can be interpreted as related to the SNR measure. In terms of the binary image, it reveals the neighborhood data points around the peak in the Field of View (FoV) by the algorithm.

5.2.1 Selection of Expected Peak Width

Selection of σ_e, should reflect knowledge of the ECI configuration. As stated earlier for EC line scans, the probe is scanned over the ROI and due to the differential nature of the probe coils and the speed of the scanning procedure, the coil closest to the defect will detect the defect

presence before the trailing coil. This knowledge directly affects the peak width of the defect response [247]. Therefore, for defects that are small compared to the coil diameter, σ_e was calculated as:

Let $d_c = probe\ coil\ diameter\ (in.)$ and $v_s = scan\ rate\ (\ ^{in.}/_{s.})$

$$\sigma_e = \frac{0.5 d_c}{v_s} \tag{5.1}$$

Notwithstanding, the algorithm presented is general enough in nature that σ_e may be selected based upon other analysis methods.

5.2.2 Selection Methods for Binary Image Threshold

The value of α is selected to determine the neighborhood size around a detected peak or equivalently the number of data points to be considered in the detection and feature extraction procedure. If the value is too small, unwanted noise will be included in the binary Gaussian image. Conversely, if the value is too large, useful portions of the peak neighborhood are excluded from analysis. This study investigated two methods for the calculation of α. The first determined the parameter by considering a dataset of line scans to determine a global value for the parameter. By contrast, another method was employed that calculated α by only considering an individual line scan to determine a local value for the parameter. Descriptions of the methods employed follow.

5.2.2.1 Global Method

Initial analysis of the performance of the SoGFDE algorithm (for DS1 and DS2) employed a global scheme to determine the value for α. The method utilizes the fact that the datasets in the study have defects that occur in known regions (ref. Chapter 4). Stated formally, a matrix $\mathbf{D}$ was defined for a dataset $\mathfrak{D}$ such that each row $\mathbf{d}_i$of $\mathbf{D}$ contains the absolute values of the line scan record:

$$[\mathbf{D}]_i = |\mathbf{d}_i|, \forall\, \mathbf{d}_i \in \mathfrak{D}$$

Next, submatrices are extracted such that,

$$\mathbf{D}_{i,D} = [\mathbf{D}]_{i,defect\_region}, \qquad \mathbf{D}_{i,N} = [\mathbf{D}]_{i,noise\_region}$$

Defining the operator: $\overline{\mathbf{D}}$ as the mean of the elements of the matrix $\mathbf{D}$, then

$$\alpha = \frac{\overline{\mathbf{D}_N}}{\overline{\mathbf{D}_D}} \tag{5.2}$$

5.2.2.2 Local Method

In the analysis of DS3, the method to determine alpha in equation 5.2 was reformulated to provide the estimate of α by considering the number of data points to be used in the estimate. This approach provided the mechanism to allow a range of α values to be investigated that can adapt per each line scan. Details of the methods employed are provided in the algorithm listed in Table 5.2.

Table 5.2 Local Estimation of Binary Image Threshold

Algorithm: *EstimateAlpha*	
Input: $Sampled\ defect\ response\ vector$: $\mathbf{d} = [d_1, d_1, \dots, d_n]^{\boldsymbol{T}}$ $Number\ of\ sample\ points\ for\ \alpha\ estimate$: m $Histogram\ bin\ width$: γ	
Output: $Binary\ Image\ Threshold$: α	
Step	**Description**
1.	Partition s such that $$\mathbf{d} = \mathbf{d}^+ - \mathbf{d}^-$$ Where $$d_i^+ = \begin{cases} d_i, & d_i > 0 \\ 0, & otherwise \end{cases}$$ $$d_i^- = \begin{cases} \lvert d_i \rvert, & d_i < 0 \\ 0, & otherwise \end{cases}$$ $$1 \le i \le n, \qquad n \in \mathbb{Z}$$
2.	Find the maximum values in each partitioned signal: $$d_{max}^+ = \max(\mathbf{d}^+), \qquad d_{max}^- = \max(\mathbf{d}^-)$$
3.	Normalize the partitioned signals $$\mathbf{d}_n^+ = \frac{\mathbf{d}^+}{d_{max}^+}, \qquad \mathbf{d}_n^- = \frac{\mathbf{d}^-}{d_{max}^-}$$
4.	Concatenate the normalized partitioned signals $$\mathbf{d}_n = [\mathbf{d}_n^+ \quad \vert \quad \mathbf{d}_n^-]$$
5.	$\mathbf{b} = \{1, \dots, 3\gamma, 2\gamma, \gamma\}$, $0 \le \gamma \le 1$
6.	$\mathbf{h} = Histogram(\mathbf{d}_n, \mathbf{b})$
7.	$\mathbf{c}_h = CumulativeSum(\mathbf{h})$
8.	$i_{min} = FindMinIndex(\mathbf{c}_h, m)$
9.	$\alpha = \mathbf{b}[i_{min}]$

Table 5.2 describes an algorithm which utilizes the number of sample points to include in the estimate as an input parameter. The sampled input response signal is firstly normalized onto the interval [0,1] separately for the positive and negative portions to preserve the zero mean aspect of the input signal. Next, a histogram is constructed over the α values investigated. The histogram bin values are supplied in reverse order so the largest amplitude values in the input signal are at the front of the histogram counts vector $\mathbf{h}$ (steps 5,6). Arrangement of the histogram counts in this manner permits the cumulative sum of the histogram counts (step 7) to

be constructed such that the appropriate alpha value can be obtained via a left right search of the cumulative sum vector (step 8,9).

5.3 MM Filtering

Once the binary signal images are created, the images are subjected to the binary erosion and dilation MM operators using a structural element that consists of a binarized Gaussian signal image of smaller width than the original signal. The pseudocode for the filtering operation is provided in Table 5.3.

Table 5.3 MM Filtering Algorithm

Algorithm:*DenoiseImages*	
Input: $Sampling\ instant\ vector$: $\mathbf{t_s} = [t_1 = 0, t_2, \dots, t_n]^T$ $Binary\ Gaussian\ Image\ Matrix$: $\mathbf{B}_{nxn}$ $Expected\ Peak\ Width$: σ_e $Structuring\ Element\ Width\ Delta$: Δ $SE\ Binary\ Image\ Threshold$: β	
Output: $Denoised\ Defect\ Response\ Binary\ Images$: $\mathbf{B}_d^+, \mathbf{B}_d^-$	
Step	**Description**
1	Define Structuring Element (SE) width $\sigma_{SE} = \sigma_e - \Delta$
2	Form SE matrix from known Gaussian signal $\mathbf{f}_i = \exp\left(-\frac{\left(\mathbf{t_s} - t_{i,\frac{n-1}{2}}\right)^2}{\sigma_{SE}^2}\right),$ $for\ 1 \le i \le n$ $\mathbf{F} = [\mathbf{f}_1 \quad \dots \quad \mathbf{f}_n]$

Table 5.3 (continued)

Step	Description
3	Create the associated Binary SE matrix and obtain submatrix containing the SE as the minimum bounding rectangle (MBR). $$\mathbf{B}_{SE}(i,j) = \begin{cases} 1, & \mathbf{F}(i,j) \geq \beta \\ 0 & otheriwise \end{cases}$$ $$\mathbf{SE} = MBR(\mathbf{B}_{SE})$$
4	Perform the MM open "∘" (erode "⊖ " and dilation "⊕ ") operation on the signal Binary Gaussian Image Matrices: $$\mathbf{B}_d^+ = \mathbf{B}_{SE} \circ \mathbf{B}^+ = (\mathbf{B}_{SE} \ominus \mathbf{B}^+) \oplus \mathbf{B}^+$$ $$\mathbf{B}_d^- = \mathbf{B}_{SE} \circ \mathbf{B}^- = (\mathbf{B}_{SE} \ominus \mathbf{B}^-) \oplus \mathbf{B}^-$$

Referencing Table 5.3, a Gaussian shaped disc structuring element is created (steps 1-3) and utilized by the MM operations (step 4) to remove or reduce non-Gaussian-like peaks from the binary image or equivalently the ROI.

5.4 Initial Feature Detection

After the binary signal images are processed by the MM operations, a simplified variant of the K-means algorithm was applied to the resulting images to determine the location and number of the initial Gaussian peak centers. Table 5.4 provides pseudocode for the initial peak determination portion of the algorithm.

Table 5.4 Initial Peak Determination Algorithm

Algorithm: *FindInitialPeaks*	
Input: $Binary\ Gaussian\ Image\ Matrix(filtered)$: $\mathbf{B}_{nxn}$	
Output: $Candidate\ Cluster\ Centers$: $\mathbf{p}_{j,\min}$ $Candidate\ Cluster\ Centers$: $region\_locs$	
Step	**Description**
1.	Find the indices of the columns in **B** where change of state occurs and count and identify the possible peak regions $\mathbf{b} = diag(\mathbf{B})$

Table 5.4 (continued)

Step	Description
1.	$\mathbf{x} = abs\big(diff(\mathbf{b})\big)$ $\mathbf{i} = find\_indices(\mathbf{x} == 1)$ $where\ q = count\ of\ indicies\ in\ \mathbf{i}$ $i_1 = 1, i_{q+1} = n$ $\mathbf{i}\ is\ a\ vector\ of\ dimension\ (q+2,1)$ $[num\_regions, region\_locs] = CountPeakRegions(\mathbf{b}, \mathbf{i})$
2.	For each of the possible cluster regions in the image $\mathbf{B}$, find the cluster center. Let *m* represent the number of column indices in the jth cluster. Define the candidate cluster centers along the main diagonal of the region: $\mathbf{p}_l = (l, l),\ where\ i_{j(1)} \leq l \leq i_{j(m)}, l \in \mathbb{Z}$ let $\big[\mathbf{r}_j, \mathbf{c}_j\big] = find(\mathbf{B}\big(:, i_{j(1)}: i_{j(m)}\big) == 1)$ Represent the indices of the active pixels in cluster j. Calculate the sum of the Euclidean distances for each active pixel to each candidate cluster center $$\mathbf{d}_l = \sum_{k=1}^{m} \sqrt{(r_k - l)^2 + (c_k - l)^2}$$
3.	Obtain the initial cluster center for the jth region as the index of the minimum of the summed distances vector $\mathbf{d}_l$ ($\mathbf{p}_{j,\min}$) in step 2 and the region location extents $region\_locs$.

Referencing the pseudocode listing in Table 5.4, if detected peaks are present in the input filtered binary Gaussian image matrix, they will be located along the main diagonal of the image. Using this information, step 1 in the listing locates the state transitions along the main diagonal of the filtered binary Gaussian image matrix. This information is used to locate the regions in the image that contain detected Gaussian peaks.

Step 2, utilizes the indices of the detected regions that correspond to the clusters identified in step 1 and then calculates the Euclidean distance to each possible cluster center. The initial guess at the cluster centers are the indices along the main diagonal for a given region.

Lastly, in step 3 for a given cluster region, the columnar index along the main diagonal that has the minimum summed Euclidean distance is selected as the initial guess for the peak center.

In early testing of the Initial Feature Determination Algorithm the K-Means algorithm was investigated and misclassification of cluster centers occurred frequently. As a result, the presented algorithm was developed that is much like K-means but is simplified in the fact it utilizes known features of the construction of the filtered binary Gaussian image matrix to eliminate cluster misclassification errors.

By partitioning the original signal into positive and negative portions, adequate separation in the point clusters is obtained that greatly reduces cluster misclassification (and consequent inaccurate peak center calculations).

The initial peak centers are used as an initial guess for the Gaussian μ parameter for a given peak and the region boundary vector **i** as identified in Table 5.4, was used to determine the width of the cluster which is representative of peak width or standard deviation parameter σ.

The results of application of the simplified variant of the K-Means algorithm are a set of cluster centers (spatial or temporal locations) and widths that along with the associated amplitude values will comprise the initial means, standard deviations, and amplitudes for the signal fitting/feature modelling portion of the algorithm.

5.5 Feature Modelling

After obtaining the initial estimated SoG parameters from the Binary Gaussian Images, the nonlinear constrained optimization [248,249] algorithm *'fmincon'* in MATLAB was used in a two-phase process to determine the estimated optimal model of the SoG approximation parameters to the original signal.

During the first phase, each SoG parameter feature set was independently modelled to the respective portion of the original partitioned signal using the cluster centers and region width information obtained by the initial feature detection algorithm as constraints for the μ and σ parameters. Amplitude constraints were constructed by using the extrema values of the original defect response within a given cluster region.

The second phase estimation process used the fitted SoG parameter features from the first phase and fitted the entire SoG parameter feature set to the original signal. Both optimization phases used the Summed Squared Error (SSE) metric as the objective function. The second phase optimization can be stated mathematically as follows:

Assuming the SoGFDE algorithm detected p peaks:

Given:

$Peak\ means$: $\boldsymbol{\mu} = \left[\mu_1, \mu_2, \dots, \mu_p\right]^T$

$Peak\ widths$: $\boldsymbol{\sigma} = \left[\sigma_1, \sigma_2, \dots, \sigma_p\right]^T$

$Peak\ Amplitudes$: $\mathbf{a} = \left[a_1 = d(\mu_1), a_2, \dots, a_p\right]^T$

$Orignal\ signal\ vector$: $\mathbf{d} = [d_1, \dots, d_n]^T$

$Sampling\ instant\ vector$: $\mathbf{t_s} = [t_1 = 0, t_2, \dots, t_n]^T$

The SoG response is calculated as:

$$\mathbf{f}_{est} = \sum_{i=1}^{p} a_i \exp\left(-\frac{(\mathbf{t_s} - \mu_i)^2}{\sigma_i^2}\right) \tag{5.3}$$

The objective function used to optimize each of the Gaussian mixtures is then:

$$SSE = \sum_{i=1}^{n} (\mathbf{d} - \mathbf{f}_{est})^2 \, , for\ 1 \leq i \leq n \tag{5.4}$$

5.6 Residual SoGFDE

For some defect responses, the initial pass of the SoGFDE algorithm misses content and requires a second pass on the residual signal. An example of the phenomenon from the DS3 dataset is provided in Figure 5.2.

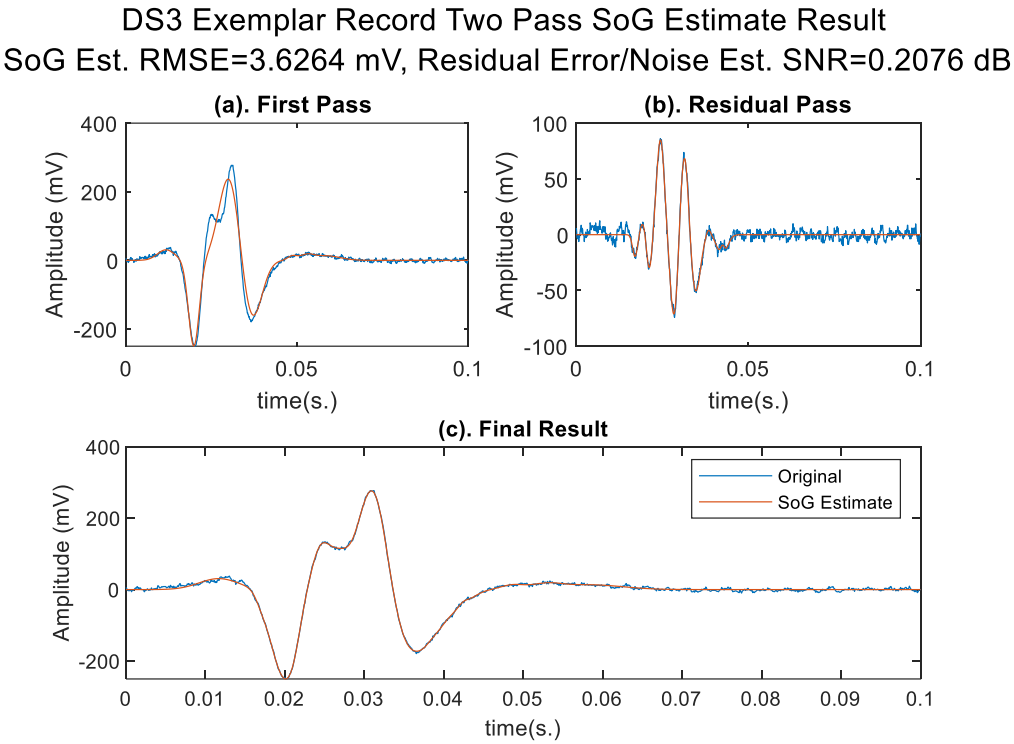

Figure 5.2 Two-Pass SoG Feature Extraction Example

From the top left (a) results of the initial pass of the extraction algorithm does not capture the peak between the minimum and maximum response, (b) SoG feature extraction on the residual defect response signal, (c) the final defect response (RMSE =3.6264 mV and residual error vs. estimated noise SNR= 0.2076 dB).

To investigate the behavior of the SoGFDE algorithm parameters for the defect responses in DS3, an iterative search method was employed to determine the optimal alpha threshold parameter for each defect response in terms of minimal RMSE when compared to the original response. Pseudocode for the approach is provided in Table 5.5.

Table 5.5 SoGFDE Minimum RMSE Search Algorithm.

Algorithm: *TwoPassSoGFeatureExtraction*	
Input: $Sampled\ defect\ response\ vector$: $\mathbf{d} = [d_1, d_2, \dots, d_n]^{\boldsymbol{T}}$ $Sampling\ instant\ vector$: $\mathbf{t_s} = [t_1 = 0, t_2, \dots, t_n]^T$ $Vector\ of\ sample\ points\ range\ for\ \alpha\ estimate$: $\mathbf{m} = [m_1, m_2, \dots, m_k]^T$ $Expected\ Peak\ Width$: σ_e $Structuring\ Element\ Width\ Delta$: Δ $Binary\ Image\ Threshold$: α $SE\ Binary\ Image\ Threshold$: β	
Output: $Initial\ and\ Final\ SoG\ estimate\ information$: $Columnwise\ matrix\ of\ fitted\ SoG\ Parameters\ (A, \mu, \sigma)$: $\mathbf{P}_{\min(\mathbf{3xp})}$ $SoG\ Estimate\ of\ defect\ response$: $\mathbf{f} = [f_1, f_2, \dots, f_n]^{\boldsymbol{T}}$ $Binary\ Image\ Threshold\ (resulting\ in\ minimal\ RMSE)$: α_{min}	
1.	Foreach (**m**) {
2.	$\alpha = EstimateAlpha(\mathbf{d}, m_i)$
3.	$\mathbf{P}_{initial}(\mathrm{i}) = ExtractSoGFeatures(\mathbf{d}, \mathbf{t_s}, \alpha, \beta, \Delta, \sigma_e)$
4.	$\mathbf{f}_{initial}(\mathrm{i}) = GenSoGCurve(\mathbf{t_s}, \mathbf{P}_{initial})$
5.	$error_{init}(i) = Rmse(\mathbf{d}, \mathbf{f}_{initial})$ }
6.	$\min(error_{init}) \rightarrow \mathbf{P}_i, \mathbf{f}_i, \alpha_i$
7.	Foreach (**m**) **{**
8.	$\mathbf{r} = \mathbf{d} - \mathbf{f}_i$
9.	$\alpha = EstimateAlpha(\mathbf{r}, m_f)$
10.	$\mathbf{P}_{residual}(\mathrm{i}) = ExtractSoGFeatures(\mathbf{r}, \mathbf{t_s}, \alpha, \beta, \Delta, \sigma_e)$
11.	$\mathbf{P}_{final}(\mathrm{i}) = MergeSoGParams(\mathbf{P}_i, \mathbf{P}_{residual}(\mathrm{i}))$
12.	$\mathbf{f}_{\mathrm{final}}(\mathrm{i}) = GenSoGCurve\left(\mathbf{t_s}, \mathbf{P}_{final}(\mathrm{i})\right)$
13.	$error_{final}(i) = Rmse(\mathbf{d}, \mathbf{f}_{final})$ }
14.	$\min(error_{final}) \rightarrow \mathbf{P}_f, \mathbf{f}_f, \alpha_f$

Referencing Table 5.5, α is estimated using the Local Method described in section 5.2.3.2 (steps 2 and 9). Steps 1 through 5 iterate using each α value calculated from the supplied defect response and number of data points considered (m) approximating the defect response

with the SoGFDE algorithm. At the end of the initial pass the α value and associated SoG parameters and estimated response resulting in minimal RMSE when compared to the original defect response are determined (step 6). The aforementioned process is repeated again (steps 7 through 14) on the defect response residual determined as indicated in step 8.

It is noted that this estimating procedure is made possible by preserving the zero mean aspect of the supplied defect response and the additive nature of the SoG representation.

5.7 Analysis Methods

The analysis methods employed in the study of DS1 and DS2 were selected to demonstrate the SoGFDE method performance for approximating the entirety of the response and the response extrema. In addition, an implementation of the Radial Basis Function Neural Network (RBFNN) from MATLAB via the command '*newrb*' was used to compare the SoGFDE based estimates to a similar established method. Descriptions of the analysis metrics and methods follow.

5.7.1 SoG Approximation Analysis Methods

Definitions of the analysis metrics employed in the study of the datasets in this study are provided in Table 5.6.

Table 5.6 SoGFDE Approximation Analysis Metrics

Metric	Formula
Maximum Amplitude Δ	$max(\mathbf{d}_{\text{defect}}) - max(\mathbf{f}_{\text{defect}})$
Minimum Amplitude Δ	$min(\mathbf{d}_{\text{defect}}) - min(\mathbf{f}_{\text{defect}})$
Defect Response RMSE (l samples)	$\sqrt{\frac{\sum_{i=1}^{l}\left(\mathbf{d}_{\boldsymbol{defect}} - \mathbf{f}_{defect}\right)^2}{l}}$

Table 5.6 (continued)

Metric	Formula
Estimated Noise RMS (m samples)	$\sqrt{\frac{\sum_{i=1}^{m}(\mathbf{d}_{noise})^2}{m}}$
SoG Approximation RMSE (n samples)	$\sqrt{\frac{\sum_{i=1}^{n}(\mathbf{d}-\mathbf{f})^2}{n}}$
SoG Residual to Noise SNR (n samples)	$20log\left(\sqrt{\frac{\sum_{i=1}^{n}(\mathbf{d}-\mathbf{f})^2}{\sum_{i=1}^{n}\mathbf{n}^2}}\right)$

Defect Response RMSE and Estimated Noise RMS analysis metrics are taken over the subintervals $\mathbf{d}_{defect}, \mathbf{d}_{noise}$ (see Chapter 4) from the original signal and the SoG approximation ($\mathbf{f}$). The noise estimate record is identified as $\mathbf{n}$.

5.7.2 SoG Representation Comparison to RBFNN

The SoGFDE method proposed in this dissertation is similar in some aspects to previous approaches to the RBFNN [251] used for function approximation. However, many implementations of the RBFNN treat the RBF neuron sigma parameter as a constant for all neurons as this is a condition for satisfying the universal approximation property [252]. Other researchers have noted that the universal approximation property can have drawbacks in that the number of "building blocks" (in the present case Gaussian functions) can be unbounded to attain the desired accuracy [253]; a property which can introduce interpretability issues. To demonstrate the effectiveness of the SoGFDE algorithm and to highlight the differences in approximation of D-Coil defect responses, it was compared to the MATLAB implementation of RBFNN ('*newrb*'). To aid in the discussion of the comparison results a brief discussion of the relevant implementation details for the RBFNN follow.

The MATLAB RBFNN implementation creates RBF neurons centered at each sampling instant of constant spread (σ) that span the entire of the ROI. The RBFNN is a two-layer

network consisting of a hidden layer of RBF neurons along with associated weights and bias and connected to a purelin layer that provides the sum of the RBF contributions to the approximation. At each iteration of the approximation process, the RBF neuron with the largest error is selected and the associated weights and bias are adjusted to minimize the Mean Square Error (MSE). The maximum number of RBF neurons is specified as input to the function. The design of the RBFNN for function approximation can be stated mathematically as follows:

Let $\mathbf{q}[\mathbf{t}], \mathbf{t} = [t_1 = 0, t_2, \dots, t_n]^{\boldsymbol{T}}$ define an approximation to a supplied function $\mathbf{d}[\mathbf{t}]$.

The approximation can then be written as the linear summation of a collection of weighted kernel functions:

$$\mathbf{q}[\mathbf{t}] = \sum_{i=1}^{M} w_i K\left(\frac{\mathbf{t} - z_i}{s_i}\right) = \sum_{i=1}^{M} w_i \mathbf{q}_{K,i} \tag{5.5}$$

In the present case, the kernel functions are a linear collection of Gaussian functions:

$$\mathbf{q}[\mathbf{t}] = \sum_{i=1}^{M} A_i exp\left(\frac{(\mathbf{t} - \mu_i)^2}{\sigma_i^2}\right) \tag{5.6}$$

Referencing Equation 5.6 in the case of Gaussian function kernels, there are three variables that can be adjusted for approximation: A_i, μ_i, σ_i.

The MATLAB implementation of the RBFNN for function approximation defines kernel nodes centers at each point of the input vector (μ_i), therefore referencing Equation 5.6, M=n. In addition, for each kernel node $\sigma_i = \sigma$. At each iteration, the kernel node with the largest MSE is identified and added to a collection of kernel functions that are subject to solution of a linear set

of equations from which the updated A_i is obtained in terms of weights and a bias term. Stated mathematically for the ith iteration, the set of identified kernel functions is:

$$\mathbf{Q}_{K,i} = \left[\mathbf{q}_{K\,\mathbf{1}}, \mathbf{q}_{K\,\mathbf{2}}, \dots, \mathbf{q}_{K\,\boldsymbol{i}}\right]^{\boldsymbol{T}}$$

From which the updated A_i values are calculated as

$$\mathbf{W}_{\mathrm{i}} = \begin{bmatrix} \mathbf{Q}_{K,i} \\ \mathbf{1} \end{bmatrix}$$

Where $\mathbf{1}$ a row vector of 1's of the same dimensions as $\left[\mathbf{q}_{K\,\boldsymbol{i}}\right]^{T}$

$$[\mathbf{a}, b]\mathbf{W}_i = \mathbf{d}$$

$$[\mathbf{a}, b]\mathbf{W}_i\mathbf{W}_i^{-1} = \mathbf{d}\mathbf{W}_i^{-1}$$

$$[\mathbf{a}, b] = \mathbf{d}\mathbf{W}_i^{-1} \tag{5.7}$$

From the estimate in Equation 5.7, the amplitude or weight for the pth RBF kernel node is then:

$$A_p = a_p + b, \qquad 1 \leq p \leq i \tag{5.8}$$

To further analyze the estimation performance of the SoGFDE algorithm, the aforementioned MATLAB RBFNN implementation was utilized for comparison of the approximated response to the original in terms of the defect response RMSE.

To ensure fair comparison, the RBFNN implementation was constrained in terms of the maximum number of neurons to the number of SoG elements found using the SoGFDE approximation method.

.

CHAPTER VI

SOGFDE APPROXIMATION RESULTS

This chapter investigates the estimation performance of the SoGFDE algorithm visually and in terms of the analysis methods discussed in section 5.7. In addition, the dual (residual) pass SoGFDE approximation is investigated and the resulting RMSE compared to the original response and estimated noise records. Lastly, the SoGFDE method is compared to a similar common implementation RBFNN used in function approximation.

6.1 SoGFDE Initial Pass Results

The following subsections in this section present the results from only an initial pass of the SoGFDE algorithm over the line scan records in DS1 and DS2. However, prior to presenting these results a visual analysis of the algorithm is conducted for a line scan from the DS2 dataset.

6.1.1 Visual Analysis of SoGFDE Algorithm

Figures 6.1 through 6.3 provide an example of the results obtained from the SoGFDE algorithm for a record from the DS2 data set.

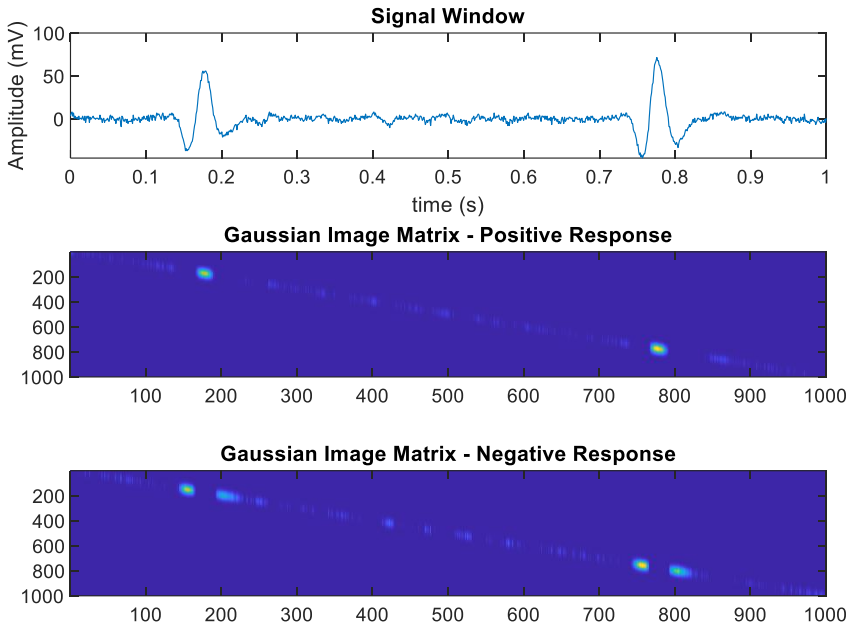

Figure 6.1 Example Gaussian Image Matrix (scaled color)

Referencing Figure 6.1, the top plot and bottom images show two EDM defect responses present in the ROI from DS2. The Gaussian image matrices are shown as scaled color images for the $\mathbf{d}^{+}$ and $\mathbf{d}^{-}$partitioned exemplar signal. As indicated in the Gaussian images, defect responses lie along the main diagonal and dilated in time. Noise largely appears as vertical lines with little lateral (horizontal) extent in the images. The peaks of the two defect responses are clearly visible.

Next, the images in Figure 6.1 were subject to the binarization process described in Table 5.1.

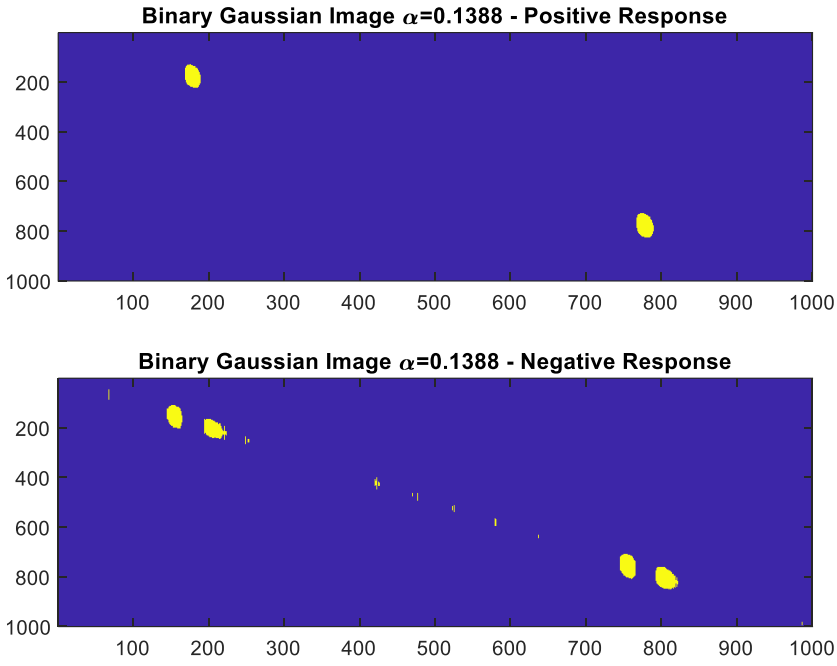

Figure 6.2 Binary Gaussian Image of Exemplar Signal

Referencing Figure 6.2, the binarization process removes much of the undesired noise in the defect response. In addition, processing the partitioned signals separately provides greater separation of the SoG features. Next, the binarized images in Figure 6.2 were subject to MM filtering and the results are indicated in Figure 6.3

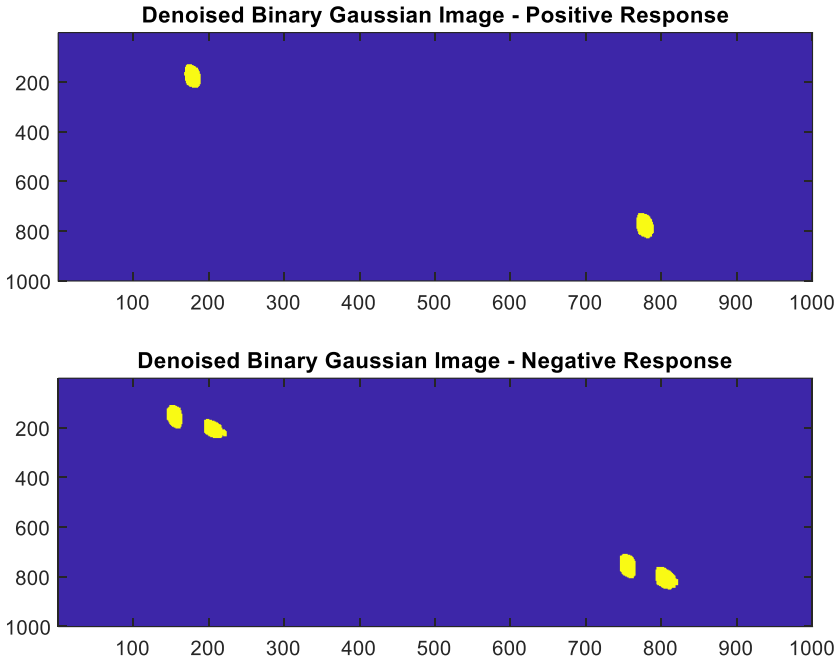

Figure 6.3 MM Filtered Exemplar Signal

As indicated in Figure 6.3, the MM filtering clearly isolates the SoG features in the defect response. The SE used to denoise the exemplar signal shown in Figure 6.3 is provided in Figure 6.4.

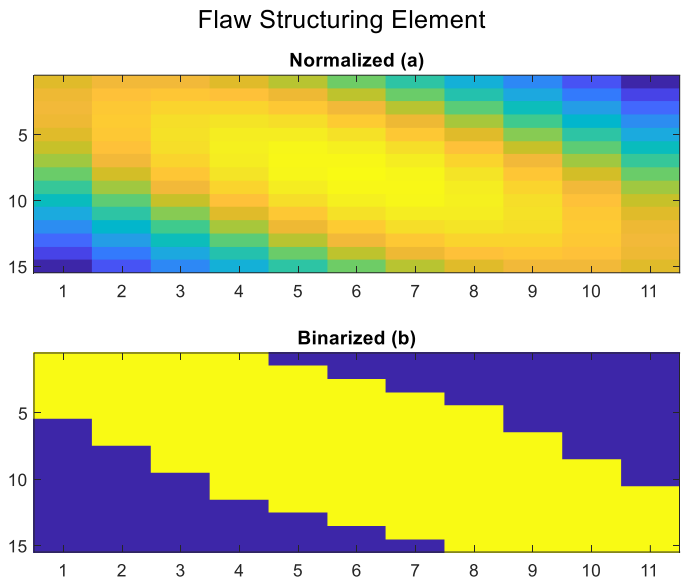

Figure 6.4 SoGFDE MM Filtering Gaussian Structuring Element.

Top image (a) is of the normalized Gaussian structuring element. Image (b) is the structuring element after binarization.

The images in Figure 6.3 were then used as input to the Initial Feature Detection and Modelling stages of the algorithm. Figure 6.5 presents the approximation results compared to the original response in terms of the Defect Response RMSE measure.

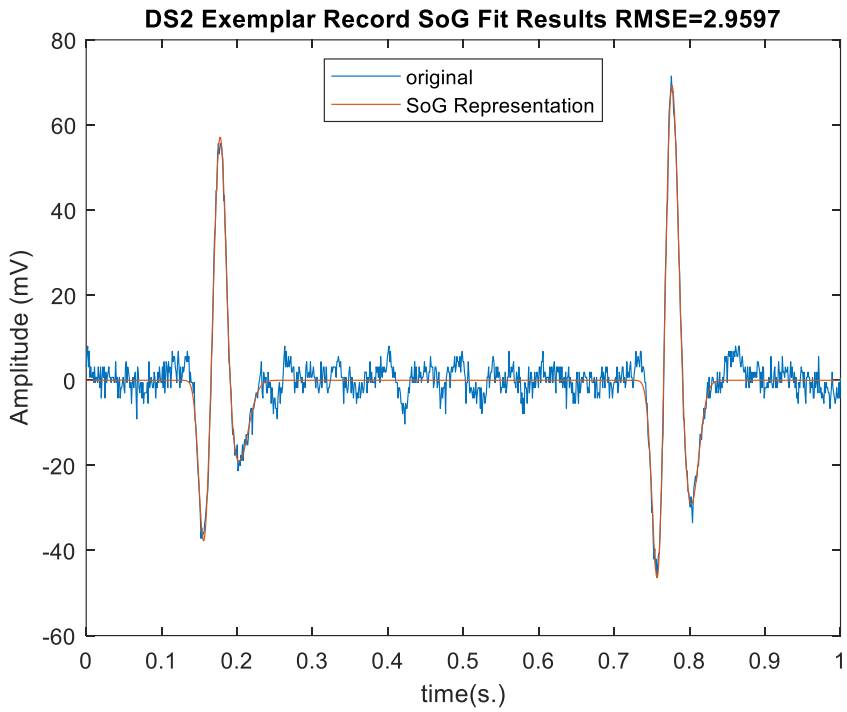

Figure 6.5 SoGFDE Approximation Results for DS2 Exemplar Signal

As indicated Figure 6.5 the SoG approximation is in close agreement with the original defect response with an RMSE=2.9597 mV which is lower than the estimated noise region RMS=10.6643 mV by a factor of 3.6.

6.1.2 Algorithm Parameters for DS1 and DS2

Utilizing the parameter estimation procedures described in Sections 5.2.2 and 5.2.3.1 the SoGFDE algorithm parameters were calculated for DS1 and DS2 and are listed in Table 6.1.

Table 6.1 Algorithm Parameters Used for Analysis of DS1 and DS2

Parameter	DS1 Value	DS2 Value
α	0.0672	0.1388
σ_e	0.004	0.024
Δ	0.002	0.012
β	0.9	0.9

Analysis of the DS1 and DS2 datasets using the SoG approximation analysis methods follow.

6.1.3 DS1 Results

Figures 6.6 through 6.8 show results of the SoGFDE algorithm approximation results for the records in DS1.

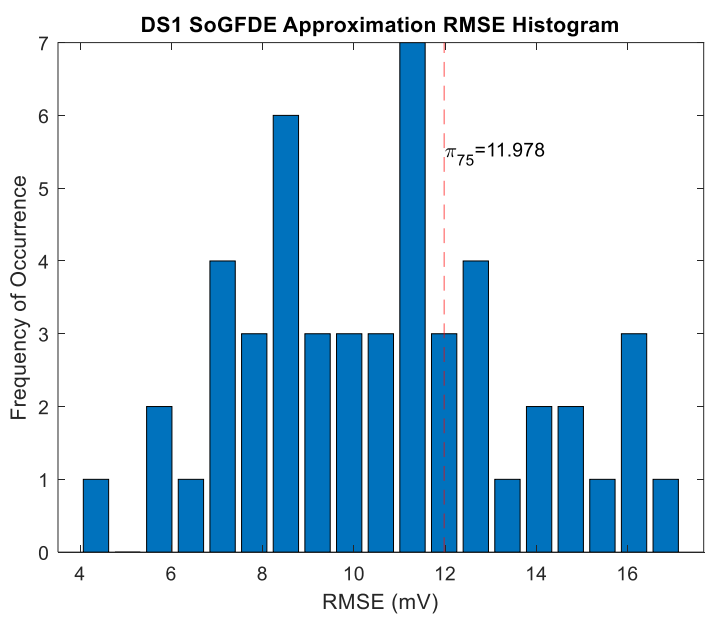

Figure 6.6 DS1 SoG Approximation RMSE Histogram.

The red dashed vertical line in the plot denotes the 75th percentile value for the RMSE histogram

As shown in Figure 6.6, 75% of the records had a RMSE less than 11.978 mV. Figures 6.7 and 6.8 show the minimum and maximum RMSE cases for DS1.

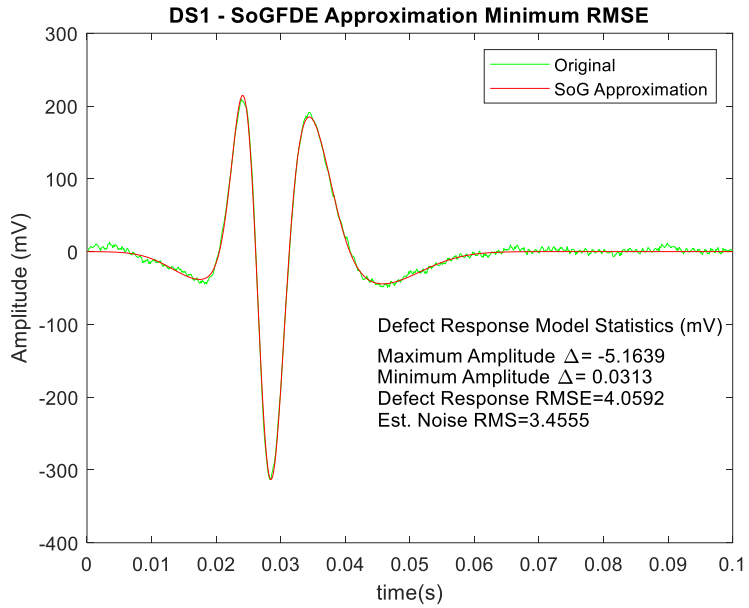

Figure 6.7 DS1 SoG Approximation RMSE Minimum Case.

As shown in Figure 6.7, the algorithm detected all five features in the defect response RMSE differs from the estimated noise RMS by 0.6037 mV.

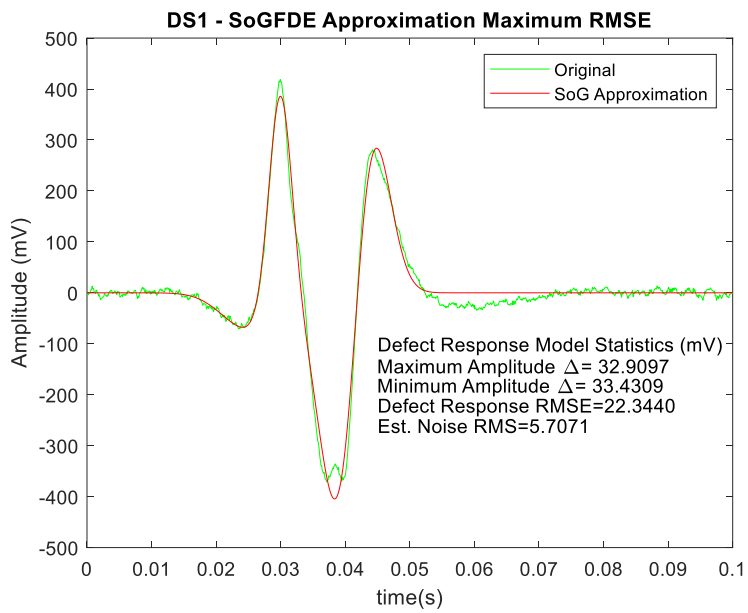

Figure 6.8 DS1 SoG Approximation RMSE Maximum Case.

Referencing Figure 6.8, The algorithm detected four defect features. However, there are possible discrepancies in the response maximum and minimum peaks that simple peak analysis algorithms may not detect (note interval $0.025 \leq t \leq 0.045$). The noted discrepancies however, are detectable by minimum and maximum amplitude Δ metrics when compared to the results of Figure 6.6. In addition, there is a much larger difference between the Defect Response RMSE when compared to the Estimated Noise RMS (22.3440 mV-5.7071 mV=16.6369 mV) providing further indication of possible anomalies in the defect response.

6.1.4 DS2 Results

Figures 6.9 through 6.11 show the SoGFDE algorithm approximation results for the records in DS2.

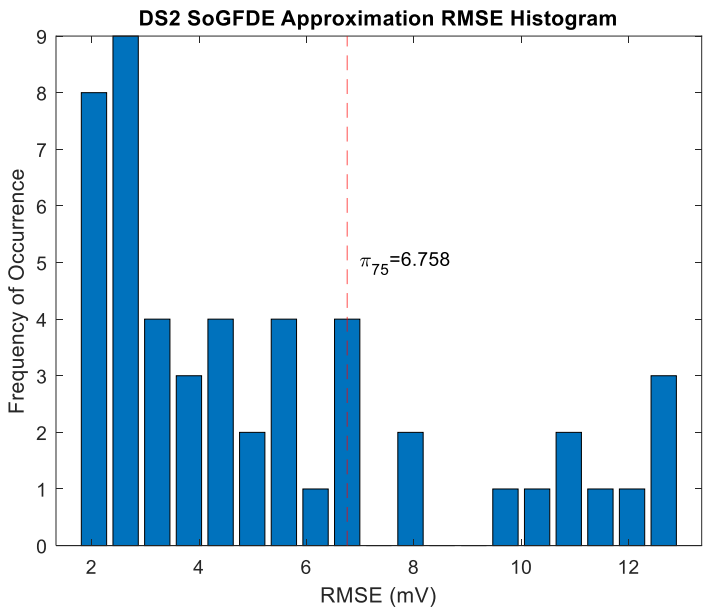

Figure 6.9 DS2 SoG Approximation RMSE Histogram.

The red dashed vertical line in the plot denotes the 75th percentile value for the RMSE histogram.

Referencing Figure 6.9, the SoG approximation RMSE for records in DS2 is noticeably lower than that for DS1 as indicated by the lower 75th percentile value. This result indicates that the records in DS2 are more Gaussian-like in appearance than the records in DS1. Similar to the results presented for DS1, Figures 6.10 and 6.11 show the minimum and maximum RMSE cases for DS2.

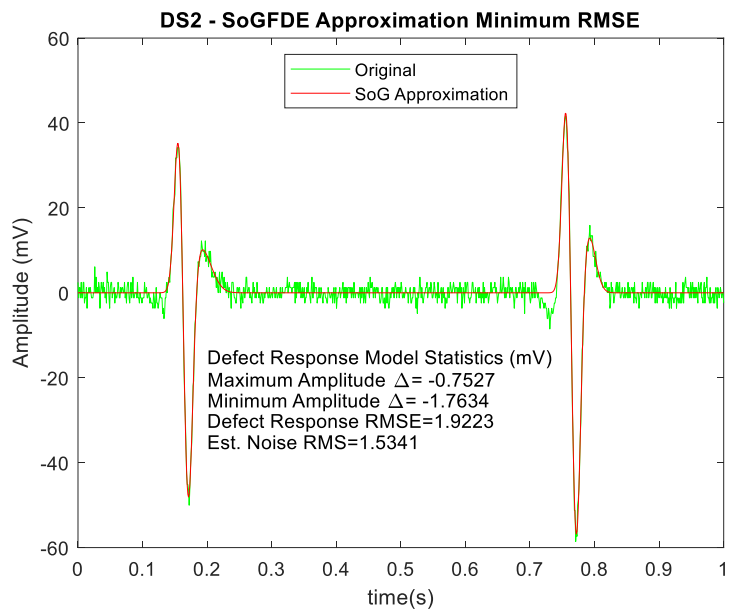

Figure 6.10 DS2 SoG Approximation RMSE Minimum Case.

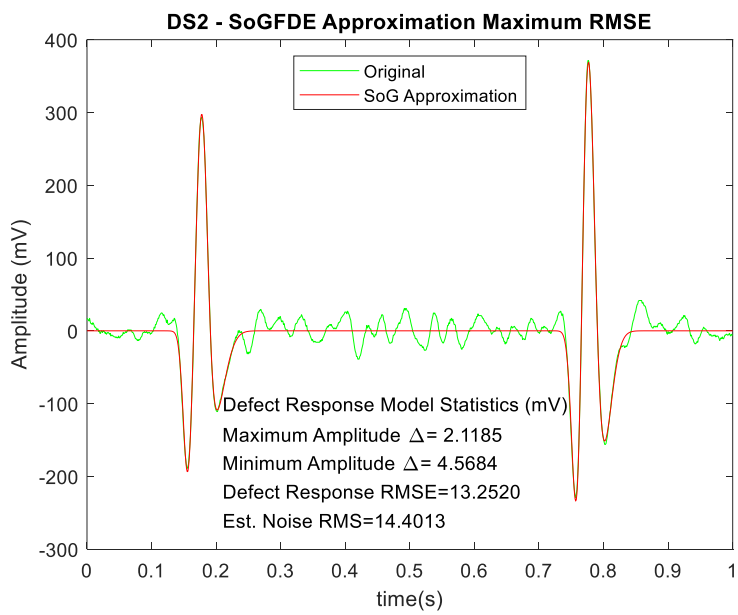

Figure 6.11 DS2 SoG Approximation RMSE Maximum Case.

Figures 6.10 and 6.11 indicate an inversion in the probe response signature for the two EDM notches in the ROI that could be easily detected by comparing the SoG representation A and μ parameters between the two feature sets. In addition, Figure 6.11 indicates larger Defect Response RMSE and Estimated Noise RMS when compared to Figure 6.10. This information coupled with the difference in extrema peak Δ's indicates a difference in the noise magnitude between the two responses and provides quantifiable information regarding the difference. However, in the case of Figure 6.11, the Defect Response RMSE is lower than the Estimated Noise RMS by 1.1493 mV.

6.1.5 Results Discussion for DS1 and DS2

Collectively, the results of sections 6.1.3 and 6.1.4 indicate that with very basic analysis metrics SoG approximation models can be used effectively to compare D-Coil defect response signals, uncover anomalies, and to gain a greater understanding of the datasets studied.

It is noted that the SoG approximation RMSE range for DS2 was approximately 1.77 times lower than that of DS1. This is an interesting result considering that DS2 contained two defect responses in the ROI compared to one in the DS1 ROI. This is also indicative that the SoG representation provides a better approximation for the Titanium defect records than the Inconel records. In addition, the results of Figures 6.10 and 6.11 provide quantitative evidence that the defect responses in DS2 are more Gaussian-like in their appearance; a fact that could possibly be used to construct more informed detection algorithms regarding D-Coil responses to defects in Titanium materials.

Lastly, as indicated in Figures 6.8, 6.10, and 6.11 for both datasets, there were lower amplitude peak features in both datasets that were not detected by performing a single pass of the SoGFDE algorithm.

6.2 Residual SoGFDE Results

The following subsections detail the results of initial and residual passes of the SoGFDE algorithm over the DS3 dataset.

6.2.1 DS3 Results

The SoGFDE algorithm parameters for the analysis of DS1 and DS2 were determined using known defect/non-defect regions of the ROI across the entirety of the datasets. As discussed in sections 4.3 and 5.6 an alternate method was employed to enable a more accurate and robust SoG approximation of defect responses in terms of lower RMSE. The following discusses the parameters used and the results obtained.

6.2.1.1 Algorithm Parameters for DS3

Table 6.2. lists the parameters used for the initial and residual SoGFDE process described in section 5.6 for the defect responses in DS3.

Table 6.2 DS3 Initial and Residual Pass SoGFDE Algorithm Parameters

Parameter	Initial Pass Value	Residual Pass Value
m	$\{400,500,\ldots,900\}$	$\{500,600,..900\}$
σ_e	0.006	0.004
Δ	0.004	0.003
β	0.9	0.9
γ	0.025	0.025

As indicated in Table 6.2, the values for σ_e and Δ were widened when compared to Table 6.1 to account for tolerance in the probe diameter and to enable capture of smaller width peaks that may be present in the defect response.

6.2.1.2 SoG Approximation RMSE Results

Using the parameters listed in Table 6.2 the SoGFDE initial and residual feature detection process was executed. For each record in DS3, the SoG Approximation RMSE was obtained for the initial and residual passes. The resulting histograms are provided in Figures 6.12 and 6.13.

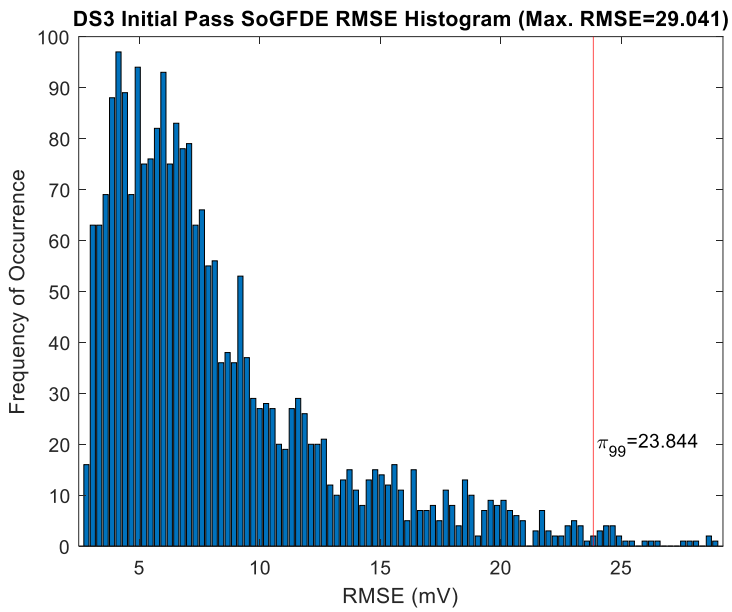

Figure 6.12 DS3 Initial Pass SoG Approximation RMSE Histogram.

The red vertical line in the plot denotes the 99th percentile value for the RMSE histogram.

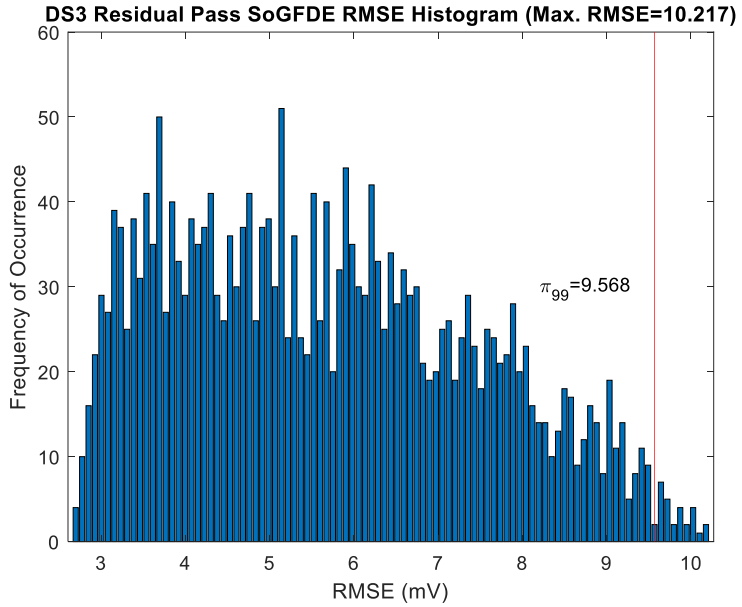

Figure 6.13 DS3 Residual Pass SoG Approximation RMSE Histogram.

The red vertical line in the plot denotes the 99th percentile value for the RMSE histogram.

As indicated in Figures 6.12 and 6.13, performing a second pass of the SoGFDE algorithm on the residual defect response resulted in a factor 2.84 reduction in the Approximation RMSE for the worst case (maximum RMSE) and a factor 2.49 reduction when considering the 99th percentiles of the RMSE values for the records in DS3. Figure 6.14 provides a plot of the SoG approximation for the maximum RMSE in the DS3 dataset.

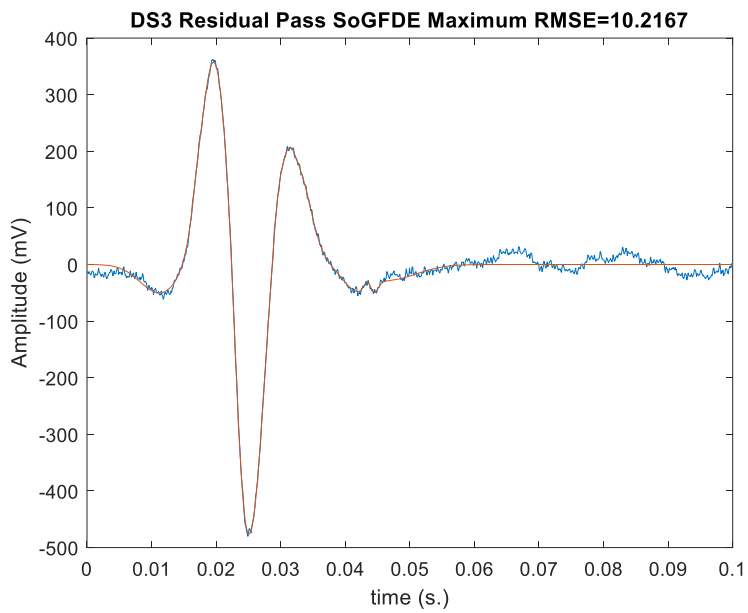

Figure 6.14 DS3 Residual Pass SoG Approximation RMSE Maximum Case.

As indicated in Figure 6.14, even for the worst case SoG approximation RMSE, the SoGFDE algorithm correctly identified the five (5) features present in the defect response with the noise in the interval: $0.06 \leq t \leq 0.1$ ignored.

6.2.1.3 SoG Residual to Estimated Noise SNR Results

In addition to calculating the SoG approximation RMSE for the records in DS3, the SoGFDE final residual errors were compared to the noise estimate records. A histogram of the results is provided in Figure 6.15.

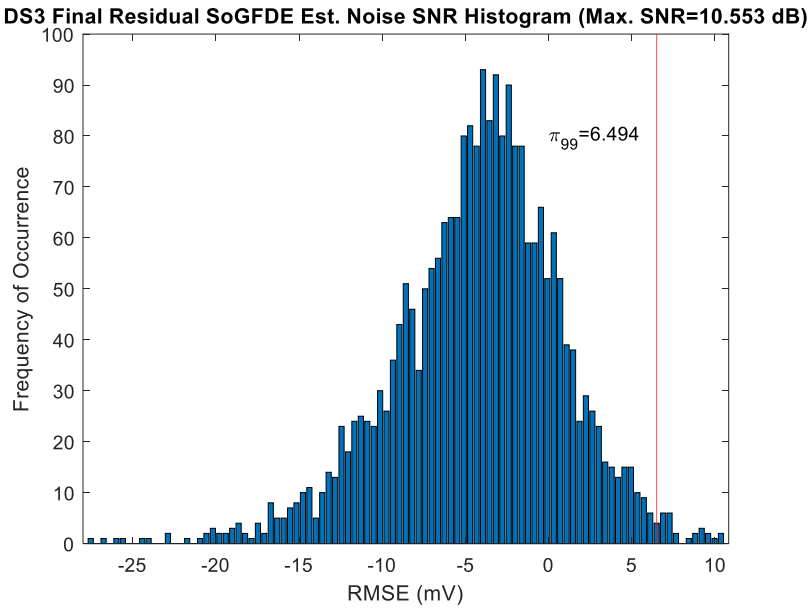

Figure 6.15 DS3 SoG Residual to Estimated Noise SNR Histogram.

The red vertical line in the plot denotes the 99th percentile value for the SNR histogram.

The histogram in Figure 6.15 indicates that 99% of the SoGFDE final residuals for the records in DS3 are less than 2.11:1 SNR. For context, a commonly used minimum SNR listed for EC detection purposes is 3:1 [250]. Using this information, the SoGFDE final residuals for DS3 only contained four (4) records where the SoG final residual would have an SNR large enough to meet the minimal requirements for defect detection. To illustrate the nature of the error between the SoGFDE final residual and the associated noise estimate record, an example of the worst case SoG Residual to Noise Estimate SNR is provided in Figure 6.16.

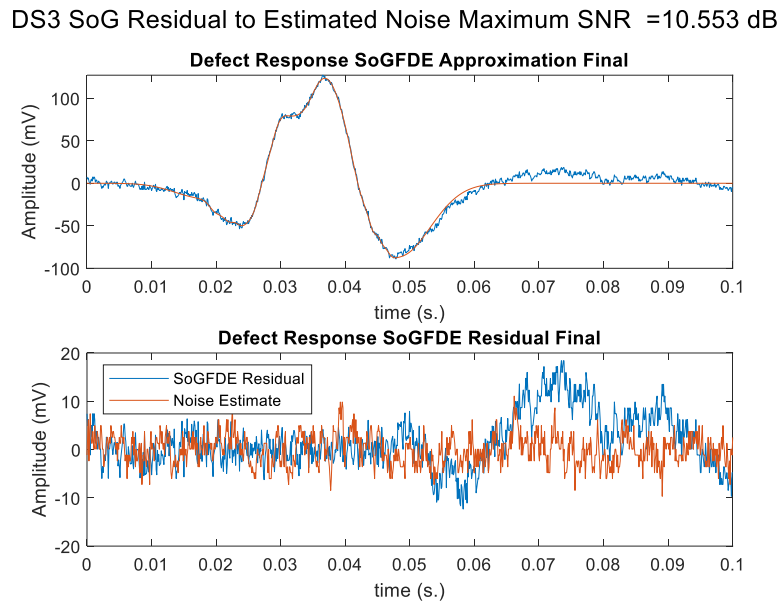

Figure 6.16 DS3 SoG Residual to Estimated Noise SNR Maximum Case.

Referencing Figure 6.16, the SoG approximation closely matches the original response through the defect interval ($0.0 \leq t \leq 0.065\ s.$) and does not capture signal content outside the interval. This is further evidenced by the lower comparison plot of the SoG approximation residual to the associated noise record where the largest discrepancies are seen in the region outside the area of the defect ($0.065 < t \leq 0.1\ s.$)

6.2.1.4 Binary Image Threshold Results

As discussed in section 5.6, during the execution of the SoGFDE Residual Feature detection algorithm the α threshold that resulted in minimal SoG approximation RSME for the initial and residual was obtained. A histogram of the results is provided in Figure 6.17.

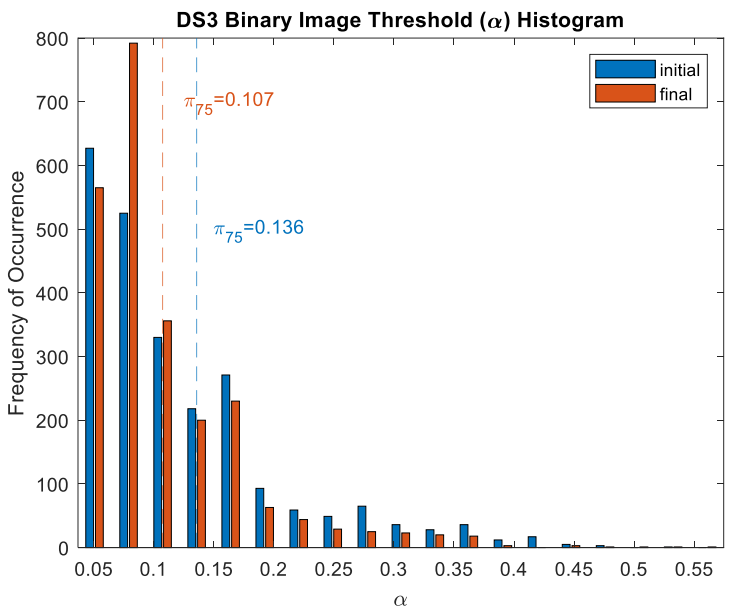

Figure 6.17 DS3 Initial and Residual α Threshold Histograms.

The blue and orange dashed vertical lines in the plot denote the 75th percentile values for the initial and final (respectively) binary image threshold histograms.

As indicated in Figure 6.17, for the range of α values investigated, the histograms show close similarity for the α parameter for both the initial and residual pass of the algorithm with the final α indicating a slightly decreased range (variance) of values referenced by the lower 75th percentile value. The results indicate that the SoGFDE algorithm is detecting and approximating elements that are relevant to the defect response and largely ignoring the noise in the ROI.

6.2.1.5 Comparison to RBFNN Approximation

To investigate the comparative performance of the SoGFDE algorithm against the existing MATLAB RBFNN method a subset of 475 records (consisting of the first five line scans from each calibration sequence) in the DS3 dataset were selected. The RBFNN width parameter

(σ) was varied through a range of values and at each value the dataset records were approximated. A summary of the relevant RBFNN parameters are listed in Table 6.3.

Table 6.3 RBFNN Parameters used for SoGFDE Comparison

Parameter Description	Value(s)
MSE Error Goal	0
Number of Added Neurons per Iteration	1
Maximum No. Neurons	≤ SoGFDE estimated parameters
σ	[0.0005,0.001,0.002,0.003,0.004]

Sigma width parameters were selected to be consistent with the widths considered in the SoGFDE approximation. In addition, the maximum number of RBF neurons were limited in upper bound to the number of parameters utilized in the SoGFDE estimate to ensure fair comparisons.

The results of the experiment are provided in Table 6.4 and Figure 6.17.

Table 6.4 RMSE Comparison Statistics for RBFNN and SoGFDE for DS3 Subset

		Approximation RMSE			
Approximation Method	**RBF σ**	**Min.**	**Mean**	**Max**	**Variance**
RBFNN	0.0005	3.325	13.160	43.014	52.984
	0.001	3.594	9.359	30.318	22.644
	0.002	3.399	7.670	133.080	44.424
	0.003	3.263	19.648	1287.876	7009.378
	0.004	3.210	54.176	4903.559	102832.086
SoGFDE		**2.791**	**5.679**	**14.601**	**3.364**

Lowest RMSE values annotated in bold font. All RMSE values are in units of mV.

As indicated in Table 6.4, the SoGFDE method consistently outperformed the RBFNN method for the neuron width values investigated. An example of one of the common pitfalls of utilizing the RBFNN to estimate D-coil defect signals is provided in Figure 6.18.

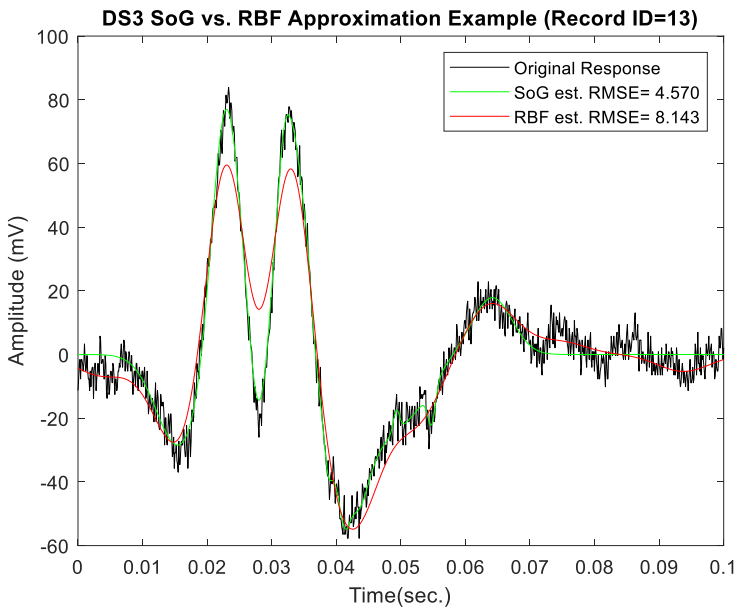

Figure 6.18 RBFNN vs. SoGFDE Approximation Example

As shown in Figure 6.18. the SoGFDE approximation better estimates both the extrema extents of the defect response to include the inflection points that occur between the extents. The constant σ width values of the RBFNN limits its estimative ability. The SoGFDE estimation is more selective in the sense that it ignores the non-defect portions of the signal (i.e., $0 \leq t \leq 0.01$, $0.07 \leq t \leq 0.1$). This point is an example of another shortfall of the RBFNN estimation in that it assumes all data points in the investigated interval are ranked in importance based on the largest remaining contribution to MSE and then attempts to determine the RBF weights (amplitudes) as a linear solution to a set of equations without further constraints. One manifestation of the lack of additional constraints can typically be observed as the large RMSE variance values evidenced in Table 6.4 which clearly indicate RBF kernel node parameters that are outside the solution space of interest.

Lastly, it should be noted that in contrast to the RBFNN algorithm, the SoGFDE method attempts to fit possible "meaningful" features in the defect response (which are determined as the input parameters to the algorithm), and optimizes all three Gaussian parameters (i.e., A, μ, σ) as part of a constrained procedure instead of fitting the Gaussian feature amplitude to an interval.

6.2.2 Results Discussion for DS3

The dual pass SoGFDE algorithm described provides the ability to obtain a smoothed approximation of D-Coil defect responses. In addition, once the SoG features have been extracted (or fit) to the defect response, the resulting parameters provide a dimensionally reduced representation. The reduced representation is better able to approximate the defect response when compared to the existing RBFNN method in terms of reduced RMSE and SoG features that better focus upon the elements of interest to the analyst in the response.

In addition to the approximation of the defect response, the resulting SoG features can be used to create and improve the performance of interpretable ML classifiers as will be discussed in the next two chapters of this dissertation.

CHAPTER VII

SOG FEATURE ASSISTED SAX CLASSIFIERS

7.1 Introduction

As indicated in the literature review, the PAA symbolic representation of time series is a dimensionality reduction method that has been used in numerous applications. Symbolic Aggregate Approximation (SAX) [147] is an extension to PAA that permits further dimensionality reduction and has been used as a basis for time series classification. The following describes a method based on SoG feature representations that can boost the accuracy of the SAX method when used in the classification of D-Coil defect responses. However, prior to introduction of the method, description of previous methods upon which it is based and the techniques used to validate the performance are discussed.

7.2 Methodology

7.2.1 PAA

The PAA method achieves dimensionality reduction of a time series by segmenting the ROI in the time series and using the segment mean as the representative value. Given a time series $\mathbf{d} = [d_1, d_2, \dots, d_n]^T$, and segment length M, the PAA is then calculated as

$$\bar{x}_i = \frac{M}{n} \sum_{j=\frac{n}{M}(i-1)+1}^{\frac{n}{M}i} \left[d_{\frac{n}{M}(i-1)+1}, \dots, d_{\frac{n}{M}i} \right] \tag{7.1}$$

7.2.2 SAX

The SAX method provides a symbolic representation of time series which is an extension of PAA. The method achieves further dimensionality reduction by first performing Z-score normalization on the time series ROI, calculating the segment PAA values then substituting a symbolic code for the segment mean value. The symbolic code is obtained from a predetermined table of mean value discretization intervals which are constructed based on the observation that for many types of normalized time- series segments, the values follow a Gaussian distribution. Utilizing this observation, the symbolic code discretization levels are obtained by partitioning the PAA value Gaussian distribution into equiprobable intervals. The number of symbolic intervals defines the number of symbols in the SAX alphabet for a given instance of the method.

Although SAX is very effective in numerous settings it does have limitations. Researchers have developed enhancements to SAX that address the fact that the method does not adequately discern the series slope or shape in the segment window [254-257] for some applications. Regarding these approaches, some incorporate modifications that could cause issues where interpretability is a concern [258],[259] by altering times series features. Another issue with SAX is the inability to vary the segment window size in the ROI to which researchers have developed enhancement techniques to address the concern [260-265]. Lastly, some researchers have implemented clustering schemes to further optimize the breakpoint intervals [266].

Some of the SAX drawbacks can be observed when the method is used to analyze EC defect response signals. Many approaches to quantitative EC analysis utilize the response peak values [267],[81] to relate a given defect response to its physical characteristics (e.g., depth or length). Due to the nonstationary nature of such signals, statistics such as the mean value for a

specified analysis segment can incorrectly provide an estimation of the defect peak amplitude. This problem is compounded when utilizing the SAX representation as Figure 7.1 illustrates.

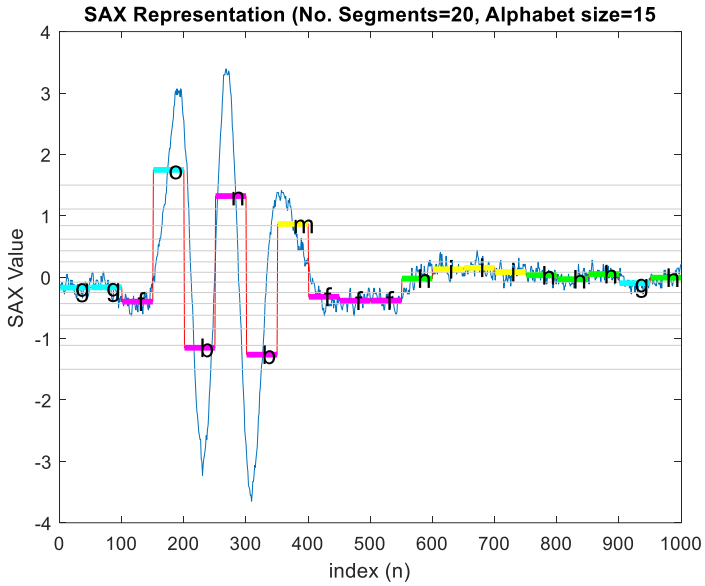

Figure 7.1 SAX Representation of D-Coil Defect Response

Segments in the plot are color coded and are annotated with the appropriate SAX symbol.

Referencing Figure 7.1, it is noted that the peak amplitude information in the defect response is not correctly reflected in the SAX representation. Positive peaks associated with the segments “o” and “n” are opposite in relative value when compared to the actual relative amplitude values due to the drastic change in the response shape within the segment, whereas, the two negative peaks although of different amplitude are both assigned the SAX symbol “b”. The segment size was selected to ensure in all cases in the ROI the defect response peaks were well represented in the analyzed PAA segments.

One of the reasons for the errors in peak representations in Figure 7.1 relates to how the values in a given segment are discretized. The equiprobable Gaussian distribution regions

criterion for discretization in the SAX method results in finer detail in the representation captured as the PAA value tends to zero and larger values are discretized using wider intervals and therefore are assigned the same value. Thus, the discretization method of SAX can create dimensionally reduced symbolic representations of D-coil defect signatures that do not accurately capture the peak content of the response and for quantitative EC analysis that focuses on the extrema in the defect response amplitude, interpretability of the representation can be a concern.

7.2.3 Extended SAX (ESAX)

In an effort overcome some of the limitations of SAX, researchers have investigated methods that provide more information for a given time series segment. One example, the ESAX method [148] extends the SAX method by adding the segment extrema amplitudes in addition to the PAA value. Symbol assignment for the method utilizes the SAX breakpoints and enforces an order of the segment symbols based on the position of occurrence in the segment with the assumption that the segment mean value occurs at the midpoint of the segment.

To address the aforementioned issues with SAX, a novel enhancement to the method based on the SoG features of the defect response is presented.

7.2.4 SoG Feature-Based SAX (SoG-SAX)

The SoG-SAX method presented consists of two components: feature discretization and symbol assignment. Feature discretization is accomplished by performing clustering using the SoG parameter matrices for a collection of defect responses to determine the symbolic code breakpoints not in terms of the segment mean value as in SAX, but the segment extrema values in the SoG estimate of the D-coil defect response. Once the breakpoints are obtained for the

specified SoG-SAX alphabet size, symbol assignment is performed using the SoG estimate for a given defect response and the extrema values for a given segment. Further description of the two component methods employed follow.

7.2.4.1 Feature Discretization

The SoG feature discretization process utilizes clustering to obtain the segment extrema value breakpoints. A brief description of the clustering method employed and the subsequent process to obtain the SoG feature amplitude breakpoints is discussed.

7.2.4.1.1 FCM

The FCM clustering algorithm [268] is considered a soft clustering algorithm in that it provides membership information for a given feature vector for all determined clusters. The technique can be beneficial in cases where there is suspected overlap in clusters and in many studies performs better than K-means [269],[270]. The method employs a weighting exponent (m) to tune the degree of overlap in the cluster membership values for a clustered vector. Assuming a D-dimensional input vector $\mathrm{X} = \{x_1, x_2, \dots, x_n\}, x_k \in \mathbb{R}^d$, the method searches for a matrix of cluster centers $\mathbf{V} = \{v_1, v_2, \dots, v_c\}, v_i \in \mathbb{R}^d$, and data vector membership matrix $\mathbf{U} = \{u_1, u_2, \dots, u_n\}, u_i \in \mathbb{R}^c \mid \sum_{j=1}^{c} u_{ij} = 1; 0 \leq u_{ij} \leq 1;\ 1 \leq i \leq n, 1 \leq j \leq c$, subject to the optimization function:

$$J(U, v) = \sum_{k=1}^{n} \sum_{i=1}^{c} {u_{ik}}^m \|x_k - v_i\|^2 \tag{7.2}$$

with the cluster centers and membership values updated at each iteration as:

$$v_i = \frac{\sum_{k=1}^{n}(u_{ik})^m x_k}{\sum_{k=1}^{N}(u_{ik})^m}; 1 \le i \le c \tag{7.3}$$

$$u_{ik} = \frac{1}{\sum_{j=1}^{c}\left(\frac{\|x_k - v_i\|}{\|x_k - v_j\|}\right)^{\frac{2}{m-1}}}; 1 \le k \le n, 1 \le i \le c \tag{7.4}$$

For the purposes of this study, *m=2* was utilized throughout as it provided the best results in terms of K-fold cross validation classification analysis metrics.

7.2.4.1.2 Feature Discretization Algorithm

Pseudocode for the SoG feature discretization process is listed in Table 7.1.

Table 7.1 SoG-SAX Feature Discretization Algorithm

Algorithm: *SoG-SAX_Feature_Discretization*	
Input: $Dataset\ of\ SoG\ Parameter\ Matrices\ (\mu\ removed)$: $\mathbf{P}_{2xm} = \begin{bmatrix} \boldsymbol{A_1} & \boldsymbol{\sigma_1} \\ \dots & \dots \\ \boldsymbol{A_m} & \boldsymbol{\sigma_m} \end{bmatrix}$ $Sigma\ Lower\ Bound: \sigma_{lb}$ $Alphabet\ Size: a$	
Output: $Amplitude\ Breakpoint\ Vector: \beta_a$	
Step	**Description**
1.	Partition the columns of matrix **P** based on sign of amplitude value A $\mathbf{P} = [\mathbf{P}^{+}_{ix2}]\ [\mathbf{P}^{-}_{jx2}] \quad where\ m = i + j$
2.	Normalize the amplitude columns of $\mathbf{P}^{+}$ and $\mathbf{P}^{-}$ into the intervals [0,1] and [0, -1] respectively.
3.	Construct data matrices $\mathbf{D}^{+}$ and $\mathbf{D}^{-}$ by performing steps 1 and 2 for each defect response in the dataset and concatenating the results.

Table 7.1 (continued)

Step	Description
4.	$\mathbf{D}^{+}(\sigma \leq \sigma_{lb}) = null$ $\mathbf{D}^{-}(\sigma \leq \sigma_{lb}) = null$
5.	$[\mathbf{K}^{+}, \mathbf{C}^{+}] = max\ (FCM\left(\mathbf{D}^{+}, \left\lceil \frac{a}{2} \right\rceil\right))$ $[\mathbf{K}^{-}, \mathbf{C}^{-}] = max\ (FCM\left(\mathbf{D}^{-}, \left\lceil \frac{a}{2} \right\rceil\right))$
6.	$[\mathbf{k}^{+}_{min}, \mathbf{k}^{+}_{max}] = FindClusterAmpExtrema(\mathbf{K}^{+}, \mathbf{D}^{+})$ $[\mathbf{k}^{-}_{min}, \mathbf{k}^{-}_{max}] = FindClusterAmpExtrema(\mathbf{K}^{-}, \mathbf{D}^{-})$
7.	$\boldsymbol{\beta}_{a} = CreateABPVector(\mathbf{k}^{+}_{min}, \mathbf{k}^{+}_{max}, \mathbf{k}^{-}_{min}, \mathbf{k}^{-}_{max})$

As referenced in Table 7.1, the SoG feature dataset only utilizes the A and σ parameters and is decomposed into positive and negative amplitude features prior to amplitude normalization (steps 1,2). Step 4 provides the ability through the hyperparameter σ_{lb}, removal of SoG features of small width prior to the clustering process. This operation has the effect of removing finer feature detail that could negatively influence the breakpoint determination. Next, FCM clustering and locating the cluster extrema in terms of normalized amplitude are performed for the two SoG feature subsets (steps 5,6). Lastly, the cluster amplitude extrema information is used in step 7 to construct the break point vector for the specified alphabet size.

7.2.4.2 Symbol Assignment

Utilizing the normalized amplitude breakpoints identified by clustering of the SoG amplitude and sigma parameters, a variant of the ESAX method using the SoG defect response estimate and the segment extrema amplitude values is constructed. Pseudocode for the proposed method is provided in Table 7.2.

Table 7.2 SoG-SAX Symbol Assignment Algorithm

Algorithm: *SoG-SAX_Symbol_Assignment*	
Input: $Amplitude\ Norm.Sampled\ Signal\ SoG\ Estimate\ \mathrm{Vector}$: $\mathbf{g} = [g_1, g_2, \dots, g_n]^T$ $Number\ of\ Segments: N$ $Alphabet\ Size: a$	
Output: $SoG - SAX\ representation: \boldsymbol{s} = [s_1, s_2, \dots s_{2N}]$	
Step	**Description**
1.	$for\ \ i = 1{:}N$ {
2.	$\mathbf{g}_s = \left[g_{\frac{n}{N}(i-1)+1}, \dots, g_{\frac{n}{N}i}\right]$
3.	$\mathbf{x}_i = FindExtrema\ (\mathbf{g}_s)$
4.	$\mathbf{s}_i = LookupSoGSAXSymbols(\mathbf{x}_i, a)$ }

Referencing Table 7.2, the SoG-SAX symbol assignment algorithm processes the SoG estimate signal that has been normalized to the interval [-1,1] and for each segment locates the extrema values. The extrema values are replaced with symbols using the breakpoints determined previously via the SoG Feature Discretization procedure.

7.2.5 Dataset Description

Utilizing the dual pass SoGFDE parameter matrices obtained for DS3 as well as the defect response extrema values, the dataset was partitioned using an 80/20 training/test split of the 95 calibration sequences. Performing the split based on the calibration sequence index ensures that the training and testing set line scan records are not co-mingled.

Referencing the ECIS calibration procedure discussed in section 4.1, the amplitude extrema in the defect response are used for system gain adjustment prior to inspection. Figure

7.2 indicates the typical extrema values for a calibration sequence in DS3 as referenced by line scan index.

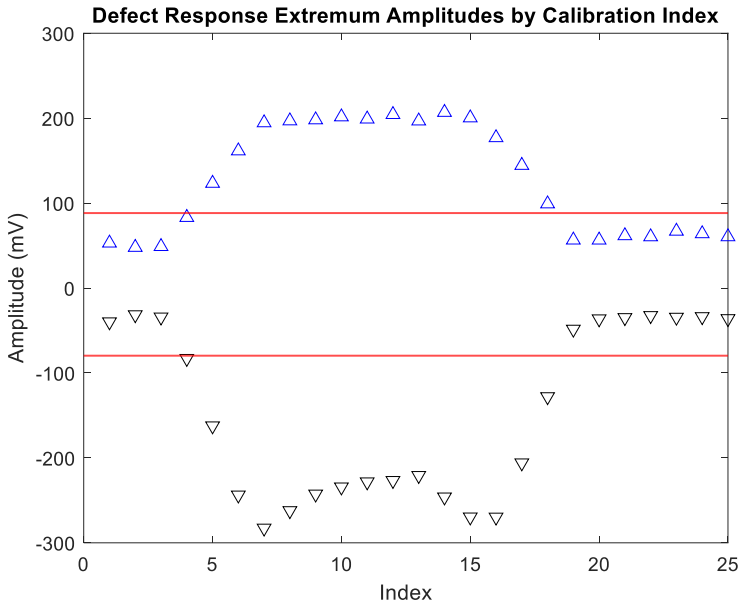

Figure 7.2 DS3 Example Calibration Sequence Defect Response Extrema Amplitude Values by Scan Index.

The DS3 calibration records dataset positive and negative extremum median values are indicated as red horizontal lines.

In Figure 7.2, two zones are identified based on the training dataset extrema amplitude medians. Utilizing the median statistic has numerous examples in the literature as a method for fault detection [271-274] due primarily to its robustness to outliers. Building a binary classifier that can discern defect response patterns based on the extrema features could be useful in quantitative analysis of the calibration sequence for detection of less sensitive EC probe or probe positional misalignment issues.

To this end, the defect responses in the training and testing datasets were partitioned into two classes based on the minimum and maximum amplitudes of the defect response line scans using the training dataset extrema median values as the class thresholds.

Stated formally, for a specified line scan line scan $\mathbf{d}_i$ let $d_{i(min)}$ and $d_{i(max)}$ represent the maximum and minimum values for the line scan $\mathbf{d}_i$. Furthermore, let the training dataset extrema amplitude medians be defined as $\tilde{d}_{min}$ and $\tilde{d}_{max}$ respectively. Utilizing this notation, a summary of the classes for DS3 is provided in Table 7.3.

Table 7.3 DS3 Class Partitioning Criterion

Class ID	**Extremum Amplitude Criterion (mV)**
Positive	$d_{i(\min)} \leq \tilde{d}_{min} \wedge d_{i(max)} \geq \tilde{d}_{max}$
Negative	$d_{i(\min)} \geq \tilde{d}_{min} \wedge d_{i(max)} \leq \tilde{d}_{max}$

For the purposes of binary classification, Table 7.3 defines the positive class as indicative of defect responses that are in close proximity to the expected maximum probe response for the scanned EDM notch. By contrast, the negative class defect responses are all the remaining responses that are lower than the training dataset extrema amplitude medians.

7.2.6 Classifier Design and Analysis Metrics

Details of the classifier designs and analysis metrics used for evaluation of DS3 are discussed in the following subsections.

7.2.6.1 1-NN Classification

In numerous studies [275-277], analysis of the efficacy of time series symbolic representation is performed through use of 1-NN classification. The rationale is that the method

provides a direct measure of the effectiveness of the representation in terms of classification accuracy which is obtained by a similarity measure. In addition, the result is not influenced by hyperparameters. This study investigated 1-NN performance using Euclidean similarity measure for a binary classification task.

7.2.6.2 SVM

The SVM has been utilized in numerous quantitative EC analysis classification investigations as indicated in the literature review. The method seeks to define an optimal hyperplane between identified support vector features in the training set that best separate the dataset classes. Although not consider inherently interpretable classifier designs [278], linear and quadratic SVM classifiers were employed in this study as a method to measure the effectiveness of the 1-NN classifier in terms of commonly previously applied classifier methods.

7.2.7 Analysis Metrics

The analysis metrics employed in this study are defined in Table 7.4.

Table 7.4 Classification Analysis Metrics

Class ID	**Predicted Result**	
Positive	True Positive (TP)	False Negative (FN)
Negative	False Positive (FP)	True Negative (TN)
Precision	$\frac{TP}{TP + FP}$	
Recall	$\frac{TP}{TP + FN}$	
Accuracy	$\frac{TP + TN}{TP + FP + TN + FN}$	
F1-Score	$\frac{2(Precision * Recall)}{Precision + Recall}$	

K-fold cross validation (K=10) was performed on the DS1 training set to determine the optimal alphabet size and selection of σ_{lb} in terms of largest mean F1-Score.

7.3 Results

The following subsections detail the relevant results obtained by processing the DS3 dataset utilizing the SoG-SAX, SAX, and ESAX methods.

7.3.1 Clustering Results

The DS3 training set records were processed by the aforementioned SoG feature discretization procedure. Due to the random initialization of the FCM procedure, the clustering process was repeated for 50 separate iterations on each of the SoG feature subsets. The resulting means of the cluster centers and membership matrices were then calculated. The clustering results are provided in Figure 7.3

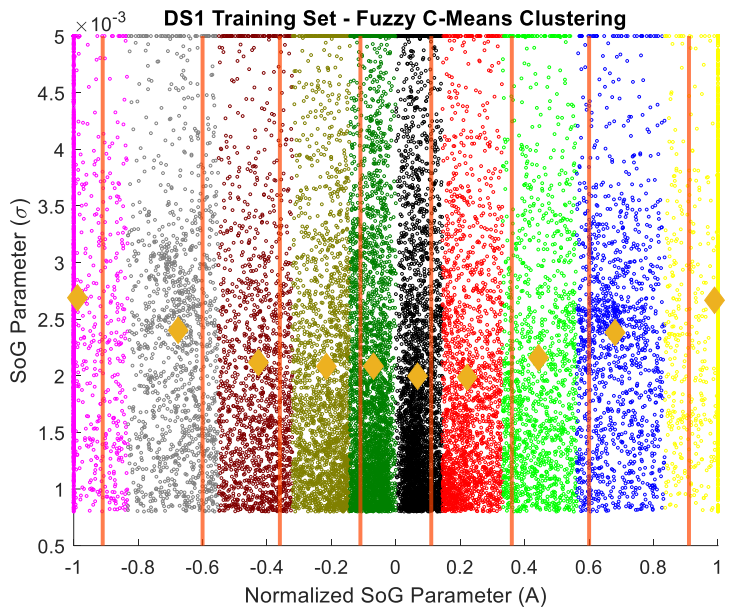

Figure 7.3 DS3 Training Set FCM Clustering Result

Diamond markers in the plot indicate the cluster centers. The vertical lines indicate the associated SAX alphabet breakpoints. The SoG-SAX parameters used were σ_{lb}= 0.0008, a=11.

Referencing the scatter plot in Figure 7.3, vertical bands in amplitude are clearly present. For reference, vertical annotation lines are provided indicating the breakpoints for an associated SAX alphabet size (a=11) for the amplitude region investigated. It is noted that the spacing of the clusters (i.e., SoG parameter symbolic amplitude discretization intervals) are noticeably smaller in size than the SAX intervals.

7.3.2 Parameter Determination Results

K-fold Cross Validation (K=10) was performed on the DS3 training set to determine the optimal parameters for the SAX, ESAX, and SoG-SAX methods. The criterion for parameter selection was the mean F1-Score. The results are provided in Tables 7.5 through 7.7 with the maximum mean F1-Score and associated method parameter values annotated in bold font.

Table 7.5 DS3 Training Set 10-Fold Cross Validation Mean F1-Score Results (SAX).

Alphabet Size	**F1 Score**
8	0.9290
9	0.9362
10	0.9319
11	**0.9384**
12	0.9338
13	0.9375

Table 7.6 DS3 Training Set 10-Fold Cross Validation Mean F1-Score Results (ESAX).

Alphabet Size	**F1 Score**
8	0.8851
9	0.8841
10	0.8877
11	0.8843
12	**0.8892**
13	0.8801

Table 7.7 DS3 Training Set 10-Fold Cross Validation Mean F1-Score Results (SoG-SAX).

$\boldsymbol{\sigma_{lb}}$	Alphabet Size			
	9	10	**11**	12
0	0.9168	0.9124	0.9276	0.9199
0.0004	0.9161	0.9125	0.9263	0.9173
0.0008	0.9264	0.9203	**0.9283**	0.9255
0.0012	0.9127	0.9137	0.9224	0.9164

7.3.3 Classification Results

Utilizing the parameter values determined by the K-fold cross validation studies for the symbolic representation methods, binary classifiers were created and the DS3 testing set was

classified. The results are presented in Table 7.8 with the highest classification accuracy and F1-Score annotated in bold font.

Table 7.8 DS3 Testing Set Classification Results

Representation Method	Test Counts				Precision	Recall	Accuracy	F1 Score
	TP	FN	FP	TN				
SAX	207	11	31	226	0.870	0.950	0.912	0.908
ESAX	206	12	48	209	0.811	0.945	0.874	0.873
SoG-SAX	207	11	14	243	0.937	0.950	**0.947**	**0.943**
LSVM	201	17	31	226	0.866	0.922	0.899	0.8933
QSVM	198	20	12	245	0.943	0.908	0.933	0.925

Referencing Table 7.8, the SoG-SAX based 1-NN classifier outperformed both SVM classifiers (utilizing SoG-SAX features) achieving a 1.9% improvement in F1-Score over the QSVM classifier. The SoG-SAX based classifier also outperformed the defect response representations using the SAX and ESAX largely due to better discernment of the negative class records in the DS3 testing set resulting in a classification accuracy and F1-Score improvement of 3.8%.and 3.9% respectively over the SAX based classifier. An example comparing the SAX and SoG-SAX matching 1-NN records for one of the SAX misclassified negative class records is provided in Figure 7.4.

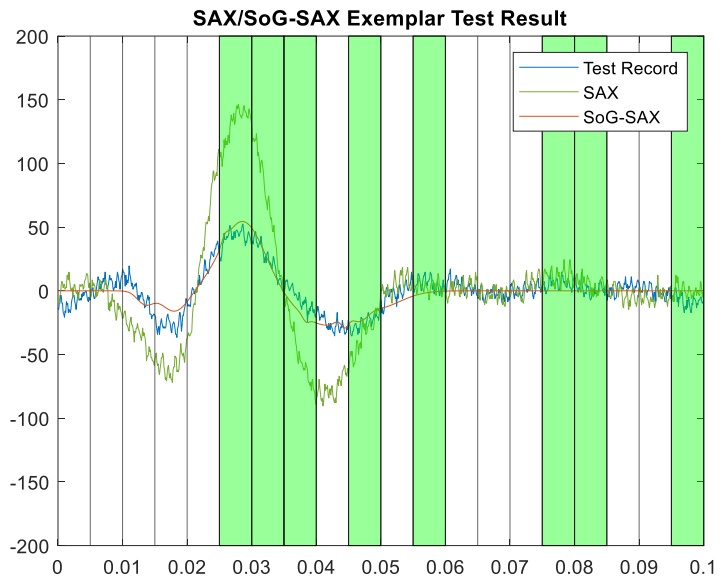

Figure 7.4 SAX/SoG-SAX Comparison for Exemplar Test Record.

Vertical lines in the plot indicate the segment endpoints with each segment representing a symbol. Shaded segments in the plot map to the same SAX symbol for the test record and the matching 1-NN SAX classifier record. Note the closer agreement in peak amplitude for the matching 1-NN SoG-SAX classifier record resulting in correct classification.

7.4 Discussion

The SoG-SAX method described in this dissertation based on SoG representations of D-coil defect responses provide quantifiable improvement over the SAX and ESAX methods. The use of FCM clustering of the SoG amplitude and width features provides an alternative technique to determining segment feature value breakpoints than that employed by the SAX method. The SoG-SAX method reduces the dimension of the original data by a factor of 25 (1000/40) which drastically reduces the number of calculations necessary for classification. In addition, due to the use of extrema features in the estimated defect response, the interpretability of the symbolic representation is increased for the defect responses studied.

The 1-NN classification method and the usage of the defect response amplitude extrema provide useful information to the EC inspector regarding the quality of a given defect response in terms of a corpus of past recorded results.

CHAPTER VIII

SOG FEATURE ASSISTED PAA BASED PNN CLASSIFIERS

8.1 Introduction

As indicated in the literature review, PNN classifiers have been used to discern EC defect responses in terms of material type or condition. To demonstrate the effectiveness of SoG representations in boosting the performance of PNN based classifiers when investigating EC phenomena using D-coil type probes, an experiment was conducted utilizing a subset of the data records from the DS3 dataset. The methodology used, associated results and discussion follow.

8.2 Methodology

8.2.1 Dataset Description

In numerous investigations in the literature review, researchers utilized the width of the petals and the extrema in the Lissajous defect response pattern as features in classification applications. When translated to time-based representations of an EC signal, these features relate to the distance between the extrema in the signal. Therefore, when analyzing time-based EC signals one logical design for a classifier would be one that was able to detect possible time anomalies between the extrema in the defect response. To simulate this scenario, a subset of DS3 was constructed by calculating the time interval between the extrema in the SoG approximation defect responses and creating classes based on the data. The criteria used and the resulting dataset is summarized in Table 8.1.

Table 8.1 DS3 Subset for PNN Classification

Class ID	Extremum Time Interval (s.)	No. Samples
Positive	$0.003 \leq t \leq 0.006$	391
Negative	$0.007 \leq t \leq 0.03$	721

Referencing Table 8.1, for the purposes of binary classification, the positive class is indicative of DS3 defect responses that are expected for the specified EC probe coil diameter and scan speed with the lower and upper bounds calculated based on the listed tolerances for the coil diameter used for inspection. By contrast, the negative class represents defect responses that fall outside the expected values in terms of the time interval between the extrema. To demonstrate the relevance of such a partitioning of DS3, examples of the defect responses considered are shown in Figure 8.1.

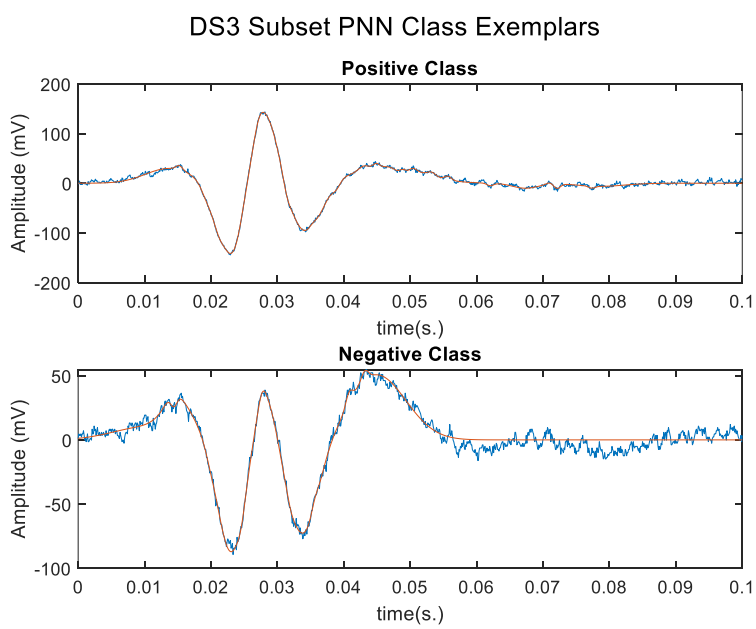

Figure 8.1 DS3 Subset PNN Class Exemplar Defect Responses

In Figure 8.1, the defect response for the positive class contains extrema typically seen when the EC probe is positioned close to the maximum response from the EDM notch. The time interval in the response extrema correspond to the expected width based on the scan speed and coil. By contrast, the negative class defect response in the figure contains a maximum peak that is well outside the expected location which is typical of the probe position outside the region of optimal response.

After the assignment of classes to each defect response line scan in the subset of DS3, it was partitioned using an 80/10/10 training/validation/test split.

8.2.2 The PNN Classifier

The PNN classifier could be considered an interpretable design in that it has a very simple internal structure. In addition, it possesses a very simple training process. The records in the training set form a set of class weights for the classifier. Each weight undergoes a nonlinear activation process when compared to an unknown record and Bayesian analysis is used to classify the result. A diagram of the process is provided in Figure 8.2

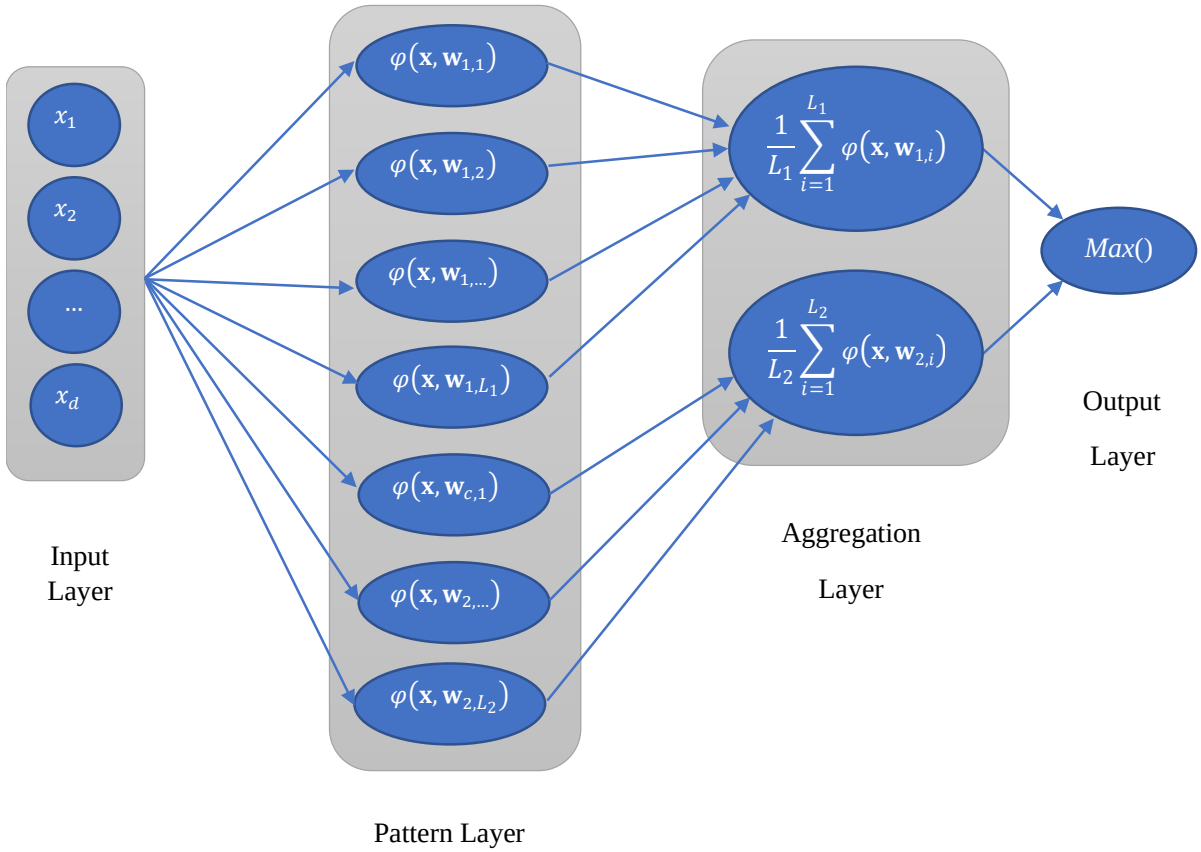

Figure 8.2 PNN Functional Diagram

As indicated in Figure 8.2 the PNN consists of four layers. The input layer is fully connected to each training pattern (weight) in the pattern layer. For the purposes of this study, the activation function shown in Figure 8.2 utilizes the Gaussian function with a specified spread parameter. Stated mathematically, let $\mathbf{W}_{dxN}$ be the normalized training set weight vectors in the Pattern layer and $\mathbf{x}_{dx1}$ be a normalized input vector from the test set. The activation function for the ith node in the pattern layer is then,

$$\varphi(\mathbf{x}, \boldsymbol{w_i}) = \exp\left(-\frac{(\mathbf{x} - \boldsymbol{w_i})^2}{2\sigma_s^2}\right) \tag{8.1}$$

Expanding the above expression:

$$\varphi(\mathbf{x}, \boldsymbol{w_i}) = \exp\left(\frac{(\mathbf{x} - \boldsymbol{w_i})^T(\mathbf{x} - \boldsymbol{w_i})^T}{2\sigma_s^2}\right)$$

$$\varphi(\mathbf{x}, \boldsymbol{w_i}) = \exp\left(-\frac{\mathbf{x}^T\mathbf{x} + \mathbf{w}_i\mathbf{w}_i^2 - 2\mathbf{w}_i^T\mathbf{x}}{2\sigma_s^2}\right)$$

$$\varphi(\mathbf{x}, \boldsymbol{w_i}) = \exp\left(\frac{\mathbf{w}_i^T\mathbf{x} - 1}{\sigma_s^2}\right) \tag{8.2}$$

Central to the development of equation 8.2 is the normalization of the weights and input vectors which reduces the number of calculations by simplification of the activation function.

The Aggregation layer in Figure 8.2 calculates the activation average values for each specified class and assigns a classification decision based on the class average maximum value (Output layer).

One of the key elements of PNN classifiers as evidenced by equation 8.1 is the squared Euclidean distance of the test vector and the classifier weights. When classifying time series, reduced representations that enhance the relevant features in the time series, while reducing or removing irrelevant features can provide the ability to increase classification accuracy and interpretability.

One drawback to PNNs is that they can be computationally expensive in that for a record to be classified the similarity measure must be computed between all weights in the classifier. If the weight values in the Pattern layer are of high dimensionality (as can be the case in time series) the number of calculations can dramatically increase. One method to reduce the computational burden and possibly increase the capacity of the PNN in terms of additional

weights would be the use of dimensionally reduced representations (e.g., downsampling, wavelet representations) of the features. However, care must be taken when implementing such schemes in EC analysis that the peaks of the defect response are preserved. Example of some of the pitfalls are provided in Figure 8.3.

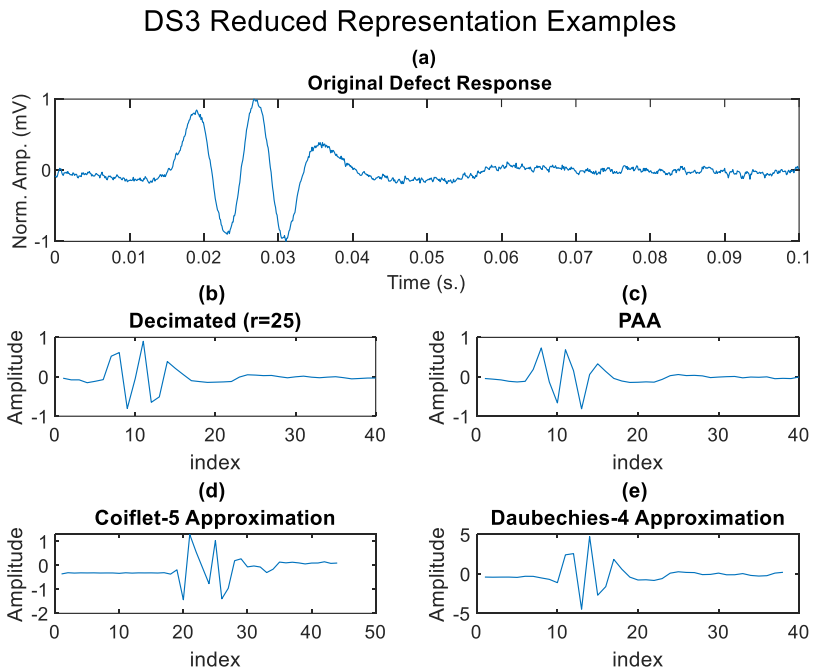

Figure 8.3 DS3 Example Response Reduced Representations

(a) Amplitude normalized defect response from DS3, (b) decimation of (a) by a factor of 25, (c) PAA (40 segments), (c) Coiflet-5 approximation coefficients (MRA level=6), (d) Daubechies-4 approximation coefficients (MRA level=5). MRA level for the wavelet representations were selected to be consistent with the representation lengths in (b) and (c).

Figure 8.3 shows four dimensionally reduced representations of the defect response in (a) which was normalized in amplitude onto the interval [-1,1]. The decimated representation in (b) maintains the overall structure of the original defect response, but begins to lose the signal maximal extent information due to indiscriminate nature of the decimation process. In addition,

the relative amplitudes of the negative peaks do not match the original signal. In (b) the PAA representation; again, reduction in amplitude is observed and the positive peak relative amplitudes do not match the original signal. The Coiflet approximation in (d) bears little resemblance to the original signal. In (e) the Daubechies approximation incorrectly identifies the original signal extrema. The wavelet implementations (d) and (e) are larger in amplitude scale due to the filtering structure of wavelet-based analysis.

Utilizing dimensionally reduced representations such as those indicated in Figure 8.3 could present problems in interpretability and create issues when there is a need to determine the correctness of the ML application.

8.2.3 SoG Feature Assisted PAA (SoG-PAA)

In an effort to address the issues discussed in Section 8.2.2, the utility of SoG based representations were investigated. SoG based defect response representations provide defect response amplitude location information through the μ parameter. Table 8.2 provides the pseudocode of a modification to the PAA procedure which exploits the information provided by the SoG representation.

Table 8.2 SoG-PAA Pseudocode

Algorithm: SoG-PAA
Input: $Amplitude\ Normalized\ Sampled\ Signal\ SoG\ Estimate\ \mathrm{Vector}$: $\mathbf{f}_n = [s_0, s_1, \dots, s_{\mathrm{N}-1}]^T$ $sampling\ instant\ vector$: $\mathbf{t}_s = [t_s = 0, t_1, \dots, t_{n-1}]^T$ $Amplitude\ Normalized\ SoG\ Parameter\ Matrix$: $\mathbf{P} = \begin{bmatrix} A_{n(1)} & & A_{n(M)} \\ \mu_1 & , \dots, & \mu_{(M)} \\ \sigma_1 & & \sigma_{(M)} \end{bmatrix}$ $Number\ of\ PAA\ segments$: k
Output: $SoG\ Feature\ PAA\ Assisted\ Representation\ Vector$: $\mathbf{y}$

Table 8.2 (continued)

Step	Description
1	$\mathbf{T}_{i(\mathrm{kx2})} = FindPAATimeIntervalExtents(\mathbf{t}_{\boldsymbol{s}}, k)$
2:	$\mathbf{F}_{i(\mathrm{kxM})} = FindSoGFeatureIntervalMemberships(\mathbf{T}_{\boldsymbol{i}}, \mathbf{p}_{\boldsymbol{\mu}}, \mathbf{t}_{\boldsymbol{s}})$
3:	for i=1:k
4:	$idxs = SoGFeatureCheck(\mathbf{F}_{\boldsymbol{i}}(i,:))$
5:	if $(isempty\ (idxs))$
6:	$y(i) = PAA(\mathbf{f}_n(\mathbf{T}_i(i,1):\mathbf{T}_i(i,2))$
7:	else
8	$y(i) = extremum\ (\mathbf{f}_n(\mathbf{T}_i(i,1):\mathbf{T}_i(i,2))$

Referencing the algorithm in Table 8.2, steps 1 and 2 determine the time intervals for the segments in the PAA representation and the segments that contain SoG features per the SoG parameter μ. Steps 4 through 8 then perform the normal PAA calculations with the exception that when a segment that contains SoG features is encountered, the extremum amplitude of the SoG estimate in the interval is substituted in place of the normal PAA value.

8.2.4 Analysis Metrics

Due to the binary nature of the classes of defect responses utilized in this study the analysis metrics used were those identified in section 7.2.7.

8.3 Results

The SoG-PAA representation of the exemplar record in Figure 8.3 was calculated and qualitatively compared to the PAA representation. In addition, PNN classifiers were constructed using the defect response representations investigated in Figure 8.3 as well as SoG-PAA. The results follow.

8.3.1 Qualitative Comparison

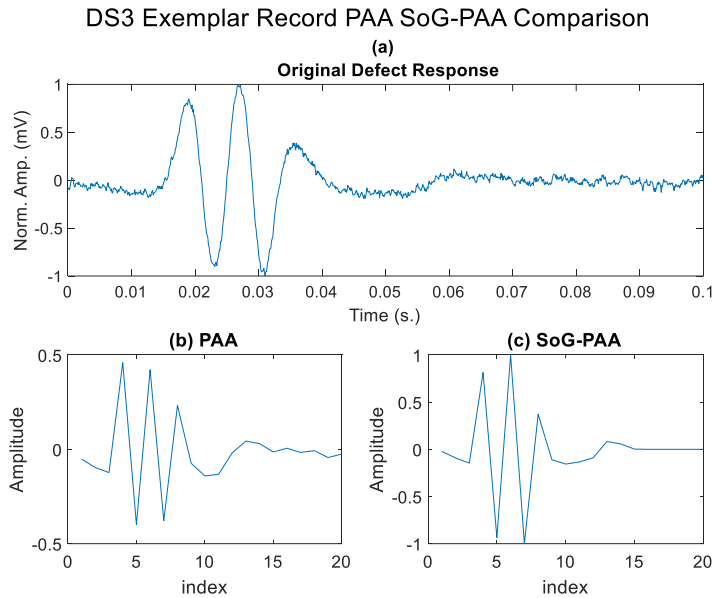

Figure 8.4 DS3 Exemplar Response SoG-PAA Comparison to PAA

The defect response in (a) is the same as in Figure 8.3. The bottom plots show the PAA and SoG- PAA representations at even lower scale (20 segments) than the representations in Figure 8.3 (40 segments).

As indicated in Figure 8.4, the SoG-PAA representation better captures the relative peak amplitudes in the defect response as compared to the PAA method. In addition, due to the restriction of the expected width (σ_e) in the SoGFDE algorithm, non-defect areas of the ROI (30 $\leq$ index $\leq$ 40) are minimized and therefore their influence in the distance calculations for the PNN classifier pattern layer are subsequently decreased.

8.3.2 PNN Classification Results

PNN Classifiers were constructed using PAA, SoG Assisted PAA, Coiflet-5, and Dabeches-4 representations of the subset of defect responses in DS3. For each classifier, the PNN Spread Parameter was varied through a range which was empirically determined. At each

iteration, the validation set classes were predicted by the resulting PNN classifier and the classification accuracy recorded. Selection of the PNN spread parameter used for the testing set was the PNN spread parameter that resulted in the maximum classification accuracy on the validation set. The classification results are provided in Table 8.3.

Table 8.3 DS3 PNN Classification Results

Representation	**PNN Spread Parameter**	**Test Counts**				**Precision**	**Recall**	**Accuracy**	**F1 Score**
		TP	**FN**	**FP**	**TN**				
PAA	0.1037	35	2	3	72	0.9211	0.9459	0.9554	0.9333
SoG-PAA	0.0569	37	0	2	73	0.9487	1	**0.9821**	**0.9737**
Coiflet-5	0.6900	37	0	4	71	0.9024	1	0.9643	0.9487
Daubechies-4	0.8600	35	2	2	73	0.9459	0.9459	0.9643	0.9459

Relevant maximum values are highlighted in bold font.

Referencing Table 8.3, classifiers for the four representations performed similarly in classification accuracy with the range of accuracy values of 2.67% and F1 Score range of 4.04%. It is noted however, that the classifier using the SoG-PAA representation boosted the precision of the PAA based classifier improving the classification accuracy by 2.79% and F1 Score by 4.33%. In addition, the SoG-PAA classifier had the highest classification accuracy and F1 Score for the dataset and classifiers tested. It should be noted that the SoG-PAA and PAA representations consisted of 20 elements, whereas the Coiflet-5 and Daubechies-4 representations were of lengths 44 and 38 respectively. Thus, the SoG-PAA performance was attained using defect response representations approximately half the length of the wavelet systems studied.

8.4 Discussion

Figure 8.4 indicates issues with existing time series representation methods that implement averaging and equivalently low pass filtering can negatively impact the peak amplitude features in the D-coil defect response. In scenarios wherein the internals of the ML method (here the PNN classifier) must be demonstrated to an external approval authority, utilizing defect response representations that not only reduce the dimensionality, but maintain traceable properties to the original data ease the interpretability burden as well as improve the computational drawbacks to the PNN classifier.

CHAPTER IX

CONCLUSIONS

9.1 Conclusion Discussion

This study provides the methods and frameworks to automatedly decompose D-coil EC defect responses as a summation of basic Gaussian function elements that are referenced to the physical dimensions of the coil and inspection scan rate. The elements reduce the dimensionality of the defect response in ways that enable greater interpretability in terms of relevant features (amplitude peaks and widths) when compared to other current methods. In addition, the SoG-based representations were demonstrated to show increased classification performance when compared to other classification schemes utilizing existing time series dimensionality reduction methods.

RMSE as a similarity method has been indicated in numerous studies to be a fragile measure. One manifestation of this fragility is that slight translations in the two time-series to be compared can result in significant changes in the RMSE. Time series dimensionality reduction methods such as PAA and SAX partly attempt to reduce this fragility by the use of singular features that represent the ROI. However, as demonstrated in this study, the use of SoG representations can improve the segment descriptive ability of these methods.

In many instances, the ability to quickly locate past reference responses can be of concern to the EC analyst providing the ability to answer questions typically posed during data mining tasks such as, “How unique is the queried response in terms of past inspections?” The SoG-SAX

method demonstrated in this study coupled with the 1NN classifier provides a relatively simple and interpretable framework to answer such questions.

9.2 Suggestions for Further Study

This study focused a small subset of EC inspection scenarios in terms of materials, defect dimensions, inspection frequency, and inspection coil diameter. One avenue for future research could be expanded study of the presented methods in these areas. In addition, there are other research domains such as ultrasonic inspection and ground penetrating radar which generate A-scan signals somewhat similar to those observed for D-coil EC analysis that could be investigated using the aforementioned methods.

Another area for further study could be extensions to the basic Gaussian element functions. As an example, Gaussian functions possess an inflection point at the function maximum (μ). This information could be used to construct piecewise Gaussian functions that would have different widths on either side of this inflection point. In this case the parameters would be $(A, \mu, \sigma_l, \sigma_r)$. Such functions could be used as the basic elements that perhaps could achieve greater dimensionality reduction. Along these lines, the efficacy of other element functions such as Gaussian derivatives or piecewise modifications to them could be investigated.

SoGFDE algorithm execution speed improvements could be made by optimizing the opening and closing MM operations to only consider the binary image regions along the main diagonal as this is the only region where the relevant response content exists. Execution speed in this area of the SoGFDE algorithm could further be improved by parallelizing the processing of the binary defect response images. The constrained optimization portion of the SoGFDE algorithm only considered the Interior Point method as the method converged more consistently than other methods. Analysis of the reasoning for these results could be an opportunity for

future study. Additionally, the computational complexity of the SoGFDE algorithm could be contrasted with other RBFNN implementations in an effort to better understand accuracy vs. complexity tradeoffs.

The study of SoG-PAA considered only two wavelet systems (Coiflet, Daubechies) for symbolic representations. Future work should consider an expanded set of such systems that possess attributes that are more similar (e.g., Morlet, Ricker) to D-coil defect responses.

Interpretability was narrowly defined in this study. Future works could expand upon the definition to include more subjective measures of interpretability such as analysis of SoG based defect signature representations by domain experts.

REFERENCES

[1] H. Rowshandel, G. L. Nicholson, J. L. Shen, and C. L. Davis, “Characterisation of clustered cracks using an ACFM sensor and application of an artificial neural network,” NDT & E International, vol. 98, pp. 80–88, Sep. 2018, doi: 10.1016/j.ndteint.2018.04.007.

[2] D. P. Johnston, J. A. Buck, P. R. Underhill, J. E. Morelli, and T. W. Krause, “Pulsed Eddy-Current Detection of Loose Parts in Steam Generators,” IEEE Sensors J., vol. 18, no. 6, pp. 2506–2512, Mar. 2018, doi: 10.1109/JSEN.2018.2793234.

[3] R. Zhou, “A Kullback-Leibler Divergence Filter for Anomaly Detection in Non-Destructive Pipeline Inspection,” M. Sc. Thesis, Univ. of Ottawa, Ottawa, Canada, 2020

[4] L. Brasche, “The Use of Nondestructive Inspection in Jet Engine Applications,” Materials Evaluation, vol. 60, no. 7, 2002

[5] C. G. Annis, J. S. Cargill, J. A. Harris, and M. C. Van Wanderham, “Engine Component Retirement-for-Cause: A Nondestructive Evaluation (NDE) and Fracture Mechanics-based Maintenance Concept,” JOM, vol. 33, no. 7, pp. 24–28, Jul. 1981, doi: 10.1007/BF03339447.

[6] J. N. Yang and Shiung Chen. "An exploratory study of retirement for cause of gas turbine engine components." Journal of Propulsion and Power 2.1, pp. 38-49, 1986.

[7] White, Paul. Review of methods and approaches for the structural risk assessment of aircraft. Defense Science and Technology Organization Victoria (Australia) Air Vehicles Div., 2006.

[8] Sweeting, Trevor. "Statistical models for nondestructive evaluation," International Statistical Review/Revue Internationale de Statistique, pp. 199-214, 1995.

[9] P.W. Hovey, A.P. Berens, “Statistical Evaluation of NDE Reliability in the Aerospace Industry,” D.O. Thompson, D.E. Chimenti (eds) Review of Progress in Quantitative Nondestructive Evaluation. Boston, MA.: Springer,1998, https://doi.org/10.1007/978-1-4613-0979-6_108

[10] Berens, Alan P. Probability of Detection (POD) Analysis for the Advanced Retirement for Cause (RFC)/Engine Structural Integrity Program (ENSIP) Nondestructive Evaluation (NDE) System-Volume 1: Pod Analysis, Univ. of Dayton Research Inst., 2000.

[11] A.P. Berens, "Analysis of the RFC/NDE system performance evaluation experiments." Review of Progress in Quantitative Nondestructive Evaluation, pp 987-994. Boston, MA.: Springer, 1987.

[12] D. J. Hagemaier, Fundamentals of Eddy Current Testing. American Society for Nondestructive Testing, 1990.

[13] N. Bowler, Eddy-Current Nondestructive Evaluation. New York, NY: Springer New York, 2019, doi: 10.1007/978-1-4939-9629-2.

[14] P.E. Mix, Introduction to nondestructive testing: A training guide, Hoboken: Wiley-Interscience, 2005

[15] Uniwest, “Us-500 e-lab,” [Online]. Available: https://www.uniwest.com/us-500-e-lab. [Accessed: 07-Aug-2021].

[16] M. Leethy and R. Olding, “Advanced Nondestructive Evaluation (NDE) for Retirement for Cause/Engine Structural Integrity Program (RFC/ENSIP)”, AFRL, Wright-Patterson AFB, OH, USA, Rep. no. AFRL-ML-WP-TR-2000-4144, Aug. 2000, [Online]. Available: https://apps.dtic.mil/dtic/tr/fulltext/u2/a388904.pdf

[17] C. Pairazaman, S. Keller, C. Bynak, “A Third Generation Robotic Eddy Current System for the Inspection of Gas Turbine Engine Components,” World Conf. on NDT., vol. 15, Rome, Italy, Oct 2000.

[18] Iowa State University Center for Nondestructive Evaluation, “NDE-Ed.org: About NDT and NDE”, 2021, [Online]. Available: https://www.nde-ed.org/NDETechniques/EddyCurrent/ProbesCoilDesign/ProbesModeOp.xhtml

[19] R.D. Mooers and J.C. Aldrin, “Effects of angular variation on split D differential eddy current probe response”, AIP Conference Proceedings, vol. 1706, Feb 2016, doi:10.1063/1.4940559

[20] B. A. Auld and J. C. Moulder, “Review of Advances in Quantitative Eddy Current Nondestructive Evaluation,” Journal of Nondestructive Evaluation, vol. 18, pp. 3–36, 1999, doi: https://doi.org/10.1023/A:1021898520626.

[21] A. Bernieri, G. Betta, L. Ferrigno, M. Laracca and S. Mastrostefano, "Multifrequency Excitation and Support Vector Machine Regressor for ECT Defect Characterization," IEEE Transactions on Instrumentation and Measurement, vol. 63, no. 5, pp. 1272-1280, May 2014, doi: 10.1109/TIM.2013.2292326.

[22] U.S. Department of Defense, MIL-HDBK-1823: A Nondestructive Evaluation System Reliability Assessment, 2009

[23] S. Seo, G. Choi, T. J. Eom, B. Lee, and S. Y. Lee, “Correlation of eddy current responses between fatigue cracks and electrical-discharge-machining notches,” Met. Mater Int., vol. 23, no. 4, pp. 756–763, Jul. 2017, doi: 10.1007/s12540-017-6738-1.

[24] S. Ross and W. Lord, "Eddy current crack signals in small diameter tubing.", Review of Progress in Quantitative Nondestructive Evaluation, vol. 11, pp. 307-313, Boston, MA.: Springer, 1992

[25] S. Ross and W. Lord, “Eddy current calibration of fatigue cracks using EDM notches”, Review of Progress in Quantitative Nondestructive Evaluation, vol. 14, pp. 2043-2049, Boston, MA.: Springer, 1995.

[26] D. O. Thompson, D. E. Chimenti, and B. A. Auld, “John Moulder and the Evolution of Model-based Quantitative Eddy Current NDE,” Review of progress in quantitative nondestructive evaluation, vol. 18A, pp. 441–448, New York: Kluwer Academic / Plenum Publishers, 1999.

[27] H. A. Sabbagh, "Nondestructive evaluation," IEEE Potentials, vol. 13, no. 5, pp. 35-38, Dec. 1994-Jan. 1995, doi: 10.1109/45.464651.

[28] H. L. Libby, Introduction to electromagnetic nondestructive test methods. New York: Wiley-Interscience, 1979

[29] M. L. Burrows, “A Theory of Eddy-current Flaw Detection”, Ph. D dissertation, Univ. of Michigan, 1964

[30] J.D. Jackson, Classical Electrodynamics, 3rd. Ed. New York: John Wiley& Sons, 1998, pp. 218-223

[31] A. J. Bahr, “Microwave Eddy-Current Techniques for Quantitative Nondestructive Evaluation”, Eddy-Current Characterization of Materials and Structures, ASTM STP 722, pp. 311-381, 1981.

[32] B. A. Auld, “Theoretical Characterization and Comparison of Resonant-Probe Microwave Eddy-Current Testing with Conventional Low-Frequency Eddy–Current Methods”, Eddy-Current Characterization of Materials and Structures, ASTM STP 722, pp.332-347, 1981.

[33] C.V. Dodd, W.E. Deeds, "Analytical Solutions to Eddy-Current Probe-Coil Problems", Journal of Applied Physics, 39, pp. 2829-2838, 1968, https://doi.org/10.1063/1.1656680

[34] C.T. Tai, Dyadic Green's Functions in Electromagnetic Theory, Intext Educational Publishers, 1971

[35] J. R. Bowler, "Eddy current calculations using half-space Green's functions", Journal of Applied Physics, 61, 1987, pp. 833-839, https://doi.org/10.1063/1.338131

[36] J. R. Bowler, L. D. Sabbagh and H. A. Sabbagh, "A theoretical and computational model of eddy-current probes incorporating volume integral and conjugate gradient methods", IEEE Transactions on Magnetics, vol. 25, no. 3, pp. 2650-2664, May 1989, doi: 10.1109/20.24505.

[37] Z. Badics, Y. Matsumoto, K. Aoki, F. Nakayasu, M. Uesaka and K. Miya, "An effective 3-D finite element scheme for computing electromagnetic field distortions due to defects in eddy-current nondestructive evaluation," IEEE Transactions on Magnetics, vol. 33, no. 2, pp. 1012-1020, Mar. 1997, doi: 10.1109/20.558521.

[38] Y. Le Bihan, J. Pavo, M. Bensetti and C. Marchand, "Computational environment for the fast calculation of ECT probe signal by field decomposition," IEEE Transactions on Magnetics, vol. 42, no. 4, pp. 1411-1414, April 2006, doi: 10.1109/TMAG.2006.872516.

[39] L.D. Sabbagh, H.A Sabbagh, "Development of a System to Invert Eddy-Current Data and Reconstruct Flaws", Review of progress in quantitative nondestructive evaluation, vol. 2A, pp. 1555-1571, Boston, MA: Springer, 1983.

[40] S. J. Norton and J. R. Bowler, "Theory of eddy current inversion," Journal of Applied Physics, vol. 73, no. 2, pp. 501–512, Jan. 1993, doi: 10.1063/1.353359.

[41] Y. Li, L. Udpa, and S. S. Udpa, "Three-Dimensional Defect Reconstruction from Eddy-Current NDE Signals Using a Genetic Local Search Algorithm," IEEE Trans. Magn., vol. 40, no. 2, pp. 410–417, Mar. 2004, doi: 10.1109/TMAG.2004.824116.

[42] S. Bilicz, E. Vazquez, S. Gyimothy, J. Pavo, and M. Lambert, "Kriging for Eddy-Current Testing Problems," IEEE Trans. Magn., vol. 46, no. 8, pp. 3165–3168, Aug. 2010, doi: 10.1109/TMAG.2010.2043418.

[43] R. Douvenot, M. Lambert, and D. Lesselier, "Adaptive Metamodels for Crack Characterization in Eddy-Current Testing," IEEE Trans. Magn., vol. 47, no. 4, pp. 746–755, Apr. 2011, doi: 10.1109/TMAG.2011.2105883.

[44] S. Bilicz, "Sparse Grid Surrogate Models for Electromagnetic Problems with Many Parameters", IEEE Trans. Magn., vol. 52, no. 3, pp. 1–4, Mar. 2016, doi: 10.1109/TMAG.2015.2477241.

[45] M. Kermadi, S. Moussaoui, A. Taieb Brahimi, and M. Feliachi, “Defect localization and characterization in eddy current nondestructive testing by change detection and global optimization,” COMPEL, vol. 37, no. 2, pp. 948–970, Mar. 2018, doi: 10.1108/COMPEL-05-2017-0201.

[46] F. Desobry, M. Davy, and C. Doncarli, “An online kernel change detection algorithm,” IEEE Trans. Signal Process., vol. 53, no. 8, pp. 2961–2974, Aug. 2005, doi: 10.1109/TSP.2005.851098.

[47] R. D. Mooers, J. S. Knopp, J. C. Aldrin, and S. Sathish, “Split D differential probe model validation using an impedance analyzer,” 40th Annual Review of Progress in QNDE, Baltimore, Maryland, USA, 2014, pp. 1511–1518. doi: 10.1063/1.4865002.

[48] R.K Murphy, H.A. Sabbagh, J. Chan and E. H Sabbagh, “A Volume Integral Code for Electromagnetic Nondestructive Evaluation,” Proceedings of the 13th Annual Review of Progress in Applied Computational Electromagnetics, March 1997

[49] J.A. McMahan and A.K. Criner, “Statistical Flaw Characterization Through Bayesian Shape Inversion from Scattered Wave Observations,” AIP Conference Proceedings, vol. 1706, 130005, 2016, https://doi.org/10.1063/1.4940608

[50] J. A. McMahan, J. C. Aldrin, E. Shell, and E. Oneida, “Bayesian flaw characterization from eddy current measurements with grain noise,” AIP Conference Proceedings, vol. 1806, 1, 2017, doi: 10.1063/1.4974692.

[51] Q.H. Nguyen, L.D. Philipp, D.J. Lynch, and A.F. Pardini, “Steam tube defect characterization using eddy current Z-Parameters,” Res. Nondestruct. Eval, 1998, 10, pp. 227-252.

[52] W. Lord and S. R. Satish, “Fourier Descriptor Classification of Differential Eddy Current Probe Impedance Plane Trajectories,” Review of Progress in Quantitative Nondestructive Evaluation, D. O. Thompson and D. E. Chimenti, Eds. Boston, MA: Springer US, 1984, pp. 589–603. doi: 10.1007/978-1-4684-1194-2_56.

[53] MacQueen, J., “Some methods for classification and analysis of multivariate observations”, Proceedings of the fifth Berkeley Symposium on mathematical statistics and probability, vol. 1, No. 14, 1967

[54] S. S. Udpa and W. Lord, “Fourier Descriptor Classification of Magnetite Buildup in Power Steam Generators,” Review of Progress in Quantitative Nondestructive Evaluation, D. O. Thompson and D. E. Chimenti, Eds. Boston, MA: Springer US, 1986, pp. 233–240. doi: 10.1007/978-1-4615-7763-8_25.

[55] J. Jarmulak, “A Method of Representing and Comparing Eddy Current Lissajous Patterns,” Review of Progress in Quantitative Nondestructive Evaluation, D. O. Thompson and D. E. Chimenti, Eds. Boston, MA: Springer US, 1997, pp. 303–308. doi: 10.1007/978-1-4615-5947-4_39.

[56] C. S. Burrus, R. A. Gopinath, H. Guo, Introduction to Wavelets and Wavelet Transforms A Primer, New Jersey: Prentice Hall, 1998

[57] J. S. Walker, A Primer on WAVELETS and Their Scientific Applications, 2nd ed., New York: Chapman & Hall/CRC, 2008

[58] S.-J. Song and Y.-K. Shin, “Eddy current flaw characterization in tubes by neural networks and finite element modeling,” NDT & E International, vol. 33, no. 4, pp. 233–243, Jun. 2000, doi: 10.1016/S0963-8695(99)00046-8.

[59] D.F. Specht, Probabilistic neural networks for classification, mapping, or associative memory, IEEE International Conference on Neural Networks, 1, pp. 525–532, July,1988.

[60] D. F. Specht, Probabilistic Neural Networks and Polynomial Adaline as Complementary Techniques for Classification, IEEE Trans. on Neural Networks, vol. 1, n. 1, pp. 111-121, March 1990.

[61] D.E. Rumelhart, G.E. Hinton, R.J. Williams, “Learning internal representations by error propagation”, Parallel distributed processing, 1. Cambridge, MA: MIT Press, p. 318–62., 1986

[62] S. Haykin, Neural Networks and Learning Machines, 3rd ed., New Jersey, Pearson Education, 2009

[63] N. H. Jo and H.-B. Lee, “A novel feature extraction for eddy current testing of steam generator tubes,” NDT & E International, vol. 42, no. 7, pp. 658–663, Oct. 2009, doi: 10.1016/j.ndteint.2009.05.006.

[64] G. D’Angelo, M. Laracca, S. Rampone, and G. Betta, “Fast Eddy Current Testing Defect Classification Using Lissajous Figures,” IEEE Trans. Instrum. & Meas., vol. 67, no. 4, pp. 821–830, Apr. 2018, doi: 10.1109/TIM.2018.2792848.

[65] G. D’Angelo, M. Laracca, and S. Rampone, “Automated Eddy Current non-destructive testing through low definition Lissajous figures,” 2016 IEEE Metrology for Aerospace (MetroAeroSpace), Florence, Italy, Jun. 2016, pp. 280–285. doi: 10.1109/MetroAeroSpace.2016.7573227

[66] N. Friedman, D. Geiger, and M. Goldszmidt, “Bayesian network classifiers,” Mach. Learn., vol. 29, no. 2, pp. 131–163, Nov. 1997.

[67] J. R. Quinlan, C4. 5: programs for machine learning. Elsevier, 2014.

[68] L. Yin, B. Ye, Z. Zhang, Y. Tao, H. Xu, J.R.S. Avila, and W. Yin, “A novel feature extraction method of eddy current testing for defect detection based on machine learning,” NDT & E International, vol. 107, p. 102108, Oct. 2019, doi: 10.1016/j.ndteint.2019.04.005

[69] T. M. Cover and P. E. Hart, “Nearest Neighbor Pattern Classification”, IEEE Trans. Inform. Theory, vol. IT-13, pp 21-27, Jan 1967.

[70] J. Grman, R. Ravas, and L. Syrova, “Using of Neural Networks For Classification And Data Analysis In Eddy–Current Testing,” Journal of Electrical Engineering, 53, no. 1-2, pp. 3-9, 2002.

[71] M. Faraj, F. Samsuri, A. Abdalla, D. Rifai, and K. Ali, “Adaptive Neuro-Fuzzy Inference System Model Based on the Width and Depth of the Defect in an Eddy Current Signal,” Applied Sciences, vol. 7, no. 7, p. 668, Jun. 2017, doi: 10.3390/app7070668.

[72] M. Das, H. Shekhar, X. Liu, R. Polikar, P. Ramuhalli, L. Udpa, and S. Udpa, "A generalized likelihood ratio technique for automated analysis of bobbin coil eddy current data," NDT&E Int., vol. 35, pp. 329-336, 2002.

[73] S. M. Kay, Fundamentals of Statistical Signal Processing Vol. 2. Detection Theory, 1st ed., New Jersey: Prentice-Hall, 1998

[74] H. L. Van Trees, K.L. Bell, Z. Tian, Detection, Estimation, and Modulation Theory Part 1 – Detection, Estimation and Filtering Theory, 2nd ed., New Jersey: John Wiley & Sons, 2013

[75] B. Guepie, M. Petreczky, and S. Lecoeuche, “Eddy Currents Signatures Classification by Using Time Series: a System Modeling Approach,” Annual Conference of the PHM Society, vol. 6, no. 1, 2014

[76] V. Vapnik, The Nature of Statistical Learning Theory, Springer-Verlag, 1995

[77] S. Barcherini, L. Cipiccia, M. Maggi, S. Fiori, and P. Burrascano, “Non-destructive test by the Hopfield network,” Proceedings of the IEEE-INNS-ENNS International Joint Conference on Neural Networks. IJCNN 2000. Neural Computing: New Challenges and Perspectives for the New Millennium, Como, Italy, 2000, pp. 381–386 vol.6. doi: 10.1109/IJCNN.2000.859425.

[78] J.J. Hopfield and D.W. Tank, “Neural Computation of Decision in Optimization Problems”, Biological Cybernetics, Vol. 52, pp. 141 – 152, 1985

[79] M. Angeli, P. Burrascano, E. Cardelli, S. Fiori, and S. Resteghini, “Classification of eddy current NDT data by probabilistic neural networks,” IJCNN’99. International Joint Conference on Neural Networks. Proceedings (Cat. No.99CH36339), Washington, DC, USA, 1999, vol. 6, pp. 4012–4014. doi: 10.1109/IJCNN.1999.830801.

[80] I. Galleske, J. Castellanos, “Probabilistic Neural Networks with rotated kernel functions,’ Gerstner W., Germond A., Hasler M., Nicoud JD. (eds) Artificial Neural Networks — ICANN'97. ICANN 1997. Lecture Notes in Computer Science, vol 1327. Springer, Berlin, Heidelberg. https://doi.org/10.1007/BFb0020184

[81] J. García-Martín, J. Gómez-Gil, and E. Vázquez-Sánchez, “Non-Destructive Techniques Based on Eddy Current Testing,” Sensors, vol. 11, no. 3, pp. 2525–2565, Feb. 2011, doi: 10.3390/s110302525.

[82] Eua-Anant, N., Udpa, L., & Chao, J., “Morphological Processing for Crack Detection in Eddy Current Images of Jet Engine Disks,” Review of Progress in Quantitative Nondestructive Evaluation, 1999, pp. 751-758, doi:10.1007/978-1-4615-4791-4_96

[83] J. Serra and P. Soille, Mathematical Morphology and its Applications to Image Processing, Dordrecht: Springer Netherlands, 1994

[84] R. M. Haralick, S. R. Sternberg, and X. Zhuang, “Image Analysis Using Mathematical Morphology,” IEEE Trans. Pattern Anal. Mach. Intell., vol. PAMI-9, no. 4, pp. 532–550, Jul. 1987, doi: 10.1109/TPAMI.1987.4767941.

[85] R. C. Gonzalez and R.E. Woods, Digital Image Processing, 4th ed., New York: Pearson, 2018

[86] S. Gao and L. Udpa, “An Adaptive Morphological Filter for Defect Detection in Eddy Current Aircraft Wheel Inspection,” Review of Progress in Quantitative Nondestructive Evaluation, D. O. Thompson and D. E. Chimenti, Eds. Boston, MA: Springer US, 1998, pp. 1965–1972. doi: 10.1007/978-1-4615-5339-7_255.

[87] F. Lingvall and T. Stepinski, “Automatic detecting and classifying defects during eddy current inspection of riveted lap-joints,” NDT & E International, vol. 33, no. 1, pp. 47–55, Jan. 2000, doi: 10.1016/S0963-8695(99)00007-9.

[88] K. Pearson, "On Lines and Planes of Closest Fit to Systems of Points in Space," Philosophical Magazine, 2, 11, pp. 559–572, doi:10.1080/14786440109462720., 1901

[89] H. Hotelling, “Analysis of a complex of statistical variables into principal components,” Journal of Educational Psychology, 24, pp. 417–441, 498–520.,1933

[90] G. Beylkin, R. Coifman, and V. Rokhlin, “Fast wavelet transforms and numerical algorithms”, Comm. Pure Appl. Math., 44, pp. 141–183, 1991

[91] I. Daubechies, Ten Lectures on Wavelets, SIAM, 1992.

[92] D. L. Donoho, I. M. Johnstone, “Ideal spatial adaptation by wavelet shrinkage,” Biometrika, Vol. 81, Issue 3, pp. 425–455, September 1994, https://doi.org/10.1093/biomet/81.3.425

[93] G. Chen, A. Yamaguchi, and K. Miya, “A novel signal processing technique for eddy-current testing of steam generator tubes,” IEEE Trans. Magn., vol. 34, no. 3, pp. 642–648, May 1998, doi: 10.1109/20.668059.

[94] I. Daubechies, “Orthonormal Bases of Compactly Supported Wavelets,” Comm. Pure Appl. Math., Vol 41, pp. 906-966, 1988.

[95] F. C. Morabito, “Independent component analysis and neural approaches to the extractior of features from NDT/NDE,” IJCNN’99. International Joint Conference on Neural Networks. Proceedings (Cat. No.99CH36339), Washington, DC, USA, 1999, vol. 6, pp. 4021–4026, doi: 10.1109/IJCNN.1999.830803.

[96] J. Karhunen, E. Oja, L. Wang, R. Vigario, and J. Joutsensalo, “A class of Neural Networks for Independent Component Analysis”, IEEE Trans. on Neural Networks, Vo1.8, No.3, pp. 486-504, May 1997

[97] T. Kohonen, “Self-Organized formation of topologically correct feature maps,” Biological Cybernetics, Vol.44, pp. 59-69, 1982

[98] B. Ye, P. Huang, M. Fan, X. Gong, D. Hou, G. Zhang, and Z. Zhou, “Automatic classification of eddy current signals based on kernel methods,” Nondestructive Testing and Evaluation, vol. 24, no. 1–2, pp. 19–37, Mar. 2009, doi: 10.1080/10589750802002590.

[99] J. Morlet, G. Arens, E. Fourgeau, and D. Giard, “Wave propagation and sampling theory – Part I: Complex signal and scattering in multilayered media,” Geophysics, 47, pp. 203-221, 1982a.

[100] J. Morlet, G. Arens, E. Fourgeau, and D. Giard, “Wave propagation and sampling theory – Part II: Sampling theory and complex waves: Geophysics,” 47, pp. 222-236, 1982b.

[101] B. Scholkopf, A. Smola, and K.R. Muller, Nonlinear component analysis as a kernel eigenvalue problem, Neural Computation, 10, 5, pp. 1299–1319, 1998.

[102] L. Kaufman and P. J. Rousseeuw, Finding Groups in Data: An Introduction to Cluster Analysis, New Jersey: John Wiley & Sons, 1990

[103] M. Fan, Q. Wang, B. Cao, B. Ye, A. Sunny, and G. Tian, “Frequency Optimization for Enhancement of Surface Defect Classification Using the Eddy Current Technique,” Sensors, vol. 16, no. 5, p. 649, May 2016, doi: 10.3390/s16050649.

[104] L. S. Rosado, T. G. Santos, M. Piedade, P. M. Ramos, and P. Vilaça, “Advanced technique for non-destructive testing of friction stir welding of metals,” Measurement, vol. 43, no. 8, pp. 1021–1030, Oct. 2010, doi: 10.1016/j.measurement.2010.02.006.

[105] L. S. Rosado, F. M. Janeiro, P. M. Ramos, and M. Piedade, “Defect Characterization With Eddy Current Testing Using Nonlinear-Regression Feature Extraction and Artificial Neural Networks,” IEEE Trans. Instrum. Meas., vol. 62, no. 5, pp. 1207–1214, May 2013, doi: 10.1109/TIM.2012.2236729.

[106] I. Goodfellow, Y. Bengio, and A. Courville. Deep Learning, MIT press, 2016.

[107] J. E. Ball, D. T. Anderson, C. S. Chan Sr., "Comprehensive survey of deep learning in remote sensing: theories, tools, and challenges for the community," J. Appl. Rem. Sens., 11(4), 042609, 23 September 2017 https://doi.org/10.1117/1.JRS.11.042609

[108] T. Meng, Y. Tao, Z. Chen, J.R.S. Avila, Q. Ran, Y. Shao, R. Huang, Y. Xie, Q. Zhao, Z. Zhang, and H. Yin, “Depth Evaluation for Metal Surface Defects by Eddy Current Testing using Deep Residual Convolutional Neural Networks,” arXiv:2104.02472 [cs, eess], Mar. 2021, Accessed: Aug. 04, 2021. [Online]. Available: http://arxiv.org/abs/2104.02472

[109] K. He, X. Zhang, S. Ren, and J. Sun, “Deep Residual Learning for Image Recognition,” 2016 IEEE Conference on Computer Vision and Pattern Recognition (CVPR), pp. 770–778, Jun. 2016.

[110] K. He, X. Zhang, S. Ren, and J. Sun, “Identity Mappings in Deep Residual Networks,” Computer Vision – ECCV 2016, ser. Lecture Notes in Computer Science, B. Leibe, J. Matas, N. Sebe, and M. Welling, Eds., pp. 630–645. Cham: Springer International Publishing, 2016.

[112] S. Xie, R. Girshick, P. Dollár, Z. Tu, and K. He, “Aggregated Residual Transformations for Deep Neural Networks,” 2017 IEEE Conference on Computer Vision and Pattern Recognition (CVPR), pp. 5987–5995, Jul. 2017.

[113] T. Chady, M. Enokizono, and R. Sikora, “Crack detection and recognition using an eddy current differential probe,” IEEE Trans. Magn., vol. 35, no. 3, pp. 1849–1852, May 1999, doi: 10.1109/20.767393.

[114] T. Chady, M. Enokizono, R. Sikora, T. Todaka, and Y. Tsuchida, “Natural crack recognition using inverse neural model and multi-frequency eddy current method,” IEEE Trans. Magn., vol. 37, no. 4, pp. 2797–2799, Jul. 2001, doi: 10.1109/20.951310.

[115] T. Chady and P. Lopato, “Flaws Identification Using an Approximation Function and Artificial Neural Networks,” IEEE Trans. Magn., vol. 43, no. 4, pp. 1769–1772, Apr. 2007, doi: 10.1109/TMAG.2007.892515.

[116] J. Harmouche, C. Delpha, D. Diallo, and Y. Le Bihan, “Statistical Approach for Nondestructive Incipient Crack Detection and Characterization Using Kullback-Leibler Divergence,” IEEE Trans. Rel., vol. 65, no. 3, pp. 1360–1368, Sep. 2016 doi: 10.1109/TR.2016.2570549.

[117] S. Kullback and R. A. Leibler, “On information and sufficiency,” Ann. Math. Statist., vol. 22, pp. 79–86, 1951

[118] T. M. Cover and J. A. Thomas, Elements of Information Theory, 2nd ed., Hoboken, NJ, USA: Wiley, 2006.

[119] X. Zhang, C. Delpha, and D. Diallo, “Jensen-Shannon Divergence for Non-Destructive Incipient Crack Detection and Estimation,” IEEE Access, vol. 8, pp. 116148–116162, 2020, doi: 10.1109/ACCESS.2020.3004658.

[120] J. Lin, "Divergence measures based on the Shannon entropy," IEEE Trans. on Information Theory, vol. 37, no. 1, pp. 145-151, Jan. 1991, doi: 10.1109/18.61115.

[121] A. Hyvarinen, ``Fast ICA for noisy data using Gaussian moments," Proc. IEEE Int. Symp. Circuits Syst. (ISCAS), vol. 5, pp. 57-61, May/Jun. 1999

[122] M. Basseville and I. Nikiforov, Detection of Abrupt Changes: Theory and Application, Englewood Cliffs, NJ, USA: Prentice-Hall, 1993.

[123] C. Delpha, D. Diallo, H. Al Samrout, and N. Moubayed, “Multiple incipient fault diagnosis in three-phase electrical systems using multivariate statistical signal processing," Eng. Appl. Artif. Intell., vol. 73, pp. 68-79, Aug. 2018.

[124] B. Efron and R. J. Tibshirani, An introduction to the bootstrap. CRC press, 1994.

[125] P. Banerjee, S. Safdarnejad, L. Udpa, and S. Udpa, “Investigation of a comprehensive confidence measure in NDE,” AIP Conference Proceedings, 1650, pp. 1948–1957, 2015, doi: 10.1063/1.4914822.

[126] G. J. McLachlan and K. E. Basford. Mixture models: Inference and applications to clustering. Vol. 38. New York: M. Dekker, 1988.

[127] P. Banerjee, S. Safdarnejad, L. Udpa, and S. Udpa, “Ensemble of classifiers for confidence-rated classification of NDE signal,” AIP Conference Proceedings, 1706, 2016, doi: 10.1063/1.4940631.

[128] R. E. Schapire, “The strength of weak learnability”, Mach. Learn., 5, pp.197–227, 1990, https://doi.org/10.1007/BF00116037

[129] R. E. Schapire and Y. Singer, “Improved boosting algorithms using confidence-rated predictions,” Proceedings of the eleventh annual conference on Computational learning theory - COLT’ 98, Madison, Wisconsin, United States, 1998, pp. 80–91. doi: 10.1145/279943.279960.

[130] J. Bao, B. Ye, X. Wang, and J. Wu, “A Deep Belief network and Least Squares Support Vector Machine Method for Quantitative Evaluation of Defects in Titanium Sheet Using Eddy Current Scan Image,” Front. Mater., vol. 7, p. 576806, Sep. 2020, doi: 10.3389/fmats.2020.576806.

[131] G. E. Hinton and R. R. Salakhutdinov,” Reducing the dimensionality of data with neural networks”, Science 313, 504, 2006, doi:10.1126/science.1127647

[132] P. Smolensky, “Parallel distributed processing: Explorations in the microstructure of cognition, vol. 1. chapter Information Processing in Dynamical Systems,” Foundations of Harmony Theory, pp. 194–281. MIT Press, Cambridge, MA, USA, 1986

[133] J. A. K. Suykens, and J. Vandewalle, “Least squares support vector machine classifiers,” Neural Process. Lett. 9, pp. 293–300, 1999, doi:10.1023/A:1018628609742

[134] G. A. F. Seber and A. J. Lee, Linear Regression Analysis, 2nd ed., New Jersey, USA: John Wiley & Sons, 2003

[135] W. Deng, J. Bao, and B. Ye, “Defect Image Recognition and Classification for Eddy Current Testing of Titanium Plate Based on Convolutional Neural Network,” Complexity, vol. 2020, pp. 1–10, Oct. 2020, doi: 10.1155/2020/8868190.

[136] Y. LeCun, B. Boser, J. S. Denker, D. Henderson, R. E. Howard, W. Hubbard, and L. D. Jackel, “Backpropagation applied to handwritten zip code recognition,” Neural Computation, vol. 1, no. 4, pp. 541–551, 1989.

[137] D. E. Rumelhart, G.E. Hinton, and R. J. Williams, “Learning internal representations by error propagation,” Parallel Distributed Processing. Vol 1: Foundations, Cambridge, MA: MIT Press, 1986.

[138] P. Zhu, Y. Cheng, P. Banerjee, A. Tamburrino, and Y. Deng, “A novel machine learning model for eddy current testing with uncertainty,” NDT & E International, vol. 101, pp. 104–112, Jan. 2019, doi: 10.1016/j.ndteint.2018.09.010.

[139] E. Candes, X. Li, Y. Ma, J. Wright, “Robust principal component analysis”, J. ACM, 58, 3, 2011, doi:10.1145/1970392.1970395.

[140] K. P. Murphy, Machine Learning A Probabilistic Perspective, Cambridge, MA: MIT Press, 2012

[141] G. Hinton, N. Srivastava, and K. Swersky, “University of Toronto, Computer Science Dept. - RMSprop: Divide the gradient by a running average of its recent magnitude”, 2021, [Online]. Available: https://www.cs.toronto.edu/~tijmen/csc321/slides/lecture_slides_lec6.pdf

[142] Y. Gal and Z. Ghahramani, “Bayesian convolutional neural networks with Bernoulli approximate variational inference”, arXiv preprint arXiv:1506.02158.

[143] H. A. Dau, A. Bagnall, K. Kamgar, C. C. M. Yeh, Y. Zhu, S. Gharghabi, C. A. Ratanamahatana, and E. Keogh, “The UCR Time Series Archive,” arXiv:1810.07758 [cs, stat], Sep. 2019, Accessed: Mar. 03, 2022. [Online]. Available: http://arxiv.org/abs/1810.07758

[144] R. Agrawal, F. Christos, and S. Arun, "Efficient similarity search in sequence databases," International conference on foundations of data organization and algorithms, Berlin, Heidelberg: Springer, 1993.

[145] B. D. Fulcher, “Feature-based time-series analysis,” Feature Engineering for Machine Learning and Data Analytics, 1st ed., Florida: CRC Press, 2018

[146] E. Keogh, K. Chakrabarti, M. Pazzani, and S. Mehrotra, “Dimensionality Reduction for Fast Similarity Search in Large Time Series Databases,” Knowledge and Information Systems, vol. 3, no. 3, pp. 263–286, Aug. 2001, doi: 10.1007/PL00011669.

[147] J. Lin, E. Keogh, L. Wei, and S. Lonardi, “Experiencing SAX: a novel symbolic representation of time series,” Data Min Knowl. Disc, vol. 15, no. 2, pp. 107–144, Aug. 2007, doi: 10.1007/s10618-007-0064-z.

[148] B. Lkhagva, Yu Suzuki and K. Kawagoe, "New Time Series Data Representation ESAX for Financial Applications," 22nd International Conference on Data Engineering Workshops (ICDEW'06), 2006, doi: 10.1109/ICDEW.2006.99.

[149] K. S. Hatwar and S. S. Badhiye, “Alphabetic time series representation using trend based approach,” IEEE International Conference on Innovations in Information, Embedded and Communication Systems (ICIIECS), 2015

[150] J. Dan, W. Shi, F. Dong, and K. Hirota, “Piecewise Trend Approximation: A Ratio-Based Time Series Representation,” Abstract and Applied Analysis, vol. 2013, pp. 1–7, 2013, doi: 10.1155/2013/603629.

[151] F. L. K. Chung, T. C. Fu, W. P. R. Luk, and V. T. Y. Ng, "Flexible time series pattern matching based on perceptually important points," Workshop on Learning from Temporal and Spatial Data in International Joint Conference on Artificial Intelligence, 2001.

[152] Y. Lexiang and E. Keogh, "Time series shapelets: a new primitive for data mining," Proceedings of the 15th ACM SIGKDD international conference on Knowledge discovery and data mining, pp. 947-956. 2009.

[153] M., Abdullah, E. Keogh, and N. Young. "Logical-shapelets: an expressive primitive for time series classification," Proceedings of the 17th ACM SIGKDD international conference on Knowledge discovery and data mining, pp. 1154-1162. 2011.

[154] J. Grabocka, N. Schilling, M. Wistuba, and L. Schmidt-Thieme, "Learning time-series shapelets," Proceedings of the 20th ACM SIGKDD international conference on Knowledge discovery and data mining, New York New York USA, pp. 392–401, Aug. 2014, doi: 10.1145/2623330.2623613.

[155] H., Lu, J. Kwok, and J. Zurada. "Efficient learning of timeseries shapelets," Proceedings of the AAAI Conference on Artificial Intelligence, vol. 30, no. 1, 2016.

[156] N. Karampatziakis, and P. Mineiro, "Discriminative features via generalized eigenvectors, "International Conference on Machine Learning, pp. 494-502, Jan. 2014.

[157] J. Lin, E. Keogh, S. Lonardi, and P. Patel, "Finding Motifs in Time Series," Proc. of the 2nd Workshop on Temporal Data Mining, pp.53-68, 2002.

[158] Y. Li, H. U. Leong, M. L. Yiu, and Z. Gong, "Quick-motif: An efficient and scalable framework for exact motif discovery," 2015 IEEE 31st International Conference on Data Engineering, Seoul, pp. 579–590, Apr. 2015, doi: 10.1109/ICDE.2015.7113316.

[159] Y. Zhu, C.-C. M. Yeh, Z. Zimmerman, K. Kamgar, and E. Keogh, "Matrix Profile XI: SCRIMP++: Time Series Motif Discovery at Interactive Speeds," 2018 IEEE International Conference on Data Mining (ICDM), Singapore, pp. 837–846, Nov. 2018, doi: 10.1109/ICDM.2018.00099.

[160] A. Tsitsipas, P. Schiessle, and L. Schubert, "Scotty: Fast a priori Structure-based Extraction from Time Series," 2021 IEEE International Conference on Big Data (Big Data), Orlando, FL, USA, Dec. 2021, pp. 2611–2620. doi: 10.1109/BigData52589.2021.9671513

[161] E. Keogh, J. Lin, and A. Fu, “HOT SAX: Efficiently Finding the Most Unusual Time Series Subsequence,” Fifth IEEE International Conference on Data Mining (ICDM’05), Houston, TX, USA, pp. 226–233,2005, doi: 10.1109/ICDM.2005.79.

[162] H. T. Q. Buu and D. T. Anh, “Time Series Discord Discovery Based on iSAX Symbolic Representation,” 2011 Third International Conference on Knowledge and Systems Engineering, Hanoi, Vietnam, pp. 11–18, Oct. 2011, doi: 10.1109/KSE.2011.11.

[163] L. Michele, Y. Zhu, T. Palpanas, and E. Keogh, "Matrix profile goes MAD: variable-length motif and discord discovery in data series," Data Mining and Knowledge Discovery, 34, no. 4, pp. 1022-1071, 2020.

[164] S. Lonardi, J. Lin, E. Keogh, and B. ‘Yuan-chi’ Chiu, “Efficient Discovery of Unusual Patterns in Time Series,” New Gener. Comput., vol. 25, no. 1, pp. 61–93, Nov. 2006, doi: 10.1007/s00354-006-0004-2.

[165] S. Theodoridis and K. Koutroumbas, Pattern Recognition, 4th ed., Burlington, MA: Elsevier, 2009.

[166] D. Berndt and J. Clifford, “Using Dynamic Time Warping to Find Patterns in Time Series,” AAAI-94 Workshop on Knowledge Discovery in Databases, pp. 359–370, 1994.

[167] E. Keogh and C. A. Ratanamahatana, “Exact indexing of dynamic time warping,” Knowl Inf. Sys., vol. 7, no. 3, pp. 358–386, Mar. 2005, doi: 10.1007/s10115-004-0154-9.

[168] X. Xi, E. Keogh, C. Shelton, L. Wei, and C. A. Ratanamahatana, “Fast time series classification using numerosity reduction,” Proceedings of the 23rd international conference on Machine learning - ICML ’06, Pittsburgh, Pennsylvania, pp. 1033–1040, 2006. doi: 10.1145/1143844.1143974.

[169] T. Rakthanmanon, B. Campana, A. Mueen, G. Batista, B. Westover, Q. Zhu, J. Zakaria, and E. Keogh, “Searching and mining trillions of time series subsequences under dynamic time warping,” Proceedings of the 18th ACM SIGKDD international conference on Knowledge discovery and data mining - KDD ’12, Beijing, China 2012 doi: 10.1145/2339530.2339576.

[170] R. Nick, S. Kelley, and F. Vincent. "Nearest neighbor queries," Proceedings of the 1995 ACM SIGMOD international conference on Management of data, pp. 71-79, 1995.

[171] D. A. White and R. Jain, “Similarity indexing with the SS-tree,” Proceedings of the Twelfth International Conference on Data Engineering, New Orleans, LA, USA, pp. 516–523, 1996 doi: 10.1109/ICDE.1996.492202.

[172] R. Davood and A. Mendelzon, "Similarity-based queries for time series data," Proceedings of the 1997 ACM SIGMOD international conference on Management of data, pp. 13-25, 1997.

[173] K. Chan and A. Fu, “Efficient time series matching by wavelets,” Proceedings 15th International Conference on Data Engineering (Cat. No.99CB36337), Sydney, NSW, Australia, pp. 126–133, 1999, doi: 10.1109/ICDE.1999.754915.

[174] A., Ira, R. Krieger, F. Afschari, and T. Seidl, "The TS-tree: efficient time series search and retrieval," Proceedings of the 11th international conference on Extending database technology: Advances in database technology, pp. 252-263, 2008.

[175] B. C. Giao and D. T. Anh, "Improving Sort-Tile-Recursive algorithm for R-tree packing in indexing time series," The 2015 IEEE RIVF International Conference on Computing & Communication Technologies - Research, Innovation, and Vision for Future (RIVF), pp. 117-122, 2015, doi: 10.1109/RIVF.2015.7049885.

[176] L. Zhang, N. Alghamdi, M. Y. Eltabakh, and E. A. Rundensteiner, “TARDIS: Distributed Indexing Framework for Big Time Series Data,” 2019 IEEE 35th International Conference on Data Engineering (ICDE), Macao, Macao, pp. 1202–1213, Apr. 2019, doi: 10.1109/ICDE.2019.00110.

[177] C. Faloutsos, M. Ranganathan, and Y. Manolopoulos, “Fast Subsequence Matching in Time-Series Databases,” ACM SIGMOD Record, vol. 23, issue. 2, pp.419-429, June 1994, https://doi.org/10.1145/191843.191925

[178] G. Das, D. Gunopulos, and H. Mannila, “Finding similar time series, “Principles of Data Mining and Knowledge Discovery, vol. 1263, J. Komorowski and J. Zytkow, Eds. Berlin, Heidelberg: Springer Berlin Heidelberg, 1997, pp. 88–100. doi: 10.1007/3-540-63223-9_109.

[179] M. Vlachos, G. Kollios, and D. Gunopulos, “Discovering similar multidimensional trajectories,” Proceedings 18th International Conference on Data Engineering, San Jose, CA, USA, pp. 673–684, 2002, doi: 10.1109/ICDE.2002.994784.

[180] V. Michail, M. Hadjieleftheriou, D. Gunopulos, and E. Keogh, "Indexing multi-dimensional time-series with support for multiple distance measures," Proceedings of the ninth ACM SIGKDD international conference on Knowledge discovery and data mining, pp. 216-225, 2003.

[181] A. Al-Maruf, H. H. Huang and K. Kawagoe, "Time Series Classification Method Based on Longest Common Subsequence and Textual Approximation," Seventh International Conference on Digital Information Management (ICDIM 2012), pp. 130-137, 2012, doi: 10.1109/ICDIM.2012.6360087.

[182] M. Taktak, S. Triki and A. Kamoun, "SAX-Based Representation with Longest Common Subsequence Dissimilarity Measure for Time Series Data Classification," 2017 IEEE/ACS 14th International Conference on Computer Systems and Applications (AICCSA), pp. 821-828, 2017, doi: 10.1109/AICCSA.2017.29.

[183] D. Nie, Y. Fu, J. Zhou, Y. Fang and H. Xia, "Time series analysis based on enhanced NLCS," 3rd International Conference on Information Sciences and Interaction Sciences, pp. 292-295, 2010, doi: 10.1109/ICICIS.2010.5534754

[184] C. Lei and R. Ng. "On the marriage of lp-norms and edit distance," Proceedings of the Thirtieth international conference on Very large data bases, vol. 30, pp. 792-803, 2004.

[185] L. Chen, M. T. Özsu, and V. Oria, “Robust and fast similarity search for moving object trajectories,” Proceedings of the 2005 ACM SIGMOD international conference on Management of data - SIGMOD ’05, Baltimore, Maryland, 2005. doi: 10.1145/1066157.1066213.

[186] M. D. Morse and J. M. Patel, “An efficient and accurate method for evaluating time series similarity,” Proceedings of the 2007 ACM SIGMOD international conference on Management of data - SIGMOD ’07, Beijing, China, 2007, doi: 10.1145/1247480.1247544.

[187] A. Stefan, V. Athitsos and G. Das, "The Move-Split-Merge Metric for Time Series," IEEE Transactions on Knowledge and Data Engineering, vol. 25, no. 6, pp. 1425-1438, June 2013, doi: 10.1109/TKDE.2012.88.

[188] D.Q. Goldin and P. C. Kanellakis. "On similarity queries for time-series data: constraint specification and implementation." International Conference on Principles and Practice of Constraint Programming, pp. 137-153. Springer, Berlin, Heidelberg, 1995.

[189] L., Xiang, L. Chen, J. X. Yu, G. Wang, and G. Yu. "Similarity match over high speed time-series streams," 2007 IEEE 23rd International Conference on Data Engineering, pp. 1086-1095, 2007.

[190] A. Bernieri, G. Betta, L. Ferrigno and M. Laracca, "Crack Depth Estimation by Using a Multi-Frequency ECT Method," IEEE Trans. on Instrumentation and Measurement, vol. 62, no. 3, pp. 544-552, March 2013, doi: 10.1109/TIM.2012.2232471

[191] H. Huang and T. Takagi, “Inverse analyses for natural and multicracks using signals from a differential transmit-receive ECT probe,” IEEE Trans. Magn., vol. 38, no. 2, pp. 1009–1012, Mar. 2002, doi: 10.1109/20.996259.

[192] J. C. Aldrin, E. B. Shell, E. K. Oneida, H. A. Sabbagh, E. Sabbagh, R. K. Murphy, S. Mazdiyasni, and E. A. Lindgren, "Model-based inverse methods for sizing surface-breaking discontinuities with eddy current probe variability." AIP Conference Proceedings. Vol. 1706. No. 1. AIP Publishing LLC, 2016.

[193] C. M. Bishop, Neural networks for pattern recognition, New York: Oxford university press, 1995

[194] R. E. Bellman, Dynamic programming, NJ: Princeton University Press,1957

[195] M. R. Cherry, A. Hutson, J. C. Aldrin, and J. Shank, “Eddy current analysis of cracks grown from surface defects and non-metallic particles,” AIP Conference Proceedings, 1949, 2018, doi: 10.1063/1.5031612.

[196] A. Papoulis, Probability, Random Variables and Stochastic Processes, 3rd ed., USA: McGraw Hill, 1994.

[197] N. E. Huang, Z. Shen, S. R. Long, M. C. Wu, H. H. Shih, Q. Zheng, N. C. Yen, C. C., Tung, and H. H. Liu, “The empirical mode decomposition and the Hilbert spectrum for nonlinear and non-stationary time series analysis,” Proc. R. Soc. Lond. A, vol. 454, no. 1971, pp. 903–995, Mar. 1998, doi: 10.1098/rspa.1998.0193.

[198] N. E. Huang, S. S. P. Shen Hilbert-Huang Transform and its Applications, New Jersey: World Scientific, 2014

[199] G. Yang, G. Dib, J. Kim, L. Zhang, J. Xin, and L. Udpa, “Nonlinear, non-stationary image processing technique for eddy current NDE,” AIP Conference Proceedings, 1430, 2012, pp. 689–696. doi: 10.1063/1.4716293.

[200] B. Liu, P. Huang, X. Zeng, and Z. Li, “Hidden defect recognition based on the improved ensemble empirical decomposition method and pulsed eddy current testing,” NDT & E International, vol. 86, pp. 175–185, Mar. 2017, doi: 10.1016/j.ndteint.2016.12.009.

[201] A. Stallone, A. Cicone, and M. Materassi, “New insights and best practices for the successful use of Empirical Mode Decomposition, Iterative Filtering and derived algorithms,” Sci. Rep., vol. 10, no. 1, p. 15161, Dec. 2020, doi: 10.1038/s41598-020-72193-2.

[202] T. Taniguchi, D. Kacprzak, S. Yamada, and M. Iwahara, "Wavelet-based processing of ECT images for inspection of printed circuit board," IEEE Transactions on Magnetics, vol. 37, no. 4, pp. 2790-2793, July 2001, doi: 10.1109/20.951308.

[203] R. Smid, A. Docekal, and M. Kreidl, “Automated classification of eddy current signatures during manual inspection,” NDT & E International, vol. 38, no. 6, pp. 462–470, Sep. 2005, doi: 10.1016/j.ndteint.2004.12.004.

[204] S. Safdarnejad, L. Udpa, S. S. Udpa, C. Buynak, G. Steffes, E. Lindgren, and J. Knopp, “Statistical algorithms for eddy current signal and noise analysis,” AIP Conference Proceedings, 1581, pp. 1328–1335, 2014, doi: 10.1063/1.4864975.

[205] Defense Advanced Research Projects Agency, DARPA-BAA-16-53: Broad Agency Announcement, Explainable Artificial Intelligence (XAI), 2016, [Online]. Available: https://www.darpa.mil/attachments/DARPA-BAA-16-53.pdf.

[206] R. Goebel, A. Chander, K. Holzinger, F. Lecue, Z. Akata, S. Stumpf, P. Kieseberg, and A. Holzinger, “Explainable AI: The New 42?” Machine Learning and Knowledge Extraction. CD-MAKE 2018. Lecture Notes in Computer Science A Holzinger, P. Kieseberg, A. Tjoa, E. Weippl (eds), vol 11015, Springer, Cham., 2018 https://doi.org/10.1007/978-3-319-99740-7_21

[207] W. Samek, G. Montavon, A. Vedaldi, L. K. Hansen, and K. R. Müller, Explainable AI: interpreting, explaining and visualizing deep learning, vol. 11700. Springer Nature, 2019.

[208] D. Doran, S. Schulz, and T. R. Besold, “What Does Explainable AI Really Mean? A New Conceptualization of Perspectives,” arXiv:1710.00794 [cs], Oct. 2017, Accessed: Oct. 14, 2021. [Online]. Available: http://arxiv.org/abs/1710.00794

[209] H. Hagras, "Toward Human-Understandable, Explainable AI," Computer, vol. 51, no. 9, pp. 28-36, September 2018, doi: 10.1109/MC.2018.3620965.

[210] R. R. Hoffman, G. Klein, and S. T. Mueller, “Explaining Explanation For ‘Explainable Ai,’” Proceedings of the Human Factors and Ergonomics Society Annual Meeting, vol. 62, no. 1, pp. 197–201, Sep. 2018, doi: 10.1177/1541931218621047.

[211] M. Bertovic, “Human factors in non-destructive testing (NDT): risks and challenges of mechanised NDT,” Ph. D. dissertation, Technische Universitaet. Berlin, Germany, 2015.

[212] C. Rudin, “Stop explaining black box machine learning models for high stakes decisions and use interpretable models instead”. Nat Mach Intell 1, 206–215 (2019). https://doi.org/10.1038/s42256-019-0048-x

[213] F. Poursabzi-Sangdeh, D. G. Goldstein, J. M. Hofman, J. W. Vaughan, and H. Wallach, "Manipulating and Measuring Model Interpretability," arXiv:1802.07810 [cs], Aug. 2021, Accessed: Oct. 14, 2021. [Online]. Available: http://arxiv.org/abs/1802.07810

[214] B. Ustun and C. Rudin, "Supersparse linear integer models for optimized medical scoring systems," Mach Learn, vol. 102, no. 3, pp. 349–391, Mar. 2016, doi: 10.1007/s10994-015-5528-6.

[215] J. C. Aldrin, E. A. Lindgren, and D. S. Forsyth, "Intelligence augmentation in nondestructive evaluation," AIP Conference Proceedings, 2102, 2019, doi: 10.1063/1.5099732.

[216] G. Guerrero, F. J. M. da Silva, A. Fernández-Caballero, and A. Pereira, "Augmented Humanity: A Systematic Mapping Review," Sensors, vol. 22, no. 2, p. 514, Jan. 2022, doi: 10.3390/s22020514.

[217] H. Hassani, E. S. Silva, S. Unger, M. TajMazinani, and S. Mac Feely, "Artificial Intelligence (AI) or Intelligence Augmentation (IA): What Is the Future?" AI, vol. 1, no. 2, pp. 143–155, Apr. 2020, doi: 10.3390/ai1020008.

[218] M. H. Jarrahi, "Artificial intelligence and the future of work: Human-AI symbiosis in organizational decision making," Business Horizons, vol. 61, no. 4, pp. 577–586 Jul. 2018, doi: 10.1016/j.bushor.2018.03.007.

[219] E. J. Griffen, A. G. Dossetter, A. G. Leach, and S. Montague, "Can we accelerate medicinal chemistry by augmenting the chemist with Big Data and artificial intelligence?" Drug Discovery Today, vol. 23, no. 7, pp. 1373–1384, Jul. 2018, doi: 10.1016/j.drudis.2018.03.011.

[220] E. Jussupow, K. Spohrer, A. Heinzl, and J. Gawlitza, "Augmenting Medical Diagnosis Decisions? An Investigation into Physicians' Decision-Making Process with Artificial Intelligence," Information Systems Research, vol. 32, no. 3, pp. 713–735, Sep. 2021, doi: 10.1287/isre.2020.0980.

[221] A. H. Kiran and P.-P. Verbeek, "Trusting Our Selves to Technology," Know. Techn. Pol., vol. 23, no. 3–4, pp. 409–427, Dec. 2010, doi: 10.1007/s12130-010-9123-7

[222] B. Maettig and H. Foot, "Approach to improving training of human workers in industrial applications through the use of Intelligence Augmentation and Human-in-the-Loop," 2020 15th International Conference on Computer Science & Education (ICCSE), Delft, Netherlands, Aug. 2020, pp. 283–288. doi: 10.1109/ICCSE49874.2020.9201867.

[223] A. Preece, D. Braines, F. Cerutti, and T. Pham, “Explainable AI for Intelligence Augmentation in Multi-Domain Operations,” arXiv:1910.07563 [cs], Oct. 2019, Accessed: Mar. 07, 2022. [Online]. Available: http://arxiv.org/abs/1910.07563

[224] P. Skagestad, “Thinking with machines: Intelligence augmentation, evolutionary epistemology, and semiotic,” Journal of Social and Evolutionary Systems, vol. 16, no. 2, pp. 157–180, Jan. 1993, doi: 10.1016/1061-7361(93)90026-N.

[225] K. L. A. Yau, H. J. Lee, Y. W. Chong, M. H. Ling, A. R. Syed, C. Wu, and H. G. Goh, “Augmented Intelligence: Surveys of Literature and Expert Opinion to Understand Relations Between Human Intelligence and Artificial Intelligence,” IEEE Access, vol. 9, pp. 136744–136761, 2021, doi: 10.1109/ACCESS.2021.3115494.

[226] A. Bernieri, G. Betta, L. Ferrigno and M. Laracca, "A biaxial probe for nondestructive testing on conductive materials," IEEE Trans. on Instrumentation and Measurement, vol. 53, no. 3, pp. 678-684, June 2004, doi: 10.1109/TIM.2004.827082

[227] A. Bernieri, L. Ferrigno, M. Laracca and M. Molinara, "Crack Shape Reconstruction in Eddy Current Testing Using Machine Learning Systems for Regression," IEEE Trans. on Instrumentation and Measurement, vol. 57, no. 9, pp. 1958-1968, Sept. 2008, doi: 10.1109/TIM.2008.919011

[228] T. Rocha, H. Ramos, A. L. Ribeiro and D. Pasadas, "Sub-surface defect detection with motion induced eddy currents in aluminum," 2015 IEEE International Instrumentation and Measurement Technology Conference (I2MTC) Proceedings, Pisa, 2015, pp. 930-934, doi: 10.1109/I2MTC.2015.7151394.

[229] A. Lopes Ribeiro, F. Alegria, O. Postolache and H. M. G. Ramos, "Eddy current inspection of a duralumin plate," 2009 IEEE Instrumentation and Measurement Technology Conference, Singapore, 2009, pp. 1367-1371, doi: 10.1109/IMTC.2009.5168669.

[230] D. E. Aguiam, L. S. Rosado, P. M. Ramos, and M. Piedade, “Heterodyning based portable instrument for eddy currents non-destructive testing,” Measurement, vol. 73, pp. 146–157, Sep. 2015, doi: 10.1016/j.measurement.2015.05.019.

[231] A. Aoukili and A. Khamlichi, “Modeling an Eddy-Current Probe for Damage Detection of Surface Cracks in Metallic Parts,” Procedia Technology, vol. 22, pp. 527–534 2016, doi: 10.1016/j.protcy.2016.01.112.

[232] J. R. S. Avila, Z. Chen, H. Xu, and W. Yin, “A multi-frequency NDT system for imaging and detection of cracks,” 2018 IEEE International Symposium on Circuits and Systems (ISCAS), Florence, 2018, pp. 1–4. doi: 10.1109/ISCAS.2018.8351849.

[233] L. Dai, H. Feng, T. Wang, W. Xuan, Z. Liang, X. Yang, “Pipe Crack Recognition Based on Eddy Current NDT and 2D Impedance Characteristics,” MDPI Appl. Sci., 9, 689, 2019.

[234] T. J. Rocha, A. L. Ribeiro, and H. M. G. Ramos, “Low-cost stand-alone system for eddy current testing of metallic non-ferromagnetic plates,” 2011 IEEE International Instrumentation and Measurement Technology Conference, Hangzhou, China, pp. 1–6, May 2011, doi: 10.1109/IMTC.2011.5944303.

[235] H. G. Ramos, T. Rocha, A. L. Ribeiro and D. Pasadas, "GMR versus differential coils in velocity induced eddy current testing," 2014 IEEE International Instrumentation and Measurement Technology Conference (I2MTC) Proceedings, pp. 915-918, 2014, doi: 10.1109/I2MTC.2014.6860875

[236] C. Ye, N. Zhang, L. Peng and Y. Tao, "Flexible Array Probe With In-Plane Differential Multichannels for Inspection of Microdefects on Curved Surface," IEEE Transactions on Industrial Electronics, vol. 69, no. 1, pp. 900-910, Jan. 2022, doi: 10.1109/TIE.2021.3050376.

[237] R. Caruana, R. Searle, T. Heller, and S. Shupack, "Fast algorithm for the resolution of spectra," Anal. Chem., vol. 58, no. 6, pp. 1162-1167, May 1986

[238] H. Guo, "A Simple Algorithm for Fitting a Gaussian Function [DSP Tips and Tricks]," IEEE Signal Processing Magazine, vol. 28, no. 5, pp. 134-137, Sept. 2011, doi: 10.1109/MSP.2011.941846.

[239] N. Hagen, M. Kupinski, and E. L. Dereniak, "Gaussian profile estimation in one dimension," Appl. Opt. 46, pp. 5374-5383, 2007

[240] S. M. Anthony and S. Granick, “Image Analysis with Rapid and Accurate Two-Dimensional Gaussian Fitting,” Langmuir, vol. 25, no. 14, pp. 8152–8160, Jul. 2009, doi: 10.1021/la900393v.

[241] A. Witkin, “Scale-Space Filtering A New Approach To Multi-Scale Description,” ICASSP’84, IEEE International Conf. on Acoustics, Speech, and Signal Processing, vol. 9, 1984

[242] A. Goshtasby, W.D. O’Neill, “Curve Fitting by a Sum of Gaussians,” CVGIP: Graphical Models and Image Processing, vol. 56, No. 4, pp. 281-288, July, 1994

[243] Z. Liu, G. Lu, X. Liu, X. Jiang, and G. Lodewijks, "Image processing algorithms for crack detection in welded structures via pulsed eddy current thermal imaging," IEEE Instrumentation & Measurement Magazine, vol. 20, no. 4, pp. 34-44, Aug. 2017, doi: 10.1109/MIM.2017.8006392.

[244] M. Rosenblatt, “Remarks on Some Nonparametric Estimates of a Density Function”, The Annals of Mathematical Statistics, 27,3, 1956, pp. 832-837, doi:10.1214/aoms/1177728190

[245] E. Parzen, “On Estimation of a Probability Density Function and Mode”, The Annals of Mathematical Statistics, 33,3, 1962, pp. 1065-1076, doi:10.1214/aoms/1177704472

[246] J. W. Earnest, "An Algorithm for Automated Feature Detection of Eddy Current Defects Using Sum of Gaussian Method," IEEE Trans. on Instrumentation and Measurement, vol. 70, pp. 1-8, 2021, Art no. 5005808, doi: 10.1109/TIM.2020.3047965.

[247] W. Quinn and S. Freed, "Signal Invariance to Probe Characteristics," 42nd AIAA/ASME/SAE/ASEE Joint Propulsion Conference & Exhibit, 2006

[248] R. H. Byrd, M. E. Hribar, and J. Nocedal, “An Interior Point Algorithm for Large-Scale Nonlinear Programming,” SIAM J. Optim., vol. 9, no. 4, pp. 877–900, Jan. 1999 doi: 10.1137/S1052623497325107.

[249] M. French, Fundamentals of Optimization. Switzerland: Springer International, 2018

[250] Iowa State University Center for Nondestructive Evaluation, “NDE-Ed.org: About NDT and NDE”, 2021, [Online]. Available: https://www.nde-ed.org/Physics/Waves/signaltonoise.xhtml

[251] Y. Wu, H. Wang, B. Zhang, and K-L. Du, "Using radial basis function networks for function approximation and classification.", International Scholarly Research Notices 2012, 2012

[252] J. Park and I. W. Sandberg, "Universal approximation using radial-basis-function networks." Neural Computation, vol. 3, no. 2, pp. 246-257, 1991.

[253] D. Tikk, L. T. Kóczy, and T. D. Gedeon. "A survey on universal approximation and its limits in soft computing techniques." International Journal of Approximate Reasoning, vol. 33, no. 2, pp. 185-202, 2003.

[254] S. Malinowski, T. Guyet, R. Quiniou, and R. Tavenard, October. “1d-sax: A novel symbolic representation for time series.” International Symposium on Intelligent Data Analysis, 2013, pp. 273-284.

[255] B. Bai, G. Li, S. Wang, Z. Wu, and W. Yan, “Time series classification based on multi-feature dictionary representation and ensemble learning,” Expert Systems with Applications, vol. 169, p. 114162, May 2021, doi: 10.1016/j.eswa.2020.114162

[256] K. Song, M. Ryu, and K. Lee, “Transitional sax representation for knowledge discovery for time series.”, Applied Sciences, vol. 10, no. 19, 2022.

[257] Y. Sun, J. Li, J. Liu, B. Sun, and C. Chow, “An improvement of symbolic aggregate approximation distance measure for time series.”, Neurocomputing, vol. 138, 2014, pp.189-198.

[258] R. C. McMaster, “The present and future of eddy current testing”, Materials evaluation, vol. 60, no.1, 2002.

[259] D. Jiles, Introduction to the principles of materials evaluation. CRC Press, 2007.

[260] T. Yu and D. Wilkinson, “A Fuzzy Symbolic Representation for Intelligent Reservoir Well Logs Interpretation,” Soft Computing for Hybrid Intelligent Systems, vol. 154, O. Castillo, P. Melin, J. Kacprzyk, and W. Pedrycz, Eds. Berlin, Heidelberg: Springer Berlin Heidelberg, 2008, pp. 417–426. doi: 10.1007/978-3-540-70812-4_25

[261] P. Senin and S. Malinchik, “SAX-VSM: Interpretable Time Series Classification Using SAX and Vector Space Model,” 2013 IEEE 13th International Conference on Data Mining, Dallas, TX, USA, Dec. 2013, pp. 1175–1180. doi: 10.1109/ICDM.2013.52

[262] K. Zhang, Y. Li, Y. Chai and L. Huang, "Trend-based symbolic aggregate approximation for time series representation," 2018 Chinese Control And Decision Conference (CCDC), 2018, pp. 2234-2240, doi: 10.1109/CCDC.2018.8407498.

[263] D. Zhao, S. Liu, Z. Miao, H. Zhang, Y. Wei and S. Xiao, "A Novel Feature Extraction Approach for Mechanical Fault Diagnosis Based on ESAX and BoW Model," IEEE Transactions on Instrumentation and Measurement, vol. 71, pp. 1-11, 2022, Art no. 3516011, doi: 10.1109/TIM.2022.3185658.

[264] P. M. Barnaghi, A. Abu Bakar and Z. A. Othman, "Enhanced symbolic aggregate approximation method for financial time series data representation," 2012 6th International Conference on New Trends in Information Science, Service Science and Data Mining (ISSDM2012), 2012, pp. 790-795.

[265] X. Bai, Y. Xiong, Y. Zhu, and H. Zhu, “Time series representation: a random shifting perspective,” Web-Age Information Management, Springer, 2013, pp. 37–50.

[266] N. D. Pham, Q. L. Le and T. K. Dang, "Two Novel Adaptive Symbolic Representations for Similarity Search in Time Series Databases," 2010 12th International Asia-Pacific Web Conference, 2010, pp. 181-187, doi: 10.1109/APWeb.2010.23.

[267] L.A.N.M. Lopez, D.K.S. Ting, and B.R. Upadhyaya, “Removing Eddy-Current probe wobble noise from steam generator tubes testing using Wavelet Transform.” Progress in Nuclear Energy, vol. 50, no. 7, 2008, pp. 828-835.

[268] J.C. Bezdek, R. Ehrlich, W. Full, “FCM: The fuzzy c-means clustering algorithm”, Computers & Geosciences, vol. 10. No. 2-3,1984, pp.191-203, https://doi.org/10.1016/0098-3004(84)90020-7

[269] S. Banerjee, A. Choudhary and S. Pal, "Empirical evaluation of K-Means, Bisecting K-Means, Fuzzy C-Means and Genetic K-Means clustering algorithms," 2015 IEEE International WIE Conference on Electrical and Computer Engineering (WIECON-ECE), 2015, pp. 168-172, doi: 10.1109/WIECON-ECE.2015.7443889.

[270] V. K. Dehariya, S. K. Shrivastava and R. C. Jain, "Clustering of Image Data Set Using K Means and Fuzzy K-Means Algorithms," 2010 International Conference on Computational Intelligence and Communication Networks, 2010, pp. 386-391, doi: 10.1109/CICN.2010.80.

[271] M. Ding, D. Chen, K. Xing and X. Cheng, "Localized fault-tolerant event boundary detection in sensor networks," Proceedings IEEE 24th Annual Joint Conference of the IEEE Computer and Communications Societies., vol. 2, 2005, pp. 902-913, doi: 10.1109/INFCOM.2005.1498320.

[273] I. Yesilyurt, “The application of the conditional moments analysis to gearbox fault detection—a comparative study using the spectrogram and scalogram”, NDT & E International, vol. 37, no. 4, 2004, pp.309-320, https://doi.org/10.1016/j.ndteint.2003.10.005

[273] H. -L. Dang, J. Kim, S. Kwak and S. Choi, "Series DC Arc Fault Detection Using Machine Learning Algorithms,” IEEE Access, vol. 9, pp. 133346-133364, 2021, doi: 10.1109/ACCESS.2021.3115512.

[274] A. Carlton, R. Morgan, W. Lohmeyer and K. Cahoy, “Telemetry Fault-Detection Algorithms: Applications for Spacecraft Monitoring and Space Environment Sensing”, Journal of Aerospace Information Systems, vol. 15, no. 5, 2018, pp. 239-252.

[275] Y. Sun, J. Li, J. Liu, B. Sun, and C. Chow. "An improvement of symbolic aggregate approximation distance measure for time series.", Neurocomputing, vol. 138, 2014, pp. 189-198.

[276] A. Bagnall, J. Lines, A. Bostrom, J. Large, and E. Keogh, “The great time series classification bake off: a review and experimental evaluation of recent algorithmic advances,” Data Min Knowl Disc, vol. 31, no. 3, pp. 606–660, May 2017, doi: 10.1007/s10618-016-0483-9.

[277] X. Wang, A. Mueen, H. Ding, G. Trajcevski, P. Scheuermann, and E. Keogh, “Experimental comparison of representation methods and distance measures for time series data,” Data Min Knowl Disc, vol. 26, no. 2, pp. 275–309, Mar. 2013, doi: 10.1007/s10618-012-0250-5.

[278] F. K. Došilović, M. Brčić and N. Hlupić, "Explainable artificial intelligence: A survey," 2018 41st International Convention on Information and Communication Technology, Electronics and Microelectronics (MIPRO), 2018, pp. 0210-0215, doi: 10.23919/MIPRO.2018.8400040.

[279] J. W. Earnest, “Sum of Gaussian Feature-Based Symbolic Representations of Eddy Current Defect Signatures" Research.in NDE, submission id:228740880.

[280] A. Skorupa, M. Skorupa, Riveted Lap Joins in Aircraft Fuselage: Design, Analysis, and Properties, Springer, 2012.

[281] U.S. Department of Defense, MIL-HDBK-1783B: Engine Structural Integrity Program, 2009

[282] D. R. Toui, A. Daas, B. Helifa, A. C. Lahrech, & L. I.Khaldoun, “Simple Giant Magnetoresistance Probe Based Eddy Current System of Defect Characterizatior for Non-Destructive Testing.”, Advanced Electromagnetics, vol. 11, no. 2, pp. 43-48, 2022.

[283] Digi-Key Electronics”, “Digi-Key Tech Forum”, 2018, [Online]. Available: https://forum.digikey.com/t/magnetoresistive-vs-hall-effect-in-sensor-applications/1185

[284] M. Anahid, M. K. Samal, & S. Ghosh, “Dwell fatigue crack nucleation model based on crystal plasticity finite element simulations of polycrystalline titanium alloys.”, Journal of the Mechanics and Physics of Solids, vol. 59, no. 10, pp. 2157-2176, 2011

[285] D.P. Shepherd & S. J. Williams, “New Lifing methodology for engine fracture critical parts”, QINETIQ LTD FARNBOROUGH UK, 2003.

[286] Iowa State University Center for Nondestructive Evaluation, “NDE-Ed.org: About NDT and NDE”, 2021, [Online]. Available: https://www.nde-ed.org/NDETechniques/EddyCurrent/ProbesCoilDesign/ProbesConfig.xhtml

[287] M. Cherry & C. Knott, “What Is Probability of Detection?”, Materials Evaluation, vol. 80, no. 12, 2022.

[288] Iowa State University Center for Nondestructive Evaluation, “NDE-Ed.org: About NDT and NDE”, 2021, [Online]. Available: https://www.nde-ed.org/NDETechniques/EddyCurrent/AdvancedTechniques/pulsedecinspection.x html

[289] The British Institute of Non-Destructive Testing, “www.bindt.org: What is NDT”, 2022, [Online]. Available: https://www.bindt.org/What-is-NDT/Index-of-acronyms/R/RFEC/#:~:text=RFEC%20%E2%80%93%20Remote%20Field%20Eddy%20Current,currents%20within%20the%20tube%20wall.

[290] United States Nuclear Regulatory Commission, “www.nrc.gov: Backgrounder on Steam Generator Tube Issues”, 2018, [Online]. Available: https://www.nrc.gov/reading-rm/doc-collections/fact-sheets/steam-gen.html

[291] NVE Corporation, “GMR Sensor Product Catalog”, 2022, [Online]. Available: https://www.nve.com/Downloads/catalog.pdf

APPENDIX A

GLOSSARY

Term	Definition
A/C	Aircraft
Aircraft Lap Joint	Aircraft skin material that is overlapped and typically bonded together via rivets or fasteners. The structures can be prone to corrosion and or cracking. [280]
A-Scan	Eddy current line scan. An eddy current probe is moved across the test material at a prescribed velocity and the probe voltage or impedance values are recorded at prespecified spatial/temporal instants.
Bobbin Coil	Probe coil design where the detection coil(s) is typically wound around a cylindrical form. One application of such a device is the inspection of interior cylindrical walls of metallic tubes by pulling the probe through the tube.
count	Analog-to-Digital conversion quantization level value.
C-Scan	Eddy current scan image. A collection of A-Scan eddy current signals arranged to form a spatial/temporal image of the test material probe voltage or impedance values.
D-coil	Differential coil used in an eddy current probe. Also known as Split-D due to geometry of the design. The design consists of two receive coils wound oppositely around matching half-cylindrical ferrite forms. The two receive coils are encircled by a drive/exciter coil.
EC Instrument	Instrument that connects to an eddy current probe and facilitates inspection of a test material. The device typically allows selection of inspection drive frequency and gain as well as filtering and signal processing manipulation functions (e.g., rotation) of received signals which aid in analysis. The user interface is usually provided as a 2D impedance plane representation of the received signals.
ECIS	Eddy Current Inspection System. Eddy current inspection system used for the depot inspection of USAF aircraft engine components.
EDM	Electrical/Electro discharge machining. A process that uses controlled electrical discharges to create voids in a test material. The systems that perform the process typically utilize Computerized Numerical Control (CNC) robotics to allow precise location of the voids.
ENSIP	Engine Structural Integrity Program. Framework that describes considerations and guidance for gas turbine engines design and sustainment throughout the component lifecycle [281].
Flight Cycle	A start, flight, landing, and shutdown sequence in aircraft operation. The number of cycles is a measure used to determine maintenance actions on the engine.

Term	Definition
FOV	Field of View. As regards time series, the time interval under analysis for a specified processing technique.
Fracture Critical Component	Aircraft components which if failed would hazard the entire aircraft
Fracture Mechanics	The study of the propagation dynamics of defects in materials.
Gantry Robot	Robotic system that permits primarily linear movement typically in a 2D or 3D environment. The ECIS system utilizes a cantilevered Gantry design that permits Cartesian movement of an eddy current probe in a XYZ (3D) environment.
GMR	Giant Magnetoresistance. GMR devices change resistance when in the presence of an external magnetic field. The GMR devices respond to magnetic fields that are parallel to the sensor compared to Hall effect sensors which respond to fields perpendicular to the sensor. In addition, the GMR is typically more sensitive than Hall effect sensors [282],[283].
Grain Noise	Crystallites or “grains” form polycrystalline structures in some metallic materials with Titanium alloys as one notable example. In relation to eddy current analysis, the grains and their associated boundaries disturb the formation of eddy currents in the material which in term give rise to noise in the return signal. The resulting phenomenon is termed "grain noise" to identify it with the responsible mechanism [284].
Horizontal data	Horizontal (as referenced to the Impedance Plane) “resistive” data component from the received eddy current response.
HPT Disk	High Pressure Turbine Disk. Engine component of a gas turbine engine
Impedance Plane	Resistive versus Reactive plot of probe impedance components over a region of interest. Also known as an Argand diagram.
Inspection Frequency	Eddy current inspections typically utilize sinusoidal signals for material state analysis. In these cases, the inspection frequency is the frequency of the drive signal applied to the eddy current probe.
Lifing Model	Model used to statistically calculate the component life expectancy. The model provides sustainment information used to ensure that fracture critical components are only in service for the acceptable number of operational cycles as not to induce component failure [285].

Term	Definition
lift-off	Distance between the coil of an eddy current probe and the test material. The probe drive signal attenuates with the distance from the probe coil. This has the net effect of also reducing the eddy current field strength which in turn results in lower amplitude return signals.
Lift-Off Phase	Two primary phenomena encountered in an eddy current inspection are conductivity change in the test material possibly due to a crack, void, or embedded dissimilar material and physical separation of the probe from the test material (i.e., lift-off). To minimize the effects of lift-off from analysis, the lift-off component is rotated into the resistive axis of the Impedance plane. To determine the rotation angle, a least squares regression approximation of probe lift-off signal (obtained by controlled removal of the probe from the test material) referencing the horizontal axis of the Impedance plane is obtained. Also termed as "phase" depending on the context.
Line Scan	Single scan of an eddy current probe over the region of interest. Also known as an A-Scan.
Longitudinal Orientation	Orientation wherein the split line of the differential coil probe is parallel to the defect length. This orientation typically results in smaller system response extrema in the line scan (referenced to transverse orientation) due to the orientation of the probe response field to the defect. In this orientation, line scans typically place the defect under the influence of only one coil in the response field.
mil	Unit of measure. 1/1000 of an inch.
NDE	Nondestructive Evaluation. Method used to analyze the state of the UUT without irreversibly disturbing the properties of material.
Over-inspection	Situation wherein any of the parameters of the inspection negatively affect (i.e., increase) the peaks amplitudes in the defect response resulting in a possibly smaller defect being incorrectly sized as a larger defect.
Pancake Coil	EC coil wound such that the axis of the coil is perpendicular to the surface of the UUT. The resulting inspection coil is typically only a few coil diameters in height [286].
Penetration Depth	Depth that the incident electromagnetic waves penetrate into the test material. Penetration depth is related to skin depth and as such is inversely related to the inspection frequency.

Term	Definition
PoD	Probability of Detection. Statistical analysis framework used to quantify uncertainty in eddy current inspections typically in terms of binary decisions (e.g., hit/miss) or for continuous quantities like defect size (e.g., depth, length) the probability of detection for a specified defect size. The data for a PoD analysis is usually gathered using known sized crack specimens from which the system response value (e.g., maximum peak amplitude) is obtained and analyzed using statistical regression methods [287].
Probe Response	Received horizontal (resistive) and vertical (reactive) channel signals from eddy current line scan.
Pulsed Eddy Current	Eddy current inspection technique wherein the probe drive signal is a transient pulse. Transient pulses constitute numerous frequencies ranging from low to high as indicated by Fourier analysis. Due to the penetration depth inverse relationship to inspection frequency, the resulting inspection method is able to obtain greater information regarding the depth of a material defect [288].
Reference Standard	Material that typically contains defects of known size and material that is used to calibrate the eddy current probe prior to and post inspection.
RFC	Retirement For Cause. Engine component replacement program wherein components are replaced based upon material state and not primarily on time of use.
RFEC	Remote Field Eddy Current. Eddy current inspection technique wherein the driver/exciter coil and receive coils are separated a prescribed distance. The technique is particularly useful in the scenario regarding the need to determine material status of buried pipes where access to the external surface is problematic [289].
ROI	Region of Interest. Line scan or scan image area inspected by an eddy current probe.
Scan Image	Collection of adjacent eddy current line scans arranged as a 2D image. Also known as C-Scan images.
SG Tube	Steam generator tube. Utilized in pressurized water based nuclear reactors. Transfers heat from radioactively heated water to create steam in water external to the tube which is then used to drive an electrical power turbine [290].

Term	Definition
Skin Depth	Phenomenon wherein the depth of the electric current relative to the external surface of a conductor is inversely related to the current frequency. Thus, for higher frequencies the current is constrained to outer surface of a conductor. Skin depth is utilized to provide guidelines regarding the penetration depth of the drive signal for eddy current inspections. The skin depth (in meters) [13] for a material of electrical conductivity σ and magnetic permeability μ is related to the drive frequency as: $$\delta = \frac{1}{\sqrt{\pi f \sigma \mu}}$$
System Response	Value obtained from an eddy current line scan that is typically used as the dependent variable to develop a mathematical relationship between the value and the defect size. In many instances the value used is based on the extrema features in the probe response to the defect.
Transverse Orientation	Orientation wherein the split line of the differential coil probe is perpendicular to the defect length. This orientation typically results in larger system response extrema in the line scan (referenced to longitudinal orientation) due to the orientation of the probe response field to the defect. In this orientation, line scans typically place the defect under the influence of both coils in the response field.
Under-inspection	Situation wherein any of the parameters of the inspection negatively affect (i.e., decrease) the peak amplitudes in the defect response resulting in a possibly larger defect being incorrectly sized as a smaller defect.
USAF	United States Air Force
UUT	Unit Under Test. Referencing the Retirement For Cause program, the UUT is often the component of an aircraft engine
Vertical data	Vertical (as referenced to the Impedance plane) “reactive” data component from the received eddy current response.

Term	Definition
Wheatstone Bridge	Two voltage dividers connected in parallel with some of the impedance elements providing biasing while the others are sensors which change impedance in response to external phenomena. As relates to eddy current analysis, the bridge sensor elements change impedance in the presence of a change in the magnetic field as the bridge passes over a defect in the test material. One example of the use of the Wheatstone bridge is in the GMR based eddy current probe mentioned in [1]. Figure 1, provides a functional diagram of the arrangement, wherein two of the impedance elements are magnetically shielded. [282]. 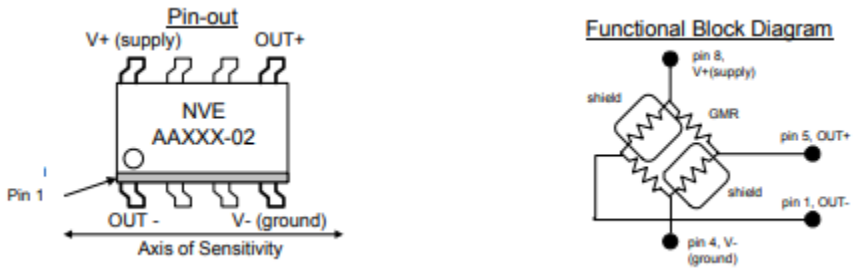 Figure A.1 GMR Wheatstone Bridge Example [291]